Synthesis, Structure and Properties of TiCoSb-Based Half-Heusler Thermoelectrics

Maryana Asaad

Submitted for the degree of Doctor of Philosophy

Heriot-Watt University

Institute of Chemical Sciences

February 2017

Abstract

Half-Heusler compounds have gained significant attention due to their potential as thermoelectric materials for high temperature waste heat recovery. They are characterised by a favourable combination of large Seebeck coefficients and low electrical resistivities, leading to large power factors but also have relatively large thermal conductivities, which limit the thermoelectric figure of merit ZT to values near one. TiCoSb-based half Heusler compounds are considered as promising p-type thermoelectric materials, however, studies on these compounds are fewer in number as compared to other half Heusler systems. For this reason, three novel series of TiCoSb-based half Heuslers were prepared and studied in this thesis.

A detailed investigation of the $Ti_{1-x}V_xCoSb_{1-x}Sn_x$ half Heusler alloys is provided in Chapter 3. This study revealed that V and Sn co-substitution improves the high-temperature thermal stability of these materials. Thereafter, in Chapter 4, attempts were made to p-type dope these materials by substitution of Fe on the Co site. Surprisingly, electrical property measurements revealed n-type conduction for a number of the investigated samples. Thus, this study provides the first experimental observation of an unexpected change in carrier type in half Heusler compounds. The last results chapter of this thesis explores TiCoSb-based nanocomposites. Five series of compositions $(TiCoSb)_{1-x}(TiM_2Sn)_x$ (M_2 = Fe_2, FeCo, Co_2, CoNi, Ni_2) were prepared. In which, these compounds are expected to segregate into half Heusler and full Heusler phases.

All samples were prepared using solid-state reactions. The synthesised materials were structurally characterised using X-ray and neutron powder diffraction. Complementary scanning and transmission electron microscopy was performed to probe the microstructure and compositional homogeneity of the investigated samples. This has allowed, coupled with measuring the thermoelectric properties, the structure-property relations to be established.

Acknowledgments

First, I would like to thank my supervisor Dr. Jan-Willem Bos for his guidance, support, motivation and immense knowledge throughout my studies at Heriot-Watt University. I have been really fortunate to have a supervisor who cared so much about my work and taught me how to be a good researcher. Without his help and encouragement, the completion of this PhD could not have been possible.

I would also like to acknowledge the technical and support staff at Heriot-Watt University. I am particularly grateful to Alan Barton and Paul Allen, who were always ready to help. A special thanks is also extended to Peter Reinbold for his endless support. My thanks and appreciation go to Ron Smith at ISIS and Jim Buckman in the Institute of Petroleum Engineering-Heriot-watt University, who carried out the electron microscopy experiments.

I would like to express my special thanks to all members of the Materials Chemistry group at Heriot-Watt University, which has been a source of friendship and great support, especially Sonia Barczak, Daniella Ferluccio, Jean-Marie Cols and Paul Murphy. My sincere thanks are due to Dr. Srinivas Popuri for his constant help and encouragement.

My special words of thanks go to Mrs Connie Smeaton for her parent-like care, support and advice. She has always been there for me through not only the good times but also the tough times. My stay at her house made me feel just like home!

Finally, I would like to thank my family for their support, encouragement and endless love during my PhD studies and throughout my life.

DECLARATION STATEMENT

TABLE OF CONTENTS

LIST OF PUBLICATIONS BY THE CANDIDATE

1. “Thermoelectric properties and high-temperature stability of the $Ti_{1-x}V_xCoSb_{1-x}Sn_x$ half-Heusler alloys”: M. Asaad, J. Buckman, R. I. Smith and J. W. G. Bos, *RSC Adv*., 2016, 6, 56511.

LIST OF ABBREVIATIONS

ZT	Thermoelectric figure-of-merit
VB	Valence band
CB	Conduction band
DOS	Density of states
PGEC	Phonon-glass-electron-crystal
VEC	Valence electron count
HH	Half Heusler
FH	Full Heusler
XRD	X-ray diffraction
NPD	Neutron powder diffraction
SEM	Scanning electron microscopy
TEM	Transmission electron microscopy
STEM	Scanning transmission electron microscopy
EDX	Energy dispersive X-ray analysis

Chapter 1–Introduction

The world is facing a huge challenge concerning the immense demand for energy, with the rapid decline of fossil fuel resources and the increasing greenhouse effects. [1] Renewable energy technologies are considered as the main solutions to address these problems. These include solar, wind, biomass and geothermal energy conversion technologies, amongst others. In 2008, renewable energies contributed to about 12.9% of the total primary energy supply. [2] This percentage has been increasing rapidly due to different factors such as the increase in the price of fossil fuels and government policies on limiting CO_2 emissions. The key challenge associated with renewable energies lies in capturing and storing their energy. Among the different types of renewable energy technologies, thermoelectric energy conversion has been receiving huge interest and is expected to play an important role in meeting the world's future energy demand. [3]

Thermoelectricity involves the direct conversion of thermal energy to electrical power and vice versa, via the Seebeck or Peltier effect. A vast amount of energy produced in everyday life is lost as heat. For instance, during electrical power generation, about 65 % of the energy produced in a power plant is lost as waste heat and therefore only 35 % reaches our houses as electrical energy. [4] Another example is the heat wasted during combustion process in a car, in which about 40% of energy generated is wasted in the form of heat. [5] In this case, thermoelectric devices can act as power generators and offer a promising approach to recover this low grade waste thermal energy, which cannot be done by conventional power generators. [6] Furthermore, thermoelectric devices can be used as primary energy sources, where they can directly harness the solar thermal energy, using energy in the infrared part of spectrum. [7] In addition to power generation, thermoelectric devices are capable to convert a voltage gradient into a temperature difference using the Peltier effect; as a result, they can be used for different heating and cooling applications. [8]

Thermoelectric devices have many features and characteristics that attract a significant interest in using this technology for a wide range of applications. They are solid state devices, no vibration, no mechanical moving parts, no environmentally harmful gases or fluids. They have high reliability, are small in size, and are simple and safe. [3] Some are able to tolerate extreme conditions, including pressure, temperature, radiation and shock. [9]

Although thermoelectric technology has impressive environmental advantages and could play a more significant role in meeting the energy challenge of the future, the low efficiency of these devices has restricted their use to niche applications, where reliability, simplicity, long life and size are much more important than efficiency and cost. For instance, thermoelectric power generators have been used widely by NASA to produce power in their space exploration such as the Apollo to the moon and the Viking to Mars missions. [10] Also, small-scale thermoelectric coolers have been extensively used for the cooling of components in computers, infrared detectors, laser diodes, amongst others. [11] Currently, many research groups around the world are focussing on improving the efficiency of thermoelectric materials, driven by the advent of more applications, especially for waste heat recovery in automobiles. The work presented in this thesis forms a part of the ongoing search for thermoelectric materials with better performance. TiCoSb is considered as promising candidate for high temperature thermoelectric applications, however, it is less well studied in the literature as compared to other half Heusler systems such as TiNiSn. Here, the structure and properties of various TiCoSb based half Heuslers are investigated and the obtained results provide novel and important scientific contribution to the literature.

1.1. Thermoelectric Effects

1.1.1. Seebeck Effect

The Seebeck effect was discovered by the German physicist Thomas Johann Seebeck in 1821. [12] Seebeck noticed that a compass needle is deflected when a temperature difference is applied across two different conductors connected in a closed loop, as illustrated in Figure 1.1.

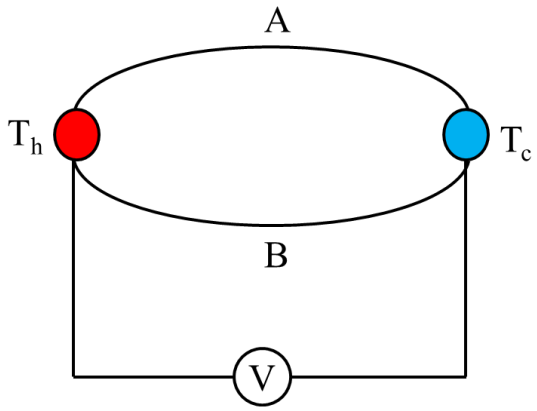

Figure 1.1. Schematic experimental set up for the Seebeck effect. T_c and T_h are the cold and hot junctions between two metals A and B.

Seebeck related this behaviour to magnetic effects. However, this phenomenon was later recognised to be caused by generating a magnetic field due to an electrical current flowing in the loop. Here, the temperature gradient leads to differing chemical potential for electrons at both ends, and electrons will then flow through the metals until an electric field builds up to compensate this difference. An electric field means that a voltage is generated between the junctions. This voltage is called the Seebeck voltage and it is found to be proportional to the temperature difference. The ratio of the voltage generated (ΔV) and the applied temperature difference defines the Seebeck coefficient (S), which is usually expressed in units of μV/K. This is given in Equation (1.1). [13]

$$S = \frac{\Delta V}{\Delta T} \qquad \text{Equation (1.1)}$$

1.1.2. The Peltier effect

A short time later, another effect was discovered by the French physicist Jean Peltier, who noticed temperature changes at the junctions of two different conductors when an electrical current passes through these junctions. The heat is found to be absorbed at one junction and rejected at the other, depending on the direction of the current [14] A schematic of the Peltier effect is shown in Figure 1.2.

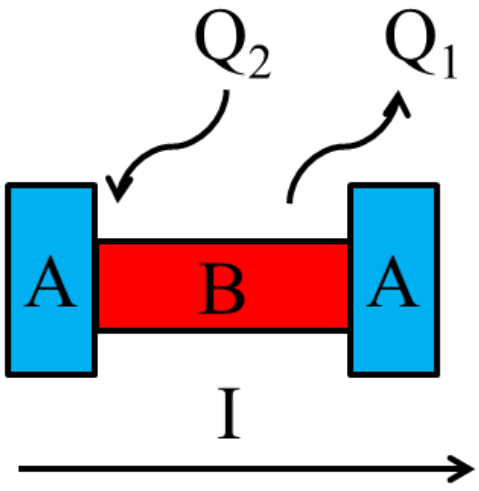

Figure 1.2. Schematic of the Peltier effect. Where an electrical current (I) passes through two different metals A and B, the heat is dissipated at one junction (Q_1) and absorbed at the other (Q_2). Reversing the direction of the current leads to reverse the temperature of the hot and cold junctions.

The physical explanation for the Peltier effect involves moving electrons from a low energy level in material (A) through one junction to a higher energy level in material (B) leading to cooling effect, as this transport requires heat absorption from the environment. Meanwhile, at the other junction heat is ejected, as electrons return to a lower energy level. Typically, the rate of heat exchange (Q) at the junctions is related to the Peltier coefficients of both materials Π_A and Π_B, and the current flowing through the materials (I), as described in Equation (1.2).

$$Q = (\Pi_A - \Pi_B)I \qquad \text{Equation (1.2)}$$

The cooling effect is usually reduced due to two factors; the first one is Joule heating and the second is the conducted heat. Joule heating occurs in most materials and can be defined as the heat produced when an electrical current flows through a material. It is proportional to the square of the current and the resistance, R, as given in Equation (1.3).

$$Q = R\,I^2 \qquad \text{Equation (1.3)}$$

Conducted heat arises from the temperature difference between the hot and cold junctions, where heat will be conducted through charge carriers from the hot to the cold end. Clearly, both conducted and Joule heat increase with increasing the current. However, at a certain value of the applied current, the Joule heating becomes dominant, as it is proportional to I^2, and any further increase in the current will lead to less cooling power. Consequently, there is a maximum current at which a maximum cooling can be obtained.

The established relationship that expresses the Peltier effect in terms of the Seebeck effect is given by Equation (1.4). [12]

$$\Pi = ST \qquad \text{Equation (1.4)}$$

Where Π is the Peltier effect, S is the Seebeck effect and T is the absolute temperature.

1.1.3. The Thomson Effect

A third thermoelectric effect was discovered by W. Thomson, who realised that there must be a relation between the Seebeck and Peltier effects. This effect describes the cooling or heating in a single homogenous conducting material, when subjected to both an electrical current and a temperature gradient. This effect can be expressed by Equation (1.5). [15]

$$Q = \beta / \Delta T \qquad \text{Equation (1.5)}$$

Where Q represents the rate of generation of heat and β is the Thomson coefficient.

1.2. Thermoelectric Devices

A thermoelectric module consists of several alternating n-type and p-type semiconductor materials (thermoelectric couples) which are connected electrically in series and thermally in parallel, by backing them between two electrically insulating but thermally conducting substrates. A schematic of thermoelectric couples used for power generation (a) and cooling (b) is depicted Figure 1.3.

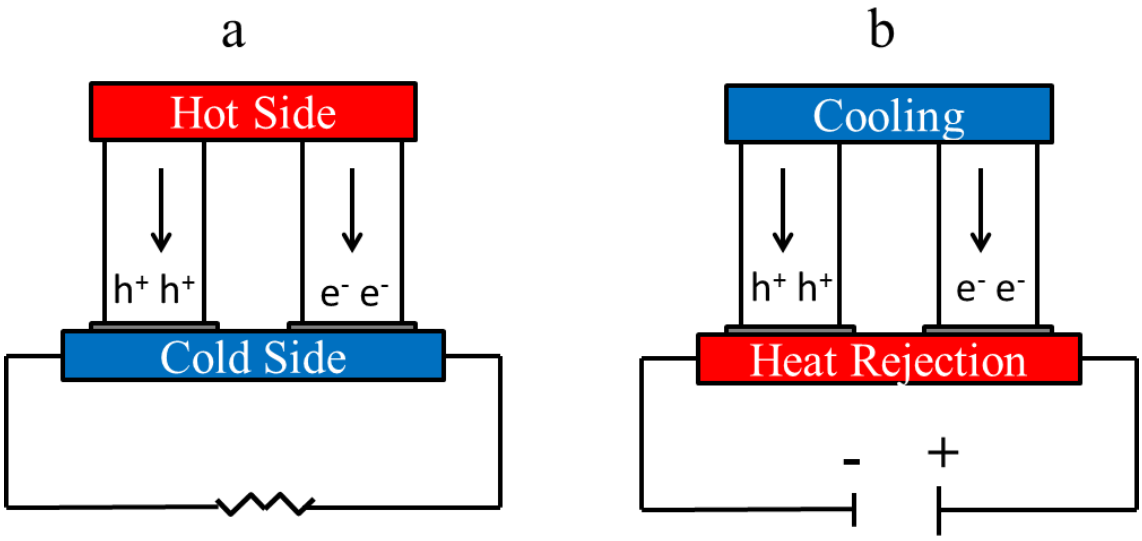

Figure 1.3. A schematic of thermoelectric couples used for power generation (a), using the Seebeck effect and cooling (b), using the Peltier effect.

It is clear from Figure 1.3 that the geometry for power generation and cooling is conceptually the same. Thermoelectric power generation (TEG) (Figure 1.3a) occurs when a temperature difference is applied across a thermoelectric device, in which the free charge carrier, either electrons for an n-type material or holes for a p-type material, diffuse from the hot side to the cold side producing a voltage difference (Seebeck voltage), which drives an electrical current when the circuit is completed. Conversely, in cooling mode (Figure 1.3b), a temperature difference can be generated at the interface by applying an electrical current through the thermoelectric couple. In this case, which exploits the Peltier effect, the temperature of one end of the thermoelectric material increases and the other decreases. Heat absorption or rejection, as previously described, depends on the direction of the current.

For both power generation and cooling to be efficient, it is essential to maintain a maximum temperature between the hot and cold sides and this requires the materials to have low thermal conductivity. On the other hand, the materials should be also good electric conductors so that the heat produced due to Joule heating is minimised in cooling mode and the power produced in power generation mode is maximised. [16] This will be discussed in more detail in the section below.

1.3. Thermoelectric efficiency

The performance of a thermoelectric device is determined by the applied temperature gradient and an intrinsic material parameter, the thermoelectric figure of merit (*ZT*), which was first introduced by Altenkirch in 1911. [17] For power generation, the thermoelectric efficiency can be defined as shown in Equation (1.6).

$$\eta = \frac{\Delta T}{T_{hot}} \frac{\sqrt{1 + (ZT)_{avg}} - 1}{\sqrt{1 + (ZT)_{avg}} + \frac{T_{cold}}{T_{hot}}} \qquad \text{Equation (1.6)}$$

Where η is the efficiency of the thermoelectric device, T_{hot} and T_{cold} are the temperature of the hot and cold end, respectively, $\Delta T = T_{hot} - T_{cold}$, $(ZT)_{avg}$ is the average of *ZT* and the term ($\Delta T/T_{hot}$) represents the Carnot efficiency. It is clear from Equation (1.6) that increasing the thermoelectric efficiency requires both large temperature gradients and high *ZT* values. The efficiency of the current thermoelectric devices is about 5-6 %, limited by *ZT* values around 1. It is expected that increasing *ZT* by a factor of 4, will lead to an efficiency of ~ 30%. [18] Consequently, achieving high *ZT* values will enable a wider use of thermoelectric devices and make them one of the several technologies working together to meet the global energy challenges.

The figure of merit for a thermoelectric material is defined by Equation (1.7).

$$ZT = \frac{S^2 \sigma}{\kappa} T \qquad \text{Equation (1.7)}$$

$$\kappa = \kappa_e + \kappa_{lat} \qquad \text{Equation (1.8)}$$

Where *S* is the Seebeck coefficient, σ is the electrical conductivity, κ is the thermal conductivity, which is the sum of two contributions; the electronic part (κ_e), which represents the heat carried by charge carriers (either electrons or holes) and the lattice contribution, κ_{lat}, which is the heat carried by phonons (lattice vibrations), as illustrated

in Equation (1.8) and T is the absolute temperature. The product $S^2\sigma$ is known as the power factor, which is a direct measure of the electrical power that can be generated.

It is obvious from Equation (1.7) that achieving high ZT in a material requires high S, high σ and low κ. Unfortunately, materials with this unique combination are not naturally available. As illustrated in Figure 1.4, metals have high σ, low S and high κ at the same time, while insulators are the reverse; they possess low κ and high S but also low σ. Optimising these properties for a given material is not straightforward, as these three thermal-electrical properties are linked to each other through the electronic structure of the material, and cannot be optimised independently. For example, increasing σ by increasing charge carrier concentration leads to an increase in κ through increasing the electronic contribution, κ_e. As shown in Figure 1.4, the best thermoelectric materials are typically heavily-doped semiconductors with charge carrier concentration of 10^{19}-10^{21} carriers cm^{-3}. [19]

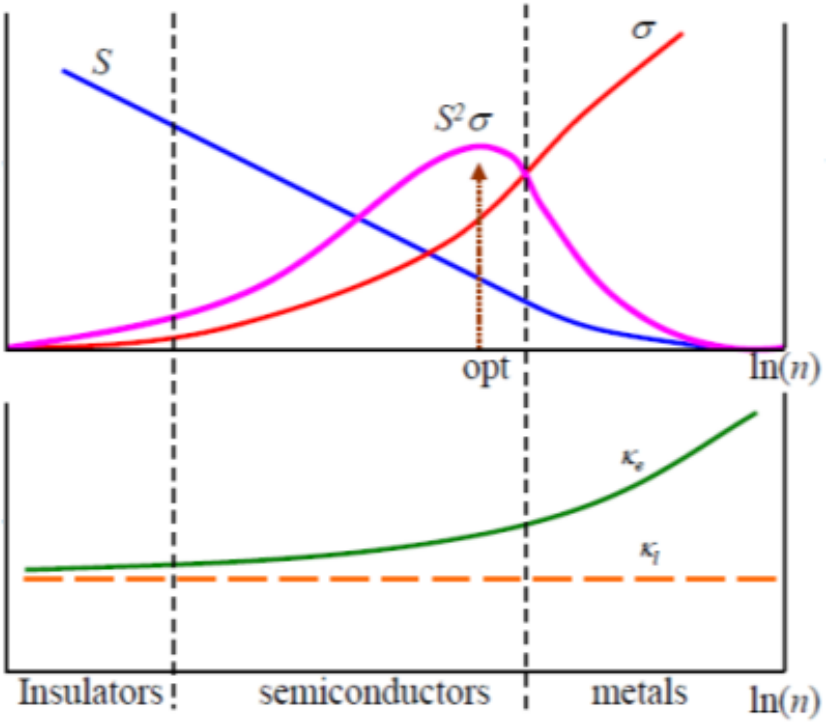

Figure 1.4. The dependency of S, σ and κ on charge carrier concentration for metals, insulators and semiconductors. [20]

1.4. Thermoelectric Properties

1.4.1. Seebeck Coefficient, *S*

As discussed above, maximising *ZT* requires a large *S*, large σ and low κ. Typically, to obtain a large *S*, a single type of charge carrier should be maintained, as the presence of both electrons and holes means that both of them will move to the cold side and thus minimizing the produced Seebeck voltage. This can be deduced from *S* formula for semiconductors containing both electrons and holes, which is described by Equation (1.9). [21]

$$S = \frac{S_n\sigma_n + S_p\sigma_p}{\sigma_n + \sigma_p} \qquad \text{Equation (1.9)}$$

Where *S* is the effective Seebeck coefficient, S_n and S_p the partial Seebeck coefficients for electrons and holes, respectively, and σ_n and σ_p are their electrical conductivities. S_n is a consequence of n-type conduction (where electrons are the majority charge carriers) and thus has a negative value, while S_p has a positive value, resulting from p-type conduction (where holes are the majority charge carriers). If both S_n and S_p are large, they will cancel each other out and the resulting *S* will be lower as compared to a material with a single charge carrier. This also explains the drop in S observed for most extrinsically doped semiconductors at high temperatures, where minority charge carriers are excited across the band gap, leading to lower *S* values.

The *S* of a material can be also expressed in term of its electronic structure, using the Mott equation, as defined in Equation (1.10). [22]

$$S = \frac{\pi^2}{3}\frac{{k_B}^2 T}{e}\left\{\frac{d\ln\sigma(E)}{dE}\right\}_{E=E_F} \qquad \text{Equation(1.10)}$$

Where k_B is the Boltzmann constant, *e* is the electron charge, $\sigma(E)$ is the energy dependent electrical conductivity and E_F is the Fermi energy.

If the electronic scattering is independent of energy, $\sigma(E)$ will be related only to the electronic density of states (DOS) at energy, E. This implies that a rapid change in the density of states near E_F (large slope) will produce high *S* values. It is expected that materials with complexity in their structure and composition tend to have complex electronic structure, which in turn may lead to a sharp peak in the DOS near E_F and thus producing large *S* values. In addition, a complex electronic structure with multiple

maxima (degeneracy) in the valence and conduction bands near E_F is expected to produce large *S* values. In this case, each maximum will contribute to a certain *S* value and the total *S* for the material will be the summation of all contributions. This property, however, requires high crystal symmetry, which can be realised in cubic, hexagonal and tetragonal crystal systems, making them the main focus of thermoelectric research. [18,23] For semiconductors with high doping level (degenerate semiconductors), *S* can be described by Equation (1.11)

$$S = \frac{8\pi^2 {k_B}^2}{3eh^2} m^* T \left(\frac{\pi}{3n}\right)^{2/3} \qquad \text{Equation (1.11)}$$

Where *n* is the charge carrier concentration, *h* is Planck's constant and m^* is the effective mass of the charge carrier and is related to the band effective mass, m^*_b, as described in Equation (1.12). [24]

$$m^* = (N_V)^{2/3} m_b^* \qquad \text{Equation (1.12)}$$

Where N_v is the number of degenerated valleys (maxima) of the band structure.

It is clear from this Equation (1.11) that charge carrier concentration as well as the effective mass, m^*, provide a conflict regarding the optimisation of *ZT*, since σ and *S* will vary in opposite way upon the increasing of carrier concentration or the effective mass.

1.4.2. Electrical Conductivity, σ

σ is directly related to carrier concentration, *n*, and the mobility of charge carrier, μ, as described in Equation (1.13).

$$\sigma = \frac{1}{\rho} = ne\mu \qquad \text{Equation (1.13)}$$

Where ρ is the electrical resistivity, *e* is the charge of the carrier.

It is obvious from Equation (1.13) that achieving high σ requires high charge carrier concentration, which has an opposite effect on *S*. The mobility of charge carriers can be described as a function of the effective mass, *m**, as stated in Equation (1.14).

$$\mu = e\tau / m^* \qquad \text{Equation (1.14)}$$

Where *e* the charge of the carrier, *m** is the effective mass and τ is the relaxation time, which can be defined as the mean time between collisions for charge carriers. This

implies that heavy charge carriers will move slowly, resulting in lower mobilities and thus lower σ. This is again, as mentioned in Section 1.4.1, a conflicting situation with S.

In semiconductors, for conduction to take place, charge carriers should be excited through the band gap, E_g, as illustrated in Equation (1.15). [11]

$$\sigma = \sigma_0 exp\left(-\frac{E_g}{2k_B T}\right) \qquad \text{Equation (1.15)}$$

Where k_B is the Boltzmann constant and T is the absolute temperature. Clearly, materials with small band gaps are expected to have higher σ. This equation can be also used to estimate the band gap of a semiconducting material if the temperature dependence of σ (or resistivity) is available.

1.4.3. Thermal Conductivity, κ

The thermal conductivity, κ, of a material is the sum of two contributions, the electronic component, κ_e, which is the heat carried by charge carriers, and the lattice part, κ_{lat}, which is the heat conducted by phonons (Equation (1.8)). As discussed earlier, low κ is vital to obtain good thermoelectric performance.

κ_e of a material is related to σ by the Wiedemann-Franz Law, as defined in Equation (1.16).

$$\kappa_e = L\sigma T \qquad \text{Equation (1.16)}$$

Where L is the Lorenz number, which is related to both temperature and carrier concentration. A value of 2.4 10^{-8} W Ω K^{-2} for is often used for metals and degenerate semiconductors. Whereas, a value of 1.6 10^{-8} W Ω K^{-2} is calculated for half Heusler compounds, [25] which are the main focus of the work presented in this thesis.

Here, another conflict appears, since increasing σ will lead to an increase in κ_e. For this reason, much work has focussed on reducing the lattice component of the thermal conductivity, as it is independent from the electronic structure. κ_{lat} can be given by Equation (1.17). [26]

$$\kappa_{lat} = \frac{1}{3} C_p \upsilon L = \frac{1}{3} C_p \upsilon^2 \tau \qquad \text{Equation (1.17)}$$

Where C_p is the heat capacity under constant pressure, υ is phonon velocity and L is the phonon mean free path, which is related to the phonon relaxation time, τ, through the phonon velocity ($\upsilon = L/\tau$).

Therefore, two approaches can be used to reduce κ_{lat}. The first one is related to low phonon velocity, υ, which can be found in materials with high density, but soft bonds. The second approach relies on decreasing τ through increasing phonon scattering. Phonons can be scattered via various mechanisms. These include, Umklapp (phonon-phonon) scattering, point defects scattering and boundary (interfaces) scattering. [27] Point defect scattering can be realised in materials that contain mass or strain fluctuations within the lattice, and this usually observed upon alloying (site substitution). [28] Meanwhile, boundary defect scattering is mainly observed in nanostructured materials. [29]

1.5. Electronic Properties of Solids

There are two approaches that are commonly used to describe bonding in solids. The first one is the free electron model, which regards a metal as a box, inside which the nuclei and core electrons are fixed, while the outer electrons (valence electrons) move freely within the solid. Assuming that the solid has N valence electrons, these electrons (in pairs) will start to fill up the states from the lowest to the highest energy level, until all the electrons are used up. The highest occupied energy level at absolute zero is known as the Fermi level, E_F. The number of states that are available for electrons to occupy at a given energy is known as the density of states (DOS). The density of states usually increases with increasing energy as shown in Figure 1.6.

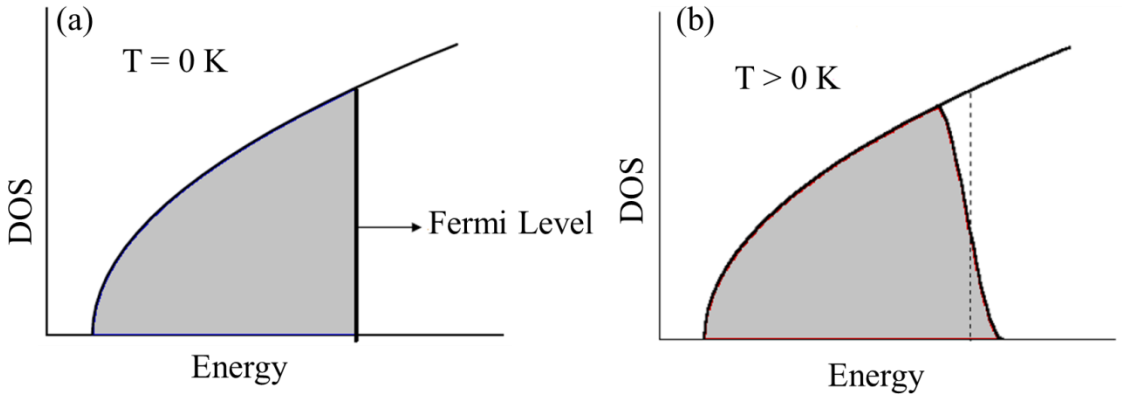

Figure 1.5. Density of states curves based on the free electron model. The shaded region in (a) represents the density of states at T = 0 K, while in (b) is the density of states at finite temperature. [30]

In Figure 1.5(a), the levels occupied at absolute zero are shaded. However when temperature increases from 0 to T, some electrons can be thermally excited and jump to occupy levels above Fermi level, as illustrated in Figure 1.5(b).

However, it is more realistic to consider the case where the electrons are affected by the atomic nuclei and by each other. This case is known as the nearly free electron behaviour and the electron will have then a periodic potential, as it is affected by the periodic lattice. One of the principle consequences of the periodic potential is the appearance of band gaps (no allowed electron states). Moreover, the nearly free electron model enables us to distinguish between metals, semiconductors and insulators based on their band structure. This illustrated in Figure 1.6.

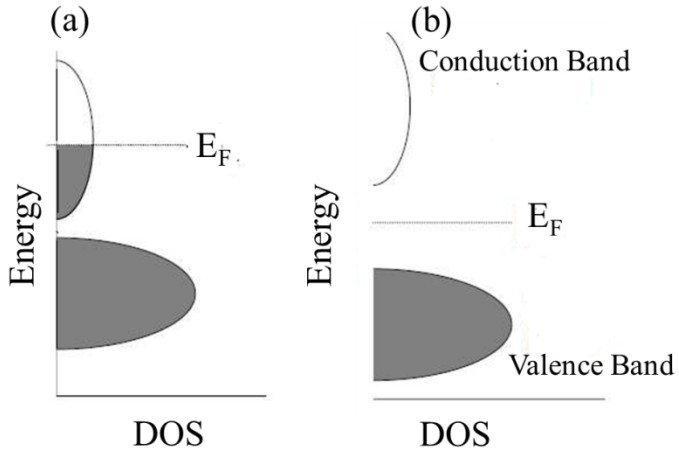

Figure 1.6. Band structure for metals (a), semiconductors and insulators (b). [30]

In metals, the conduction band is partially filled and empty energy states available for electrons just on top of the highest occupied energy level, therefore, electrons can migrate easily through this band, making metals good conductors. However, in semiconductors and insulators the conduction band is completely empty and a band gap between the conduction and valence bands exists (Figure 1.7(b)). The difference between semiconductors and insulators can be made based on the size of this gap, in which, smaller band gaps are observed in semiconductors.

At low temperatures, semiconductors appear to be insulators. However, their conductivity can be controlled by either increasing temperature (electrons will be thermally promoted from valence band to the empty conduction band) or adding impurities (doping). A semiconductor with no impurities is usually referred to as intrinsic semiconductor, in which the number of holes in the valence band equals the number of electrons in the conduction band. At a given temperature, narrow gap

semiconductors will have higher concentration of intrinsic carriers as compared to the wide gap materials. However, when impurities (dopant) are intentionally added, the semiconductor is then known as extrinsic semiconductor. If the impurity has one more electron than the host atom, a donor state will be produced near the bottom of the conduction band, generating n-type semiconductor. If the dopant has fewer electrons than the atom it replaces, an acceptor state will be created near the top of the valence band and this produces p-type semiconductor. In both cases, the conductivity of the host material increases. A diagram of donor and acceptor states in a semiconductor is illustrated in Figure 1.7. [31]

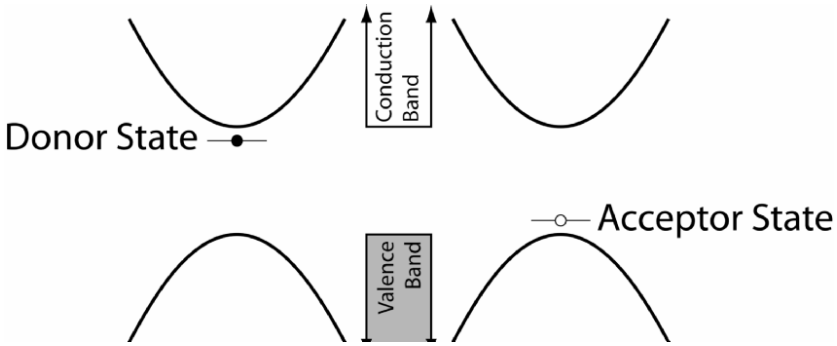

Figure 1.7. Diagram of donor and acceptor states in a semiconductor upon doping. [31]

The second approach used to describe bonding in solids is using molecular orbital theory. In this approach, the solid is considered as very large collection of atoms that are bonded together. Molecular orbitals are formed by combining the atomic orbitals, in which bonding and antibonding orbitals are formed. The bonding orbitals are lower in energy than the antibonding orbitals, where the energy difference between them depends on the degree of overlap of the atomic orbitals. As the number of atoms increase, the number of levels increase, however, this will only produce a very small increase in energy, in which a very large number of states can be found within a small range of energies. [32] This is illustrated in Figure 1.8. A distinction between metals, semiconductors and insulators can be also made based on this theory.

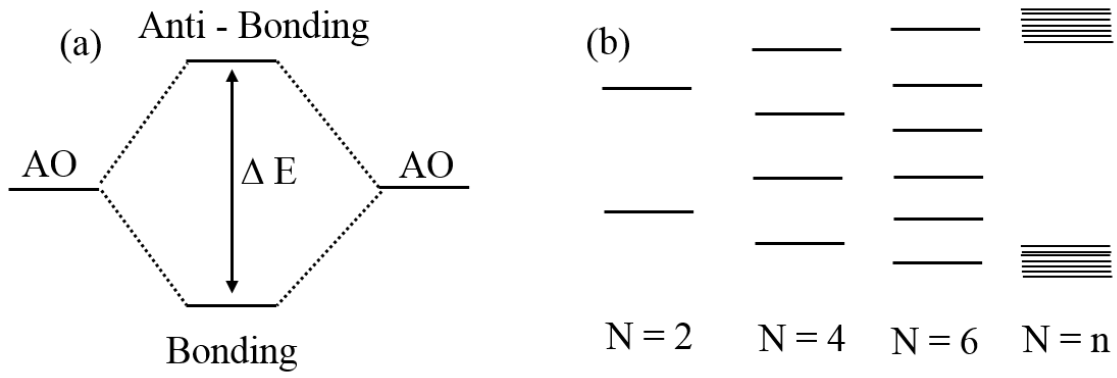

Figure 1.8. The formation of bonding and antibonding states upon the combination of two atomic orbitals (a), and in (b) energy band formed from the combination of (n) atomic orbitals.

1.6. Optimizing *ZT*

As discussed in Section 1.3, for practical applications, thermoelectric materials should have $ZT \geq 1$ and that requires large S, high σ and low κ. However, these properties are strongly coupled and cannot be optimized separately. Attempts at maximizing ZT involve either maximising $S^2\sigma$ and/or minimising κ. These include optimizing current materials, investigating nanoscale materials or developing entirely new classes of materials, which is very challenging and requires a good collaboration between theoretical and synthetic chemists. [18] These approaches will be discussed in more details in the following sections.

1.6.1. Increasing the power factor, $S^2\sigma$

As mentioned before, obtaining a large power factor means that high electrical power will be generated. However, improving $S^2\sigma$ of a thermoelectric material requires optimizing both S and σ, or increasing one quantity while the other remains unchanged, yet these two quantities are interrelated and they depend strongly on the electronic structure of the material. Enhancements of $S^2\sigma$ have been gained through doping as well as nanostructuring. These are discussed in more detail in the following sections.

1.6.1.1. Bandstructure Engineering

Recent improvements in ZT have been achieved in bulk thermoelectric materials using bandstructure engineering strategy, which affects primarily S and σ. [33] As discussed in Section 1.4.1, a high S can be due either to a high band degeneracy (high N_v) or by a high band effective mass m^*_b. Doping can be used to tune m^*_b. This has been demonstrated in I and La-doped PbTe. [34] In this study, the La-doped PbTe showed higher S values due to higher m^*_b, as compared to the I-doped PbTe. However, the

higher m^*_b in the La-doped PbTe resulted in a lower mobility and therefore a net decrease in $S^2\sigma$ compared to the I-doped PbTe. In general, band degeneracy has no significant influence on mobility, and thus increasing N_v can be used as a promising approach to increase $S^2\sigma$. Increased valley degeneracy has been proven in the $Mg_2Si_{1-x}Sn_x$ solid solution at x = 0.7, which led to a significant increase S and ZT values, as compared to other x values. [35]

1.6.1.2. Nanostructuring

Recently, efforts are targeting nanostructured materials as a promising approach to vary S and σ independently, and thus maximising the power factor $S^2\sigma$. In 1993, Hicks and Dresselhaus [36] predicted that these nanostructured materials could have a significant increase in the ZT, resulting from introducing sharp peaks in the density of states and therefore enhancing S. A comparison of the density of states for a bulk semiconductor (3D), layered materials (2D), nanowires (nano-tubes) (1D) and nano-particles is illustrated in Figure 1.9. [37] Soon, thereafter, the validity of this concept was experimentally proven in thin films (2D) structures based Bi_2Te_3-Sb_2Te_3, [38] Bi nano-wires (1D) [39] and quantum dot structures (0D) such as the PbTe-PbS system. [40] Although these nanostructured materials have revealed significant increase in the ZT values compared to bulk materials, they are expensive and difficult to fabricate on large scales, and they have poor thermal and mechanical stability. All of these issues make them not suitable for commercial applications. However, the concept of nanocomposites (nanoparticles embed in a bulk host material) has been introduced as an effective solution for these problems. Significant reduction of κ has been achieved in theses nanocomposites, yet the electronic transport is not well understood and only very few improvements in their electronic properties have been obtained. [3]

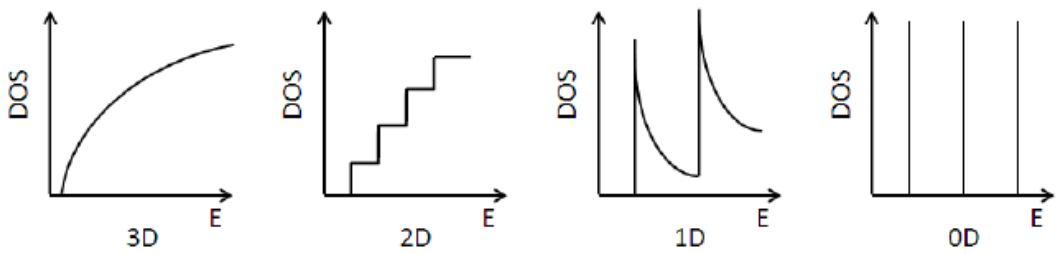

Figure 1.9. The density of states for a bulk semiconductor (3D), layered materials (2D), nanowires (nano-tubes) (1D) and nano-particles (0D).

1.6.2. Reduction of the Thermal Conductivity, κ

Most of the recent enhancements of ZT have been linked to a reduction of κ_{lat}, as it is the only quantity not determined by the electronic structure of the material. Several approaches that have been used to reduce κ_{lat} are discussed in the following sections.

1.6.2.1. Alloying

As discussed in Section 1.6.1, doping of a small amount of impurities has been known as an effective strategy to enhance charge carrier concentration and hence increase $S^2\sigma$ at the same time, however, the dopant can also act as point defect and induce strong phonon scattering, which in turn lead to a reduction in κ_{lat}. However, reduction of κ_{lat} should be more efficient upon using much higher fractions of dopant (alloying). For example, alloying Bi_2Te_3 with Sb_2Te_3 or Bi_2Se_3 remarkably reduces the κ to about half that of the parent compound. [41] In some case, alloying can affect the electronic structure leading to enhancements in $S^2\sigma$. This was observed in the $Si_{0.15}Ge_{0.85}$ alloy as a consequence of a higher density of state effective mass and thus higher S values, as compared to the pure elements. [42] Furthermore, Isoelectronic alloying in half Heusler compounds has been extensively used in order to reduce κ_{lat} through mass fluctuation effects, while preserving the electrical properties.

1.6.2.2. Phonon Glass Electron Crystal (PGEC)

A very promising approach was proposed by Slack [43] and is referred as the "Phonon Glass Electron Crystal" (PGEC) concept. According to the (PGEC) approach, a good thermoelectric material should have the electrical properties of a crystalline material, while phonons should be disrupted like in an amorphous or glass-like material. These unusual properties can be found in materials with very complex structures, in which the crystal structures contain voids or tunnels that can accommodate atoms or group of atoms of small enough size to rattle. In this case, phonons are scattered by these rattling atoms, leading to large reduction of κ. Therefore, with this approach, high $S^2\sigma$ and low κ can coexist in a single material. This has been successfully demonstrated in Clathrate [44] and Skutterudite [45] based compounds.

1.6.2.3. Nanostructuring

In addition to the previous approaches, phonons can be scattered effectively at interfaces. This has been proven in many nanostructured materials, nanocomposites and multiphase compounds, which are discussed in more detail in Sections 1.7.1.2 and 1.7.1.4 for HH systems.

1.6.3. Current Thermoelectric Materials

To date, great progress has been made in the field of thermoelectric materials research. This includes advances in both theory and experiments. Various materials with very promising properties have been identified. However, several issues are still present, restricting the wide commercial use of this technology. Nevertheless, a brief description of the most promising thermoelectric materials is given in the following sections. The temperature dependence of *ZT* for various bulk thermoelectric materials is given in Figure 1.10.

1.6.3.1. Chalcogenides

Historically, by considering the conditions of having high mean atomic weight and large *S*, group V chalcogenides attracted a lot of attention as promising thermoelectric materials. A famous member of this family is Bi_2Te_3, which is a narrow gap semiconductor, with *ZT* value of ~ 1 at 300 K. Thus, this material has been widely used for thermoelectric refrigeration since 1960. [46] Later, it was found that alloying Bi_2Te_3 with Bi_2Se_3 or Sb_2Te_3 could improve the thermoelectric performance, as discussed in Sections 1.6.1 and 1.6.2. In addition, PbTe and its alloys have also been intensively explored and they showed good thermoelectric properties at temperatures above those for Bi_2Te_3. [47] Also, the TAGS alloys ($AgSbTe_2$(80%)-GeTe(20%)) showed very promising properties, with a *ZT* value of 1.2 obtained at 400 K. This high *ZT* value was attributed to microstructure complexity, which led to exceptionally low κ_{lat} and thus high *ZT*. [48] However, due to the poor thermal stability of these alloys, they are not currently incorporated in thermoelectric devices.

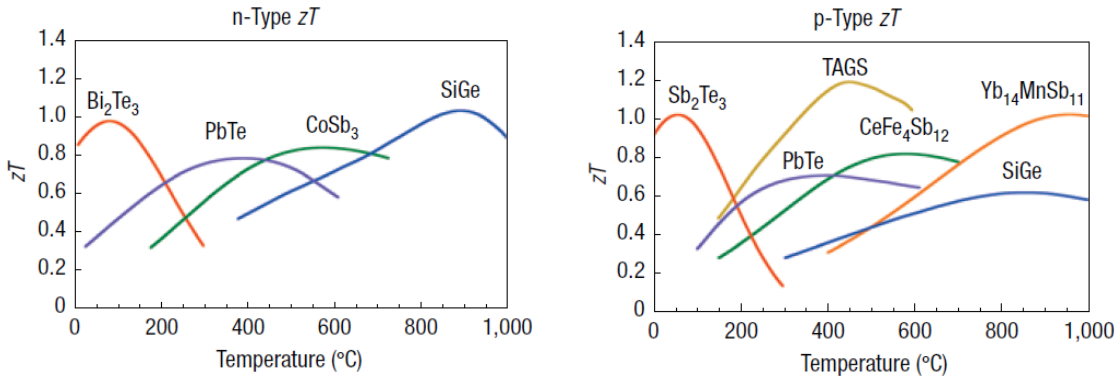

Figure 1.10. *ZT* as function of temperature for various bulk thermoelectric materials. [49]

1.6.3.2. Si-Ge Alloys

Although Si and Ge are not known to be good thermoelectric materials, however, their Ge-Si alloys have very low κ as well as high thermal stability and that makes them very good thermoelectric materials for high temperature applications. [50]

1.6.3.3. Clathrates and Skutterudites

The PGEC concept is successfully proved in materials with complex structures that contain voids or cages. These voids (cages) can accommodate atoms (ions) in such a way they are free to "rattle", leading to a dramatic decrease of κ. At the same time, these materials maintain their good electronic electrical properties; thus, the thermoelectric performance can greatly be enhanced. In some cases, the filling atom can act as electron donor or acceptor and thus optimize charge carrier concentration. Clathrates and skutterudites based compounds are typical examples of the PGEC materials. Filling the skutterudites $CoSb_3$ (Figure 1.11) with Ba, Ce or Y, remarkably reduces κ_{lat}, however, κ is further reduced and the electrical properties are even improved by substituting Co with Ni or Fe. A *ZT* value of 1.1 is obtained for the p-type skutterudites $Ce_{0.28}Fe_{0.15}Co_{2.5}Sb_{12}$ at 750 K, while a *ZT* = 1.25 is observed for the n-type skutterudites $Ba_{0.30}Ni_{0.05}Co_{3.95}Sb_{12}$ at ~ 900 K. [51] Ge based Clathrates also showed promising properties, where the Clathrate $Sr_8Ga_{16}Ge_{30}$ exhibited a κ lower than that of crystalline Ge by more than an order of magnitude. [52] These types of compounds are known as the Zintl phases, in which bonds within the structure are made up from both ionic and covalent contributions. This allows for a degree of independent optimisation of the electronic and thermal properties.

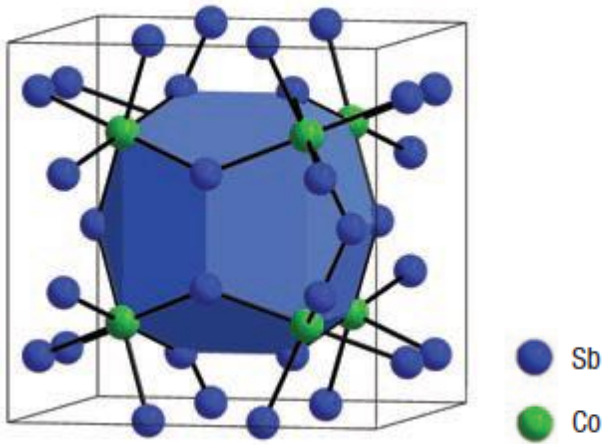

Figure 1.11. The crystal structure of skutterudites $CoSb_3$, consisting of octahedral of $CoSb_3$ creating large void spaces viewed in blue colour. [49]

1.6.3.4. Nanostructured Materials

From the above discussion, several bulk thermoelectric materials have been developed as well as a maximum $ZT \approx 1$ has been reported at different temperatures. However, this value is still not sufficient to allow the widespread commercial use of thermoelectric technology. Recently, low-dimensional systems have provided new mechanisms for increasing *ZT*. This can be found either in bulk materials containing nanoscale inclusions or in nanostructured samples themselves.

As discussed in Section 1.4.1, *S* can be optimized by reduced dimensionality as well as κ_{lat} can be greatly reduced through the strong phonon scattering at the internal interface. For instance, the combination of these two effects led to a maximum *ZT* value of 2.4 at 300 K for the thin film (2D) Bi_2Te_3-Sb_2Te_3 -based structures. [38]

Even though high *ZTs* have been reported in nanostructured materials, the difficulty in producing these materials on large quantities restricts them from being incorporated in TE devices. This, however, can be overcome by introducing the concept of nanocomposites, in which nanoparticles are randomly embedded into a bulk material (host). For instance, bulk nanostructured n-type SiGe can be prepared using ball milling technique, followed by hot pressing. This produces a peak *ZT* value of 1.3 at 1173 K, compared to a $ZT \sim 1$ for the bulk material. [53]

Also, a complex class of bulk materials known as LAST–m ($AgPb_mSbTe_{2+m}$, m = 10, 18) exhibited very interesting thermoelectric properties, and reached a ZT value of 2.2 at 800 K, making them suitable for high temperature applications. Precipitates of Ag-Sb nanoparticles as well as larger features were found in these alloys, leading to strong phonon scattering and thus significant reduction of κ_{lat}. [54]

Currently, many bulk nanostructured (nanocomposite) materials are under investigation, driven by the possibility of optimising the electrical transport properties, in addition to the expected reduction of κ_{lat} by the embedded nanoinclusions. [3]

1.7. Half Heuslers

One class of bulk thermoelectric materials which have been attracting a lot of attention as promising thermoelectric materials are the half-Heusler compounds. The first Heusler compound Cu_2MnAl was synthesised by Heusler in 1903. Currently, there are more than 1000 compounds known as Heulser and half Heuslers, in which their properties can be predicted by counting the number of their valence electrons. [55] HHs are ternary intermetallic compounds with a 1:1:1 stoichiometry. The general formula of these compounds can be written as XYZ, where X and Y are transition metals (or rare earth metals), while Z is a main group element. They crystallize in a cubic crystal structure (space group F-43m), where this structure is composed of three filled interpenetrating face centred cubic (fcc) sublattices and one vacant (fcc) sublattice. This structure can be viewed in different ways, highlighting the different type of chemical bonding. The crystal structure of a typical HH compound is displayed in Figure 1.12, in which X atoms are at 4b (½, ½, ½), Y atoms are at 4a (¼, ¼, ¼) and Z atoms are at the origin 4a (0, 0, 0), while the 4d (¾, ¾, ¾) site is vacant [56]. Different atomic arrangements are possible within this structure and this depends on the nature of the elements involved.

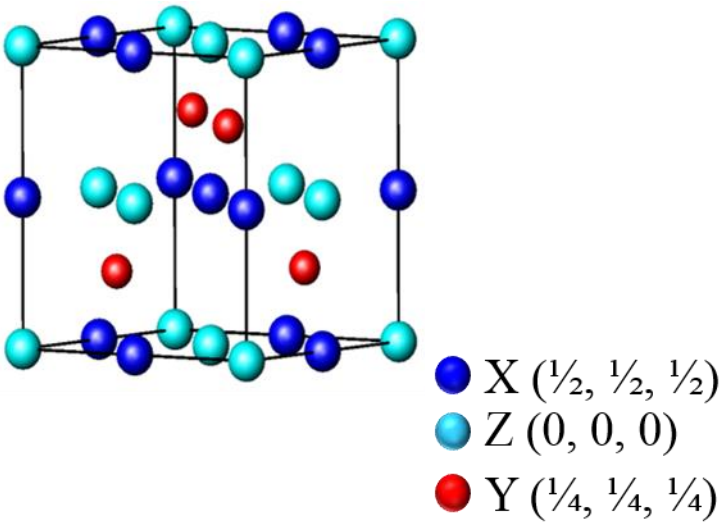

Figure 1.12. XYZ HH crystal structure.

Filling of all the tetrahedral sites results in a XY_2Z FH structure. As mentioned above, the properties of Heusler compounds depend strongly on their valence electron count (VEC). For example, a VEC = 27 gives rise to a superconducting behaviour, while the 17, 19 and 22-electron compounds are metals with weak ferromagnetism. Heusler compounds with VEC = 8 or 18 are semiconductors and very stable due to the closed shell configuration. Consequently, these compounds attracted a lot of attention as possible materials for thermoelectric applications. [55,57] Among these, XCoSb and XNiSn based compounds are the most investigated HH systems, as they show much promise. Generally, the thermoelectric properties of HH compounds can be optimized by changing their composition through the chemical manipulation of the three filled sublattices. For instance, very promising properties were obtained upon Ti substitution in the (Zr, Hf)NiSn based material. [58] The following section will discuss in detail the electronic structure and possible bonding models in the HH structure.

1.7.1. Electronic Structure

The chemical bonding within the HH structure is somehow complex and different models can be used to describe this bonding. The Zintl model is simply based on the electronegativity difference between the elements involved. In XYZ, X is the most electropositive element, thus the valence electrons of X are transferred to the Y and Z atoms to produce closed shell ions. For example, in TiCoSb, Ti gives up its valence electrons to Co and Sb and this produces Ti^{4+} (d^0) and make Co (d^{10}) and Sb (s^2p^6) closed shell ions. This explains the extraordinary stability of these compounds. However, several recent computational studies have indicated the presence of covalent bonding in HHs. [56,59] In this case, the HH structure can be described as a covalent zinc blende sublattice $(YZ)^{n-}$, filled with positive X^{n+} ions. However, some ionic bonding is still present in the (XZ) sublattice that makes up a NaCl-type sublattice. [60] Using the molecular orbital approach, the chemical bonding in the HH TiCoSb can be explained. Figure 1.13(a) illustrates the bonding in the $(CoSb)^{4-}$ substructure, where the fully occupied s and p states of Sb hybridise with the empty 5s and 5p orbitals of Co. This produces a set of bonding and antibonding states. In this case, the 3d states of Co do not hybridize with Sb orbitals. In addition to the ionic interaction between the $(CoSb)^{4-}$ structure and Ti^{4+}, the fully occupied (3d) orbitals of Co undergo a hybridisation with the empty 3d orbitals of Ti^{4+} (Figure 1.13(b)). Two sets of bonding and antibonding molecular orbitals are then formed, generating a weak covalent bonding. The bonding and antibonding states are separated by an energy gap. The highest occupied levels

(VB) have a strong Co contribution, while the lowest unoccupied states (CB) have a predominant Ti character. [55] Thus, HH phases can be considered as compounds, containing both ionic and covalent bonds, and this is keeping with the Zintl concept. [61]

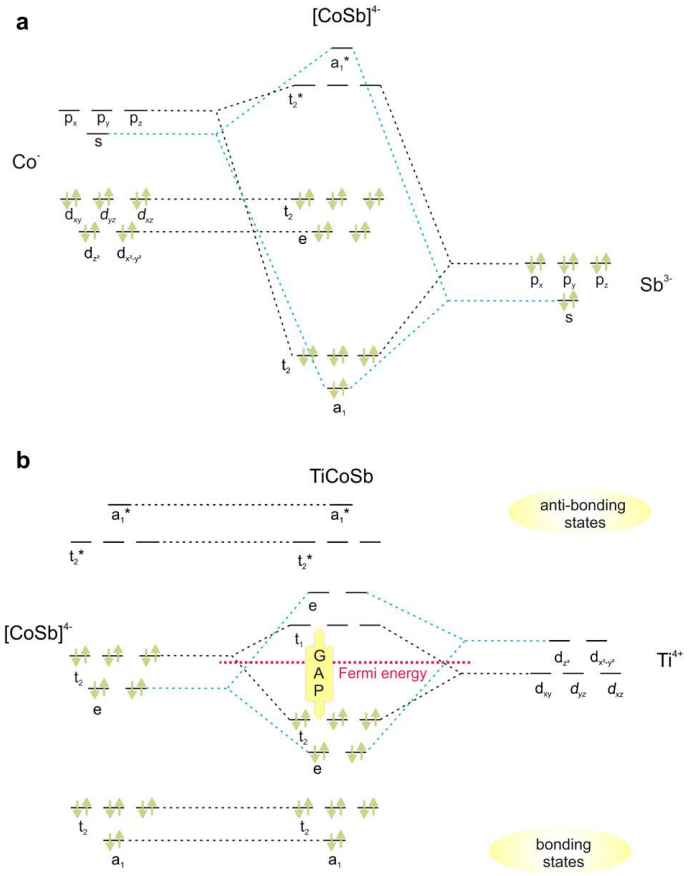

Figure 1.13. The chemical bonding in TiCoSb based on the molecular orbital approach. (a) represents the bonding in the $(CoSb)^{4-}$ substructure, while (b) depicts the interaction between $(CoSb)^{4}$ and Ti^{4+}. [55]

DOS calculations for TiCoSb confirm the hybridisation between d-states of Co with p-states of Sb and d-states of Ti. Moreover, the calculations show that the energy states above Fermi level (CB) are determined by Ti d-states, while the states below Fermi energy (VB) consist mainly of Co d states. This is illustrated in Figure 1.14. [62]As mentioned earlier, the size of the band gap depends on the difference between the bonding and antibonding states and this in turn depends on the difference in the electronegativity between the transition metals involved (X, Y). Generally, as the difference in electronegativity increases, the band gap increases. For instance, TiNiSn has a theoretical band gap of 0.42 eV, compared to a value of 0.95 eV for TiCoSb. The calculated band gaps can differ from the experimental ones, as the gap values are affected by lattice disorder. [59,63]

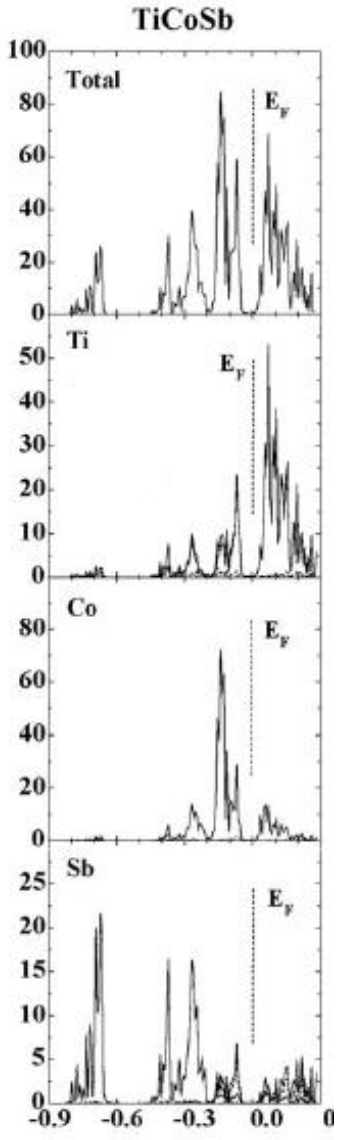

Figure 1.14. The total and partial calculated electronic density of states for TiCoSb. [62]

1.7.2. Half Heuslers for Thermoelectric Applications

Recently, the 18 VEC HH systems based on XNiSn (n-type) and XCoSb (p-type) (X = Ti, Zr, Hf) have been attracting huge interest due to their high potential for different thermoelectric applications. As indicated earlier, these materials are semiconductors, with band gaps in the range 0.4-1 eV. In addition, undoped XNiSn and XCoSb have sharp feature in (DOS) near E_F, leading to large S values. They also exhibit low room temperature resistivities (10^{-1}-10^{-3} Ω cm). [64] Experimentally, the n-type XNiSn exhibit larger power factors compared to the p-type XCoSb materials. This can be explained based on the fact that electrons have higher mobilities than holes in these materials. [65] Maximum *ZT* values for some XNSn/XCoSn systems are provided in Table 1.1. Furthermore, HHs are relatively easy to synthesise and contain low cost,

environmentally friendly and earth abundant elements. The key issue with HHs is their relatively high thermal conductivity, which reaches a value of ~ 10 Wm^{-1} K^{-1} at room temperature. This is nearly 5 times higher than that of commercial Bi_2Ti_3. Currently, enormous scientific effort is being made to reduce this high thermal conductivity, while maintaining the large power factors. [66] The thermoelectric properties of HHs can be enhanced by alloying/doping on each site individually. Thus, a wide variety of HH materials can be produced from one starting composition. It is possible, for example, to enhance charge carrier concentration by doping with non-isoelectronic elements (usually on the Z position). Whereas, isoelectronic substitution results in mass fluctuations effects, which in turn reduces κ_{lat}. For instance, combining these effects results in a *ZT* value of 0.7 for the $Zr_{0.5}Hf_{0.5}Ni_{0.8}Pd_{0.2}Sn_{0.99}Sb_{0.01}$ composition at 800 K. [67] TiNiSn-based compounds have been extensively investigated. Recently, however, materials based on TiCoSb have been receiving more attention, driven by the possibility to significantly increase their *ZT*. TiCoSb has a theoretical band gap of 0.95 eV, which is larger than most of other HH systems. [68] Therefore, the large energy gap value offers a space for enhancing the power factor, by raising the temperature of the onset of intrinsic carrier conduction. [55]

A reproducible *ZT* value of ~ 1, which is the benchmark for device applications can be then obtained in HHs by combining their large power factors, which are typically 1-6 mW m^{-1} K^{-2}, and reduced thermal conductivities. [65] However, the high temperature stability of these materials also plays a crucial role in integrating them in thermoelectric devices. The number of reports on the stability of HH systems is very small [69,70] and therefore more studies are highly desirable. In this thesis, a detailed study on the high temperature stability of TiCoSb will be provided in Chapter 3.

Table. 1.1. Overview of reported maximum *ZT* values for selected XNiSn and XCoSb HH compounds.

Composition	*ZT*
TiNiSn	0.4 at 775 K [25]
TiCoSb	0.008 at 400 K [71]
ZrNiSn	0.5 at 850 K [25]
HfNiSn	0.48 at 1000 K [72]

1.7.3. XCoSb–Based Compounds

As discussed in Sections 1.6.1 and 1.6.2, several strategies can be used for enhancing *ZT* values for thermoelectric materials. Significant improvements have been reported for both XNiSn-based and XCoSb-based (where X = Ti, Hf or Zr or a combination of these elements) HHs. However, as this work investigates TiCoSb-based HHs, the following sections will focus more on the enhancements of *ZT* that have been reported in TiCoSb-based compounds.

1.7.3.1. Chemical Substitution in TiCoSb

The unique structure of HHs offers the possibility to dope each of the three occupied fcc sublattices individually for tuning charge carrier concentration and thus enhancing the thermoelectric performance. Moreover, isoelectronic alloying in HH compounds can introduce mass and strain fluctuation, which can decrease κ. [66] For example, notable *ZT* values for p-type TiCoSb based-compounds are *ZT* = 0.03 at 988 K for $TiCoSb_{0.95}Sn_{0.05}$ and *ZT*=0.45 at 850 K for $TiCo_{0.85}Fe_{0.15}Sb$. [73,74] A larger *ZT* value of 0.3 was obtained for n-type $Ti_{0.92}Ta_{0.08}CoSb$ at 900 K. [75] Replacement of Co by Ni caused considerable increase in electron concentration and lead to a maximum *ZT* = 0.27 at 900 K for $TiCo_{0.95}Ni_{0.05}Sb$. [76] Substantial reductions in κ_{lat} have been reported for $TiCo_{0.5}Rh_{0.5}Sb$ and $Ti_{05.}Zr_{0.5}CoSb$ with room temperature κ_{Lat} of only one-third of that of TiCoSb. [77] In addition, a *ZT* value of ~ 0.51 was obtained for the n-type $Ti_{0.5}Zr_{0.25}Hf_{0.25}Co_{0.95}Ni_{0.05}Sb$ at 813 K and p-type $Zr_{0.5}Hf_{0.5}CoSb_{0.8}Sn_{0.2}$ at 1000 K , due to the combination of improved $S^2\sigma$ values and reduced κ. [80,81]

1.7.3.2. Phase Separation into Multiple Half Heusler Phases

Spontaneous phase separation has been observed in several XNiSn and XCoSb-based HH systems when they are cooled from melt. The mechanism of phase separation is still unclear. Recently, however, a few recent computational studies linked this phase separation to a poor demixing that occurs at low temperatures. [80,81] For example, the solid solution between TiCoSb (VEC = 18) and VCoSb (VEC = 19) is not stable at room temperature and needs temperatures in excess of 1073 K. Typical annealing temperatures are 1073-1173 K and phase separation into TiCoSb and VCoSb may therefore be an issue. This is illustrated in the phase diagram obtained by both mean field calculations and Monte Carlo simulation (Figure 1.15a), where a phase separated system is expected to form below ~ 1000 K. Also, snapshots from Monte Carlo simulation of $Ti_{1-x}V_xCoSb$, taken as the system is cooled down, are shown in Figure

1.15b. As the temperature decreases, demixing becomes more and more obvious, leading to the formation of Ti-rich and Ti-poor domains.

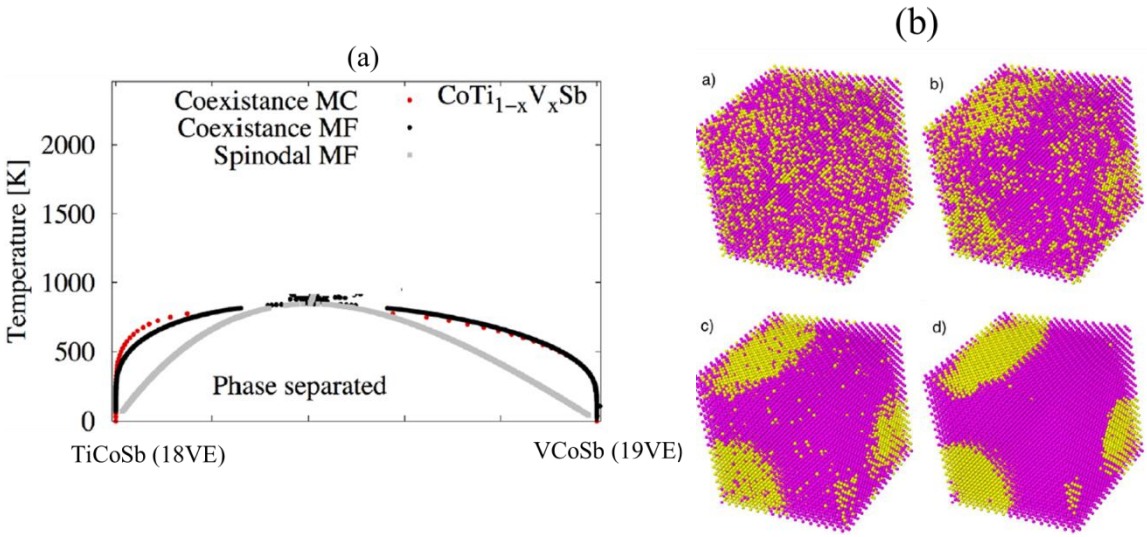

Figure 1.15. (a): Phase diagram created by mean field calculations and Monte Carlo simulation for $Ti_{1-x}V_xCoSb$. (b): snapshots from Monte Carlo simulation of $Ti_{1-x}V_xCoSb$ taken at (a) T = 1100 K, (b) T = 850 K, (c) T = 600 K, and (d) T = 350 K. Ti is shown in magenta and V is shown in yellow. [80]

It is expected that rapid solidification will shorten the reaction time as well as the diffusion distances, [82] which may lead to the formation of non-equilibrium phases that are kinetically trapped. Exceptional low κ has been found in the HH systems that exhibited an intrinsic phase separation, leading to promising *ZT* values. For instance, a *ZT* value of 1.2 at 830 K was obtained in the n-type (Ti/Zr/Hf)NiSn system, while maximum *ZT* values of 0.8-0.9 were realised in the p-type (Ti/Zr/Hf)CoSb systems. [83–85] An example of the resultant microstructure of the phase-separated $Ti_{0.5}Hf_{0.5}CoSb_{0.8}Sn_{0.2}$ is shown in Figure 1.16, where a phase separation into two HHs occurs: a dendritic structure consisting of a Ti-poor phase (II) and a Ti-rich phase (I). In addition to the reduction of κ, the phase-separated HH systems exhibited improved thermal stability, which was attributed to the high thermal stability of the resultant microstructure. [86]

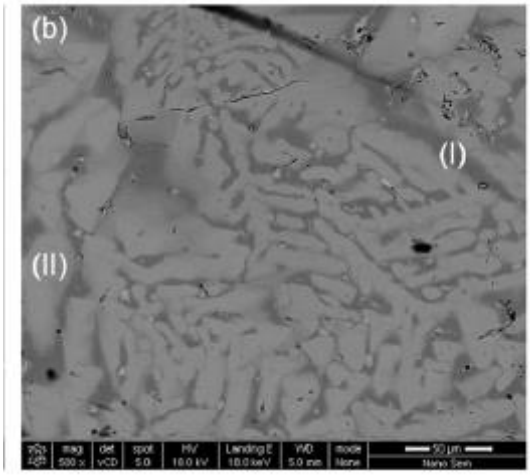

Figure 1.16. Secondary electron image of $Ti_{0.5}Hf_{0.5}CoSb_{0.8}Sn_{0.2}$, depicting the phase separation into two HH phases: a dendritic structure consisting of a Ti-poor phase (II) and a Ti-rich phase (I). [85]

1.7.3.3. Full Heusler and Zincblende Inclusions in Half Heuslers

Recently, it has been demonstrated that nanostructuring in HH compounds led to enhancement of the figure of merit in several cases. These involved materials with reduced grain size as well as nanoinclusions embedded into a host bulk HH matrix. The grain size reduction approach was applied for both n and p-type HH materials using ball-milling, followed by consolidation of the powders by hot-pressing or spark plasma sintering (SPS). This led to a peak *ZT* value of ~ 1 in the n-type $Hf_{0.75}Zr_{0.25}NiSn_{0.99}Sb_{0.01}$ and p-type $Hf_{0.44}Zr_{0.44}Ti_{0.12}CoSb_{0.8}Sn_{0.2}$ at 873K and 1073K, respectively, due to large reduction of κ_{lat} by increased phonon interface scattering. [87,88] However, when nanoinclusions are formed in situ into a micron-scale HH matrix, it is expected to enhance *ZT* through reducing κ as well as increasing the power factor. [66]. The segregation of FH nanoinclusions has been widely investigates in $XNi_{1+x}Sn$-based compounds, [89–91] but little has been done on XCoSb-based composites. However, three notable reports can be found in the literature. The first one investigates the p-type $Hf_{0.5}Ti_{0.5}Co_{1+x}Sb_{0.9}Sn_{0.1}$ nanocomposite (Figure 1.17a), [92] while the other two studies the XCoSb composite with in situ formed InSb nanoinclusions (Figure 1.17b). [93,94] As discussed in Section 1.7 HH and FH compounds have similar crystal structures. The only structural difference is that the vacant tetrahedral sites are filled with atoms in the FH structure. Moreover, the InSb inclusions have a zinc blende structure and this is also contained in the HH structure, where X and Y atoms form a zinc blende sublattice. The similarity in the structure between the FH and InSb and the HH suggests that formation

energy of the inclusions should be small, while the structural differences suggest that a solid solution cannot be formed. Consequently, this structural relationship favours the segregation of inclusions within the HH matrix. [65,89] The enhancement in $S^2\sigma$ through the embedding of nanoinclusions can be explained based on carrier filtering mechanism, where the metallic inclusions filter the low energy carriers, thus reducing charge carrier concentration, which leads to an increase in *S*. However, a simultaneous increase in carrier mobility can be achieved by the reduced electron-electrons scattering, which will then compensate the decrease in carrier concentration. [65] Experimentally, improvements in $S^2\sigma$ and reduction in κ_{lat} were achieved in the $Hf_{0.5}Ti_{0.5}Co_{1+x}Sb_{0.9}Sn_{0.1}$ nanocomposites, leading to a *ZT* value of 0.3 at 775 K for the x = 0.05 composition, compared to a value of 0.15 for the x = 0 composition at the same temperature. [92] Also, a maximum *ZT* value of 0.33 was obtained at 900 K for $TiCo_{0.85}Fe_{0.15}Sb$ containing 1% InSb nanoinclusions, and this corresponded to a ~ 450% enhancement over the nanoinclusions free sample. [93]

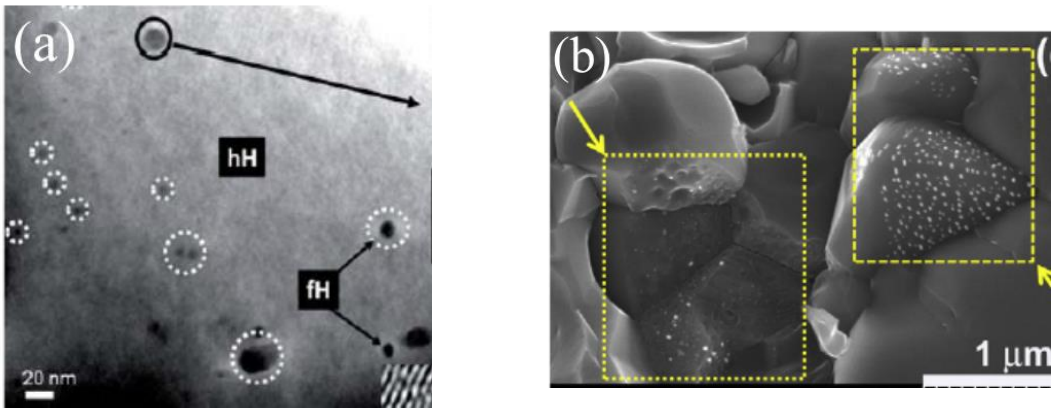

Figure 1.17. (a): TEM image of the $Hf_{0.5}Ti_{0.5}Co_{1.05}Sb_{0.9}Sn_{0.1}$ nanocomposite, showing spherical FH nanoinclusions (5-60 nm) dispersed in the HH matrix. (b): SEM image of the $TiCo_{0.85}Fe_{0.15}Sb$-15%InSb nanocomposite. The squared areas show large number of nanosegregated InSb inclusions. [92,93]

1.8. Aims and Objectives

The work presented in this thesis investigates the synthesis, structure and properties of three novel and distinct sets of TiCoSb-based HH thermoelectrics. Chapter 2 includes details of the synthesis methods and the principles behind the characterisation techniques used in the work throughout this thesis. Chapter 3 provides a detailed study on the high-temperature stability of the $Ti_{1-x}V_xCoSb_{1-x}Sn_x$ HH alloys. In Chapter 4, we report the first experimental observation of a change in carrier type in HH thermoelectrics induced by sample inhomogeneities. This is observed upon V, Fe and Sn substitutions in TiCoSb HH compound. Chapter 5 reports on the synthesis, structure and properties of $(TiCoSb)_{1-x}(TiM_2Sn)_x$ composites with x value ranging from 0 to 0.2 and M_2 = Fe_2, FeCo, Co_2, CoNi, Ni_2. These composites are expected to segregate into a HH matrix with TiM_2Sn FH inclusions.

Chapter 2–Experimental Methods and Theory

2.1 Introduction

A solid state chemistry experiment involves the solvent free synthesis of a solid product through reaction between solid reactants at elevated temperatures. This synthesis is usually followed by structural determination and physical property measurements using different techniques. There are therefore several steps included in a solid state chemistry project. This chapter will discuss the synthetic methods and characterisation techniques used throughout this thesis.

2.2 Synthesis Methods

Pure elements in the form of powders with a minimum purity of 99.5%, obtained from Alfa Aesar or Sigma-Aldrich, were used for the preparation of the samples in this thesis. Most samples were made via a conventional solid state reaction. However, a small number of samples were prepared by the arc melting technique. Both routes are discussed in more detail below.

2.2.1 Solid State Reactions

For all samples, stoichiometric amounts of the starting materials were mixed using an agate mortar and pestle, cold pressed into 13 mm pellets and then wrapped in tantalum foil. Samples were heated under vacuum in sealed quartz tubes at 850 °C with one intermediate homogenisation after 24 hours. More details on the annealing conditions used to prepare each series of samples are given in the relevant results chapters.

2.2.2 Arc Melting

An Edmund Buehler MAM-1 compact arc melter was used to synthesize a few polycrystalline HH compositions. Arc melting is a simple technique that involves the melting of elemental precursors in an electrical discharge under argon gas atmosphere. This technique can heat samples up to 3500 °C. Synthesis is therefore almost immediate. Stoichiometric quantities of the constituent elements were ground and cold pressed before they were mounted on a water-cooled copper plate in the arc melter. After initial melting, the resulting ingots were flipped and re-melted to ensure good homogenisation

.

2.2.3 Densification

Most of the samples presented in this thesis were subjected to a densification step by a simultaneous application of high temperature and pressure. [95] In general, cold pressed pellets have porosity of 60-80% of the theoretical density. This porosity leads to higher electrical resistivities and causes difficulties in measuring reliable thermal conductivities. Details of the hot press conditions used to prepare each series of samples are provided in the relevant results chapters.

2.2.3.1 Hot-Press

Hot pressing was performed using in-house equipment that uses an induction heating system, composed of an induction power supply (Flexitune) and a copper coil. The coil is positioned in the interior of a water-cooled chamber. The chamber can be filled with Ar gas and evacuated using a vacuum pump. The procedure included loading ~ 1.5g of powder in a graphite die with a diameter of ~ 13 mm. Graphite foil was used to prevent contamination between sample and upper/bottom spacer. A schematic of the setup is shown in Figure 2.1. Sample consolidation was carried out under Ar atmosphere and samples were held at the maximum temperature for 20 minutes.

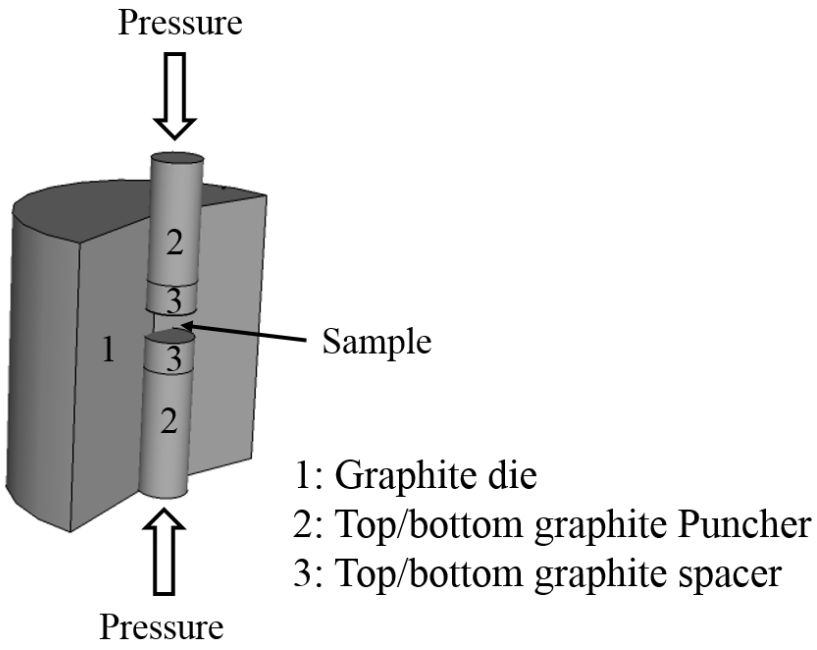

Figure 2.1. Schematic of the graphite die used in a hot press experiment.

2.3 Structural Characterisation

Structural data obtained from various physical methods is of a key importance to understand chemistry in the solid state. Three main physical techniques can be used to characterise solids: diffraction, microscopy and spectroscopy techniques However, diffraction experiments have been the dominant ones as they provide good knowledge of how the atoms are arranged within a structure. In this thesis, the crystal structures of the materials were determined using X-ray and neutron powder diffraction. Scanning electron microscopy and transmission electron microscopy were performed on selected HH compositions to further check the microstructure and homogeneity of these samples.

2.3.1 X-ray Diffraction

2.3.1.1 Generation of X-rays

X-rays are electromagnetic radiation of wavelength about 10^{-10} m. They were discovered by a German physicist, Wilhelm Rontgen in 1895. X-rays are typically generated when high energy electrons strike a metal target, often copper or molybdenum. The incident electron beam is able to expel electrons from the inner shell of the metal target, creating vacancies, which are filled by electrons falling from the shells above. The target metal emits a spectrum of white radiation and sharp, intense X-ray peaks caused by transitions of electrons within the atomic orbitals. For Cu, there are two types of electronic transitions: the 2p to 1s transition, called K_α with wavelength of 0.15418 nm and the 3p to 1s transition, called K_β with wavelength = 0.13922 nm. For diffraction experiments, a single wavelength beam of X–rays is required. Usually K_α is selected and all other wavelengths are filtered out. Generation of Cu K_α X-rays is demonstrated in Figure 2.2.

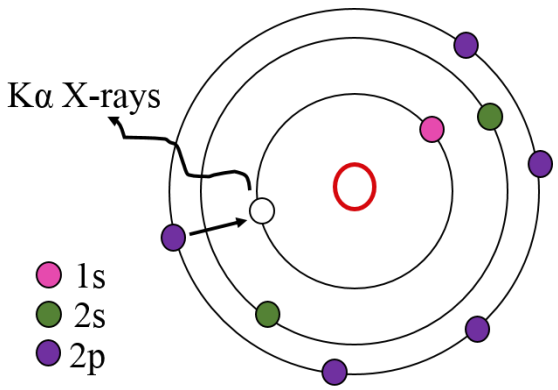

Figure 2.2. X-ray Generation. Reproduced from reference [30].

2.3.1.2 Diffraction of X-rays

Crystalline solids with their periodic internal structure are able to diffract X-rays with wavelength comparable to the inter-atomic spacing. X-rays, which can be treated either as a beam of photons or an electromagnetic wave, interact with the negatively charged electron cloud around the nucleus, and interference occurs between the scattered X-ray beams either constructively or destructively. If we consider a set of parallel planes of atoms within a crystal separated by a constant parameter, *d*, assuming that the diffraction of X-ray behaves like reflection from the planes of atoms at certain orientation of the crystal. Reflection will only occur if the scattered waves interfere constructively and this only takes place if the path difference between two waves reflected by atoms from adjacent planes is equal to a whole number of wavelength (Figure 2.3). This can be expressed by Bragg's law. [30]

$$\text{Path difference} = \text{CB} + \text{BD}$$

$$\text{Where CB} = \text{BD} = \text{d}_{\text{hkl}} \sin \theta_{\text{hkl}} \text{ and } \text{d}_{\text{hkl}} = \text{AB}$$

$$\text{and thus } Path\ difference = n\lambda = 2d_{hkl} \sin \theta_{hkl} \qquad \text{Equation (2.1)}$$

Where d_{hkl} is the spacing between layers of atoms, θ_{hkl} is the angle between incident/reflected beam and the surface of the crystal, λ is the wavelength of the incident rays, *h*, *k* and *l* are miller indices which are used to define crystal planes with respect to the unit cell edges, and n is an integer.

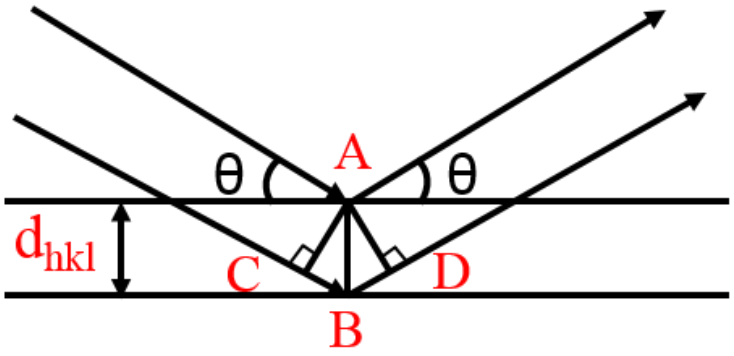

Figure 2.3. Schematic representation of Bragg's law. Reproduced from reference [30].

In the case of constructive interference, each set of parallel planes will give rise to a reflection at a particular Bragg angle. Interplanar spacing, *d*, of a set of planes can simply be calculated from Bragg's equation, if both λ and θ are known. This allows for the unit cell dimensions of a structure to be determined from any of the indexed reflections *hkl*. For example, for orthogonal crystals, where $\alpha = \beta = \gamma = 90^{\circ}$, the d-spacing can be obtained by applying Equation (2.2). [95]

$$\frac{1}{d_{hkl}{}^2} = \frac{h^2}{a^2} + \frac{k^2}{b^2} + \frac{l^2}{c^2} \qquad \text{Equation (2.2)}$$

Additional information on the crystal structure can be obtained from the intensities of the reflections. [32,96,97] This includes information on the arrangement of atoms in the entire crystal and hence bond lengths and angles. The intensity of the *hkl* reflections, I_{hkl} is proportional to the square of the structure factor F_{hkl}, which is the summation of scattering from N atoms in the unit cell to form an *hkl* diffraction peak. It is given by the general equation:

$$F_{hkl} = \sum_{1}^{N} f_n e^{2\pi i(hx_n + ky_n + lz_n)} \qquad \text{Equation (2.3)}$$

This equation can be re-written as:

$$F_{hkl} = \sum_{1}^{N} f_n \cos 2\pi(hx_n + ky_n + lz_n) + i \sum_{1}^{N} f_n \sin 2\pi(hx_n + ky_n + lz_n)$$

Equation (2.4)

Where f_n is the atomic scattering factor of the nth atom, x_n, y_n and z_n are the fractional coordination of this atom and *i* is the square root of -1.

The intensity of the X-rays scattered by one unit cell to give the *hkl* reflection is then:

$$I_{hkl} = |F_{hkl}|^2 \qquad \text{Equation (2.5)}$$

$$= \left\{\sum_{1}^{N} f_n \cos 2\pi(hx_n + ky_n + lz_n)\right\}^2 + \left\{\sum_{1}^{N} f_n \sin 2\pi(hx_n + ky_n + lz_n)\right\}^2$$

Equation (2.6)

Equation (2.3-2.4) shows that the diffracted beam has an amplitude and a phase, whereas the intensity is a scalar number.

The amplitude of a scattered wave is proportional to the atomic scattering factor f_n, which can be defined as the ratio of the scattering by an atom at a specific direction to the scattering by a free electron in the same direction. Therefore, the atomic scattering factor is unique for each element and increases with increasing number of electrons in the atom and hence with the atomic number, Z. It is also found that the atomic scattering factor varies as $sin\theta/\lambda$, where θ is the scattering angle. For $\theta = 0$, the atomic scattering factor, f_n, for the atom will be equal to its atomic number, Z. As the scattering angle increases, f_n will decrease due to increased destructive interference and this explains why the intensity falls off as θ increases.

An important effect to take into account is the thermal motion of atoms. Atoms vibrate depending on the temperature, causing the atomic electron density to spread out over a larger volume and then increasing the interference effects. For atoms which move equally in all directions, this effect is included by multiplying the stationary atomic scattering factor, f_n, of each atom by a term, as described in Equation (2.7).

$$f'_n = f_n . exp\left(-\frac{8\pi^2 U_{iso,n} sin^2\theta}{\lambda^2}\right) \qquad \text{Equation (2.7)}$$

Where $U_{iso,n}$ is an isotropic displacement parameter and measures the displacement of an atom about its mean position.

2.3.1.3 X-ray Powder Diffraction

Single crystal diffraction experiments are usually associated with a huge experimental challenge arising from the preparation of large single crystals, which is difficult or impossible in many cases. However, most solids can form crystalline powders and this led to the development of the X-ray powder diffraction technique by Debye, Scherrer and Hull in the early years of the 20th century. For this technique, the specimen must be ground to obtain a fine powder, which will contain large number of small crystals (crystallites) that are present in every possible orientation. Therefore, for each set of *hkl* planes, there will be some crystallites oriented at the correct angle to fulfill Bragg's law. The diffracted X-ray beam from those planes will make an angle of 2θ with the incident beam, and can be detected using a moveable detector connected to a computer or chart recorder. The setup of a powder diffraction experiment is shown in Figure 2.4.

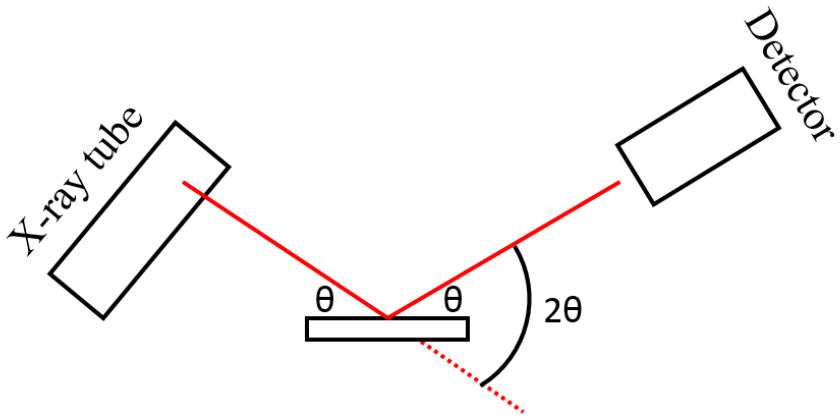

Figure 2.4. Schematic illustration of the powder diffraction method. Reproduced from reference [32].

In these finely powdered samples, the diffracted beam is emitted from the specimen as cones of *2θ* semi-angle radiation, often called Debye diffraction cones. [98] Each cone corresponds to a set of *hkl* diffracting planes and consists of a large number closely spaced dots, each dot depicts a diffraction from a single crystallite. In case of no preferred orientation (randomness), the diffracted intensity will be uniform within the cone, therefore, only one part of the cone needs to be recorded. Conversely, for a material with a preferred orientation (texture), intensity variations are usually observed along Debye cones and large parts of the cones have to be recorded. The formation of Debye cones of diffracted radiation is depicted in Figure 2.5.

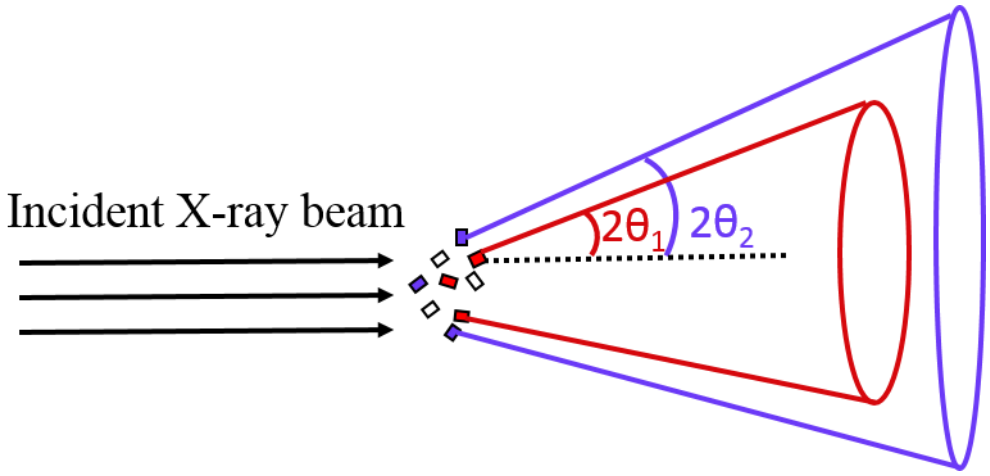

Figure 2.5. Illustration of Debye cones from diffracted radiation from a polycrystalline sample, where the red and purple colours correspond to diffraction from different d_{hkl}. [98]

Powder X-ray diffraction is a useful method for the identification of materials, where the powder diffraction pattern of an unknown compound is compared to those in a database that is regularly updated. It is also used for rapid quantitative analysis of

mixtures, following reactions and phase diagrams. Moreover, careful analysis of the positions and intensities of the peaks provides reliable information on unit cell dimensions and atomic positions. As the structure of the material becomes more complex, overlapping of reflections becomes an issue and leads to difficulty in indexing and measuring the intensities. Nevertheless, it is the most widely used technique for structural characterisation of inorganic solids.

2.3.1.4 D8 Advance

Laboratory X-ray powder diffraction patterns were obtained using a Bruker D8 Advance diffractometer, which uses a Ni-filtered Cu $K_{\alpha 1}$ radiation source (wavelength of 1.5406 Å) and a Lynxeye detector. A small quantity of a finely powdered sample (~ 20 mg) was used for each scan. Material was mounted on a sample holder and mixed with Propanol to prevent it from falling out of the sample holder. Phase identification was quickly carried out by running short scans of 30 minutes, collected over the range $20° \leq 2\theta \leq 70°$. For further analysis of the data with Rietveld method, subsequent long scans were collected over the range $10° \leq 2\theta \leq 120°$ for 8 hours.

2.3.2 Neutron Powder Diffraction

Neutron Powder diffraction is another powerful technique for probing the structure of polycrystalline materials. [30,99,100] It is complementary to X-ray powder diffraction and may be used when X-ray diffraction is inadequate. Unlike X-rays neutrons are mainly diffracted by the atomic nuclei through nuclear forces. A neutron powder diffraction pattern contains information on the atomic positions as well as the unit cell size of a given material.

2.3.2.1 Background

Neutrons in terms of their wave-like nature are similar to X-rays and thus they can be used for diffraction experiments. They are produced in two different ways, either by a nuclear reactor or spallation source. A reactor-based neutron source, such as the (ILL) in Grenoble, France, generates neutrons by the fission of ^{235}U nuclei. The released neutrons will have high energies in the range of MeV. These neutrons are then slowed to a suitable wavelength by collision in a moderating medium. For a structural diffraction experiment, a narrow distribution of wavelengths is selected using a single crystal monochromator. Therefore, this technique is a constant wavelength source, and the inter-planer separations, *d*, are determined by scanning through a range of θ and applying Bragg's law.

On the other hand, pulsed neutron beams can be obtained from accelerator-based sources (spallation sources) such as the ISIS facility in the UK. These sources are based on accelerating a beam of protons to a high energy that is enough to eject neutrons from the nuclei of a heavy metal target. The neutrons produced during this process will have high energies and they are slowed down to the required wavelength by passing into a moderator around the target. The neutron beam is finally passed into the beam tube, leading to the neutron scattering instruments. Each pulse contains neutrons of different velocities and hence wavelengths. This spreading of wavelengths is advantageous since neutrons with longer wavelengths travel at lower velocities compared to those with shorter wavelengths and their arrival time at the detector directly determines their wavelengths. Consequently, time-of-flight (TOF) diffraction experiments can be performed. In TOF based experiments, individual detectors are positioned around the sample at fixed angles so that the Bragg angle, θ, is kept constant. Neutron diffraction patterns are recorded as the number of scattered neutrons as a function of the time-of-flight of neutrons from the source, usually moderator, to the detector. The relation between the TOF and wavelength can be expressed as stated in Equation (2.8).

$$\lambda = \frac{ht}{ml} \qquad \text{Equation (2.8)}$$

Where t is the TOF, h is Planck's constant, m is the mass of a neutron, l is the path length, λ is the wavelength. The d-spacings are then calculated from the measured λ and the detector position (θ) by applying Bragg's equation. In this thesis, neutron powder diffraction experiments were carried out using the Polaris TOF diffractometer at the ISIS facility, UK, and this instrument will be discussed in more detail in Section 2.3.2.2.

Neutron and X-ray diffraction are in many ways analogous. However, there is a characteristic difference that arises from the nature of interaction of neutrons and X-rays with matter, which serves to make the two techniques complementary. Neutron scattering occurs mostly at the atomic nuclei, while X-rays diffraction involves interaction with the electron cloud surrounding each atom. This is advantageous in several ways. First, the scattering power, often called the scattering length, is dependent on the properties of the atomic nucleus and it varies randomly from element to element, rather than increasing linearly with atomic number. This means that light elements and also isotopes of the same element can be distinguished using neutron diffraction, while it is difficult to achieve this distinction with X-ray due to small electron density of light elements and similar scattering power of isotopes of the same element. Secondly, the

atomic nucleus is very small compared to neutron wavelengths and this explains why the scattering power for neutrons show no dependence of the scattering angle as it does for X-rays. Thirdly, neutron powder diffraction provides direct measurement of the atomic positions, whereas an electron density map is first obtained from an X-ray diffraction experiment, which is then used to deduce the atomic positions. Finally, Neutrons possess spin of ½ and they may interact with unpaired electrons of an atom leading to magnetic scattering. This enables the magnetic structure of a material to be analysed.

The nuclear structure factor is described in a similar way to that for X-ray scattering as given in Equation (2.3), with one exception that the atomic scattering factor is replaced with the nuclear scattering length (b), which is related to the coherent scattering cross section σ by Equation (2.9).

$$\sigma = 4\pi b^2 \qquad \text{Equation (2.9)}$$

It should also be mentioned that a relatively large size of sample is required to perform a neutron diffraction experiment since the intensity of the neutron beams are usually weaker compared to the intensity of X-rays.

2.3.2.2 Polaris

Neutron powder diffraction data were collected on several HH compositions prepared for this thesis using the upgraded Polaris diffractometer at the ISIS facility in Oxfordshire, UK. In this instrument, the sample position is at a distance of 12m from the moderator as well as a group of detectors arranged in 5 separate banks around the sample position. The strength of Polaris lies in the presence of large banks of individual detectors which provides high counting rate and therefore enables the rapid characterisation of materials or analysis of small sample volumes. A schematic of Polaris with the 5 banks presented in different colours is shown in Figure 2.5.

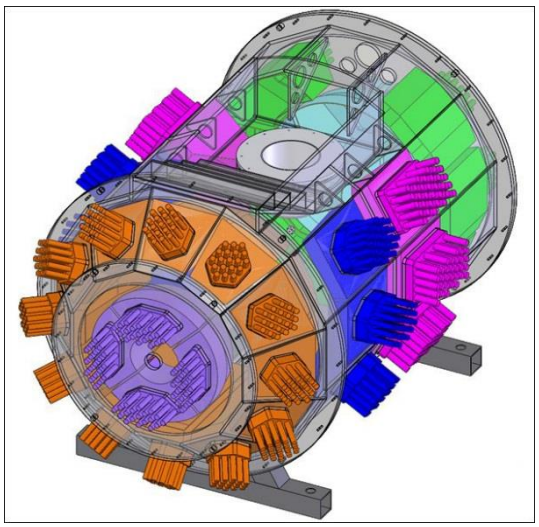

Figure 2.5. A schematic of the Polaris diffractometer at the ISIS. [101]

Experiments were performed at room temperature and they involved loading ~ 2 g of finely ground samples into cylindrical cans made of Vanadium foil. Vanadium is used as its scattering length for neutron is almost zero, making it nearly invisible to neutrons. Samples were loaded into a sample changer by the beam scientist Dr Ron Smith. Collection currents were in the range of 250-300 μA, corresponding to about 2-3 hours beam time. Mantid software was used to reduce the raw TOF data and subtract the instrumental background.

2.3.3 Diffraction Data Analysis

As discussed earlier (Sections 2.3.1 and 2.3.2), valuable information on the crystal structure of a material can be extracted from its measured powder diffraction pattern. Single crystal diffraction offers a full crystal structure determination of unknown crystal structures. By contrast, solving crystal structures from powder diffraction data is very difficult and this arises from Bragg reflection overlap, which makes it difficult to assign correct I_{hkl} intensities. As a result, crystal structures can only be refined (fitting a starting model to the observed data), which requires some knowledge of what the structure might look like.

2.3.3.1 Rietveld Refinement

Rietveld refinement is a very common method of refining crystal structures from powder diffraction data. [102,103] In the Rietveld method least squares refinements are carried out until a best fit is obtained between the observed data and a calculated model. The quantity minimised in this process is the residual S_y, as given in Equation (2.10).

$$S_y = \sum_i w_i (y_i - y_{ci})^2 \qquad \text{Equation (2.10)}$$

Where $w_i = 1/y_i$ is the weight assigned to each observed intensity, and y_i and y_{ci} are the observed and calculated intensities, respectively, at the ith step in the pattern.

Rietveld analysis is based on the idea that at each step, i, there is some information attached to the intensity, y. This may be negative information if there is no Bragg reflection, or that the intensity is the sum of contributions from several Bragg reflections. A key feature of Rietveld refinement is that a good starting model is needed as it is not a structure solution method.

2.3.3.1.1 Observed Intensities

In general, at any chosen point, i, in the diffraction pattern, the observed intensity is determined by summing the contributions from the background and neighbouring Bragg reflections. Each individual reflection has a height, width and shape which define its intensity, I_K, where K represents the Miller indices, h, k and l. As discussed earlier, the intensity, I_K, is proportional to the absolute value of the structure factor, $|F_K|^2$. The structure factor provides information on the atomic positions, site occupancies, scattering factors and thermal displacement parameters.

2.3.3.1.2 Calculated Intensities

Calculated intensities are determined from the structural model, considering contributions from both Bragg reflections and the background. The calculated intensity at a step, i, is obtained by applying Equation (2.11).

$$y_{ci} = s \sum_K L_K |F_K|^2 \phi(2\theta_i - 2\theta_K) P_K A + y_{bi} \qquad \text{Equation (2.11)}$$

Where s is the scale factor, L_K contains the Lorentz, polarisation and multiplicity factors, F_K is the structure factor, ϕ is the reflection profile function, P_k is a preferred orientation function, A is an absorption function and y_{bi} is the background intensity at the i^{th} step.

It is obvious from Equation (2.11) that Rietveld calculations include factors associated with both the sample and the instrument. All of these factors must be adjusted to minimise the residual S_y. Since the relationship between the adjustable factors and the intensity is not linear, it is necessary to start with a model that is close to the correct one. An incorrect or poor starting model may, however, converge, but it will lead to a false minimum.

2.3.3.1.3 The Reflection Profile Function, ϕ

Profile functions are used to model the shape of diffraction peaks. These contain both instrumental and specimen features, which vary as a function of *2θ*. These features usually affect the symmetry and width of the peak, and accommodating all of them in a single function is not trivial. For low-resolution, constant wavelength, diffraction data, peak shapes are easily fitted with a Gaussian profile function. The variation of the full width at half maximum (*FWHM*) of the Gaussian function with scattering angle is described by Equation (2.12).

$$FWHM^2 = Utan^2\theta + Vtan\theta + W \qquad \text{Equation (2.12)}$$

Where θ is the Bragg angle and *U, V* and *W* are refinable parameters. Though, for a high resolution diffractometer, the Gaussian profile function is not appropriate and a Pseudo-Voigt (*PV*) function may be used. This function is a linear combination of Gaussian and Lorentzian functions, as given in Equation (2.13).

$$PV = \eta L + (1 - \eta)G \qquad \text{Equation (2.13)}$$

Where η is the pseudo-Voigt mixing parameter, and it is a linear function of *2θ*, *G* is the Gaussian component and *L* is the Lorentzian component. The variation of the Lorentzian width as a function of Bragg angle is described by Equation (2.14).

$$FWHM = X\tan\theta + Y/\cos\theta \qquad \text{Equation (2.14)}$$

Where *X* and *Y* are refinable parameters and they relate to the particle size broadening and strain broadening, respectively.

2.3.3.1.4 Preferred Orientation Function, P_k

Preferred orientation occurs when there is tendency for the grains (crystallites) in a powder to be oriented along a specific axis, or set of axes. A material with layered structure provides an example, where the crystallites tend to align in a direction parallel to the sample holder. Preferred orientation usually leads to a systematic error in the measured intensities. Due to the systematic nature of this error, it can be mathematically modelled with the preferred orientation function, P_k.

2.3.3.1.5 Absorption Factor, *A*

Radiation may be absorbed while travelling through the specimen. This process affects the measured intensities. Absorption varies with the elements present (increases with atomic number) and the size and shape of the sample. It also depends strongly on the wavelength used and instrument geometry. These factors are modelled using the

effective absorption factor, *A*, which is usually taken to be a constant for a given geometry.

2.3.3.1.6 Background Intensity, y_{bi}

The background intensity at a step, i, may be obtained in three different ways. The first one is to select points between peaks and interpolate between them. The second is to use information files of operator-supplied tables with background intensities. The final way is to apply a specific background function.

2.3.3.1.7 Feedback

Rietveld refinement process will adjust the refinable parameters until a best fit of the calculated pattern to the observed one is obtained. Visual inspection of the pattern and fit is usually a very useful way to judge the goodness of the fit. Similarly, the difference curve gives a good indication of the progress of a refinement. In addition to these, there are some other statistical indicators which can be employed to determine how well the calculated pattern is fitted to the observed data. These are produced at each step of the refinement and can be defined in Equations (2.15, 2.16, 2.17, and 2.18).

$$R_p = \frac{\sum |y_i - y_{ci}|}{\sum yi} \qquad \text{Equation (2.15)}$$

$$R_{wp} = \sqrt{\frac{\sum w_i (y_i - y_{ci})^2}{w_i (y_i)^2}} \qquad \text{Equation (2.16)}$$

$$\chi^2 = \frac{\sum w_i (y_i - y_{ci})^2}{N - p + C} \qquad \text{Equation (2.17)}$$

$$R_F = \frac{\sum \left| (I_{K(obs)})^{1/2} - (I_{K(cal)})^{1/2} \right|}{\sum (I_{K(obs)})^{1/2}} \qquad \text{Equation (2.18)}$$

Where I_K is the intensity of the Kth Bragg reflection at the end of the refinement cycles, w_i is a statistical weight, and $(N - p + C)$ represent the number of degrees of freedom where N is the total number of observations, p is the number of parameters being refined and C is the number of constraint applied in the refinement.

R_p and R_{wp} are the profile and weighted profile R factor, respectively and they are used to evaluate how well the peaks are fitted. R_{wp} is considered as a direct measure of the residual being minimised. R_F is a structure factor comparable to that provided in literature on single crystal refinements. It is biased toward the calculated structure, but it can provide an indication of how reliable the structural model is. χ^2 is a numerical measure of goodness of fit between the observed data and the calculated model.

2.3.3.2 GSAS

All Rietveld refinement in this thesis were carried out using GSAS with its user interface, EXPGUI. [104,105] It is a set of programmes developed by A. C. Larson and R. B. von Dreele to process and analyse both single crystal and powder diffraction data obtained with X-rays or neutrons. It is also capable of handling multiple sets of data collected for a single sample simultaneously as well as analysing powder diffraction data containing a mixture of crystalline phases.

2.3.4 Electron Microscopy

Electron microscopy is a very powerful technique for studying structures over a wide range of magnification. [30,106,107] It includes several types of microscopes that operate in either reflection or transmission. In all types of electron microscopes, the sample under investigation is bombarded with high energy electrons, which will interact with atoms in the sample. This interaction generates a variety of signals that reveal information on the microstructural features of the sample. Like, X-rays, each element has a specific scattering power, f_e, that is approximately proportional to the atomic number and drops off as the angle of the incident beam increases. In contrast to X-rays and neutrons, electrons interact with matter very strongly and in a complex manner, thus it impossible to analyse scattering intensities in a similar way to that described in Section 2.3.3.1. Consequently, electron microscopy alone is not enough to fully solve a crystal structure, but it is a versatile instrument that offers a wide range of modes to reveal features that can not be detected using other techniques. Combining electron microscopy with other diffraction technique provides unique insight into the crystal structure of a given material.

Electrons are usually produced in the electron microscope by heating a metal filament (often tungsten). The electron beam is then accelerated by applying a potential. The wavelength of the electrons is directly proportional to the square root of the accelerating voltage, as given in Equation (2.19).

$$\lambda = \frac{h}{\sqrt{2meV}}$$ Equation (2.19)

Where h is Planck's constant, m and e represent the mass and charge of the electrons, respectively and V is the accelerating potential.

The electron beam is subsequently focussed and directed on the sample by applying magnetic fields. When the electrons strike the sample, several forms of scattering are produced. These include unscattered electrons, diffracted electrons, inelastically scattered electrons, secondary electrons and X-rays. The geometry of the measurement determines the type of scattered electrons to be analysed and thus control what information will be contained in the image. In general, the images can provide information on structure morphology, the distribution of element, defects, phase boundaries, texture etc. Three techniques were used for this thesis and will be discussed in more details in the following sections.

2.3.4.1 Scanning Electron Microscopy

Scanning microscopy is a type of reflection instrument used for viewing surface features at lengths scale down to 0.1-1μm. In this technique, an electron beam from a source is concentrated to form a very small probe, 50-100 Å in diameter. The probe is scanned across the surface of the sample to produce various types of signals (These are mentioned in Section 2.3.4). Signals that are mainly exploited in SEM are secondary electrons, backscattered electrons and characteristic X-ray photons. These are illustrated in Figure 2.6. Secondary electrons are generated from within the sample and travel at velocities that correspond to low energies (< 50 eV). These secondary electrons are detected above the sample, and an image of the sample surface is obtained. Backscattered electrons are scattered through large angles, with energies greater than 50 eV. X-rays are ejected from the sample and are used for chemical analysis (this will be discussed in more detail in Section 2.3.4.3).

In general, secondary electrons have a smaller interaction volume compared to the backscattered ones and this leads to the fact that secondary imaging has a better resolution. Secondary mode normally forms topographic images, while backscattered images can be either topographic or compositional. The latter is related to the atomic number of the scatterer and hence compositional contrast can be observed within the sample. Areas of high atomic number will appear bright compared to areas of low atomic number.

Scanning electron microscopy may require some preparation of the surface to be examined. It could involve polishing the surface if it is very rough or coating the surface of insulating materials with a thin layer of metal, such as gold, to prevent charge build up that can ruin the image.

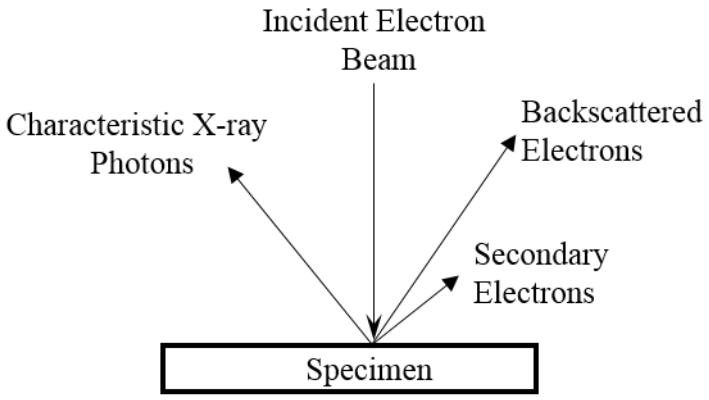

Figure 2.6. Types of electron scattering from a bulk specimen generated during a scanning electron microscopy experiment. Reproduced from reference [107]

2.3.4.2 Transmission Electron Microscopy

In transmission electron microscopy, the image is formed by electrons that transmit through the sample. This technique offers better resolution compared to scanning microscopes and is capable of examining features of diameter less than 1μm. The basic requirement for this technique is that the sample must be thin enough to allow electrons to penetrate some part significantly. In practice, sample thickness should be less than 0.2 μm. Thinning techniques, such as ion bombardment, are used when it is difficult to prepare thin samples. The wavelengths of the diffracted electrons are smaller than that of X-rays. As a result, diffraction occurs at relatively low angles and it is dominated by heavy atoms. The diffracted beams are focussed using either electric or magnetic field and an image of the sample can be seen on a viewing screen. These images provide very useful information on boundaries, defects, dislocations, amongst other. On the other hand, a diffraction pattern, similar to that of X-rays and neutrons, can be formed by choosing a specific set up.

2.3.4.3 Analytical Electron Microscopy

X-rays emitted during electron-sample interactions are of great importance for performing chemical analysis of selected regions of the solid. The energies of the emitted X-rays are characteristic of the elements in the sample. Energy dispersive spectrometer is used to separate the wavelength or energy of the emitted X-rays and

thus determining which elements are present in the sample. These techniques are often called wavelength dispersive and energy dispersive X-ray analysis (EDX), respectively. Moreover, the chemical composition of small areas on the sample can be found using EDX analysis. This is done by determining the peak intensities that are related to the relative amounts of the constituent elements. For thin samples the relation is described as:

$$\frac{C_x}{C_y} = \frac{I_x}{I_y} \qquad \text{Equation (2.20)}$$

Where C_x is the concentration and I_x is the peak intensity for element x. This quantitative analysis is not applicable to elements with low atomic number (Z < 10).

AEM is usually combined with TEM or SEM to generate elemental maps that are very valuable for studying inhomogeneous materials.

2.3.4.4 Experimental set-up

Scanning electron microscopy (SEM), Transmission electron microscopy and energy dispersive X-ray analysis were performed on several HH compositions prepared for this thesis. SEM measurements were performed using a Quanta 650 FEG scanning electron microscope. The microscope is equipped with an Oxford instruments X-max^N 150 EDX detector. Quantitative analysis of selected areas was carried out using the Aztec Large Area Maps software. Prior to analysis, samples were polished using fine Al_2O_3 sandpaper down to 0.5 micron roughness. In order to remove any aluminium oxide that became stuck to the surface, the polished samples were sonicated for 30 minutes using a Fisherbrand ultrasonic bath. Measurements were carried out by Dr. James Buckmann (Heriot Watt University). TEM measurements were performed on a JEOL ARM 200cF instrument operating at 200kV and using a Bruker XFlash detector. TEM data collection was undertaken by Dr. John Halpin at the University of Glasgow.

2.4 Physical Properties

Physical property measurements are a fundamental step to examine the effects of making modifications to materials being investigated. In the thermoelectric field, these properties are ρ, S and κ. All of these properties were measured where possible for the samples investigated in this thesis.

2.4.1 Electrical Resistivity

The resistivity of a material can be defined in terms of its resistance using Equation (2.21).

$$\rho = \frac{RA}{L} \qquad \text{Equation (2.21)}$$

Where ρ is the resistivity (Ω m), R is the resistance (Ω), A is the cross section area of the material and L is the length of the material.

The 4 terminal method was used to measure ρ at various temperatures. In this method, a constant electrical current is applied through the outer contacts and the change in voltage is measured across the inner contacts. The great advantage of this method lies in the fact that it eliminates contact and lead resistances and therefore yields accurate measurement of R especially for materials with low ρ such as metals. Figure 2.7 represents the measurement setup of the 4 terminal method.

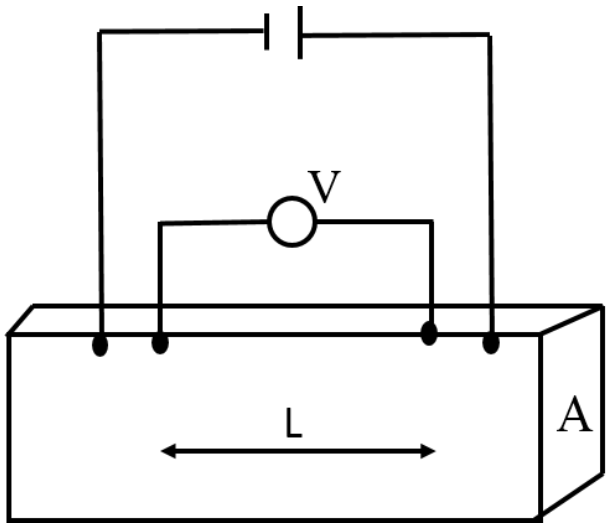

Figure 2.7. Schematic representation of electrical resistance measurement by the 4 terminal method.

Rectangular bars were cut from the hot-pressed samples using a low speed diamond saw. Resistance measurements were performed between room temperature and a maximum temperature of 823K using a Linseis LSR-3 instrument (Figure 2.8). The bar is vertically positioned between 2 platinum electrodes and two platinum thermocouples are pressed against the sample to measure voltage and temperature gradient. In this case, the distance between the 2 thermocouples replaces the length L in Equation (2.21). The whole measuring arrangement is located in a furnace that heats the sample to a specific

temperature, while a secondary heater in the lower electrode block generates a temperature gradient. All of these measurements were performed under a He atmosphere.

2.4.2 Seebeck Coefficient

S(T) measurements were carried out simultaneously with the *ρ(T)* measurements using the Linseis LSR-3 instrument. The setup of the measurements is the same as described above. For this thesis, the Seebeck measurement involved applying a temperature gradient of 30 K between the upper / lower electrodes (Figure 2.8). This generated a gradient of 7-8 K across the sample.

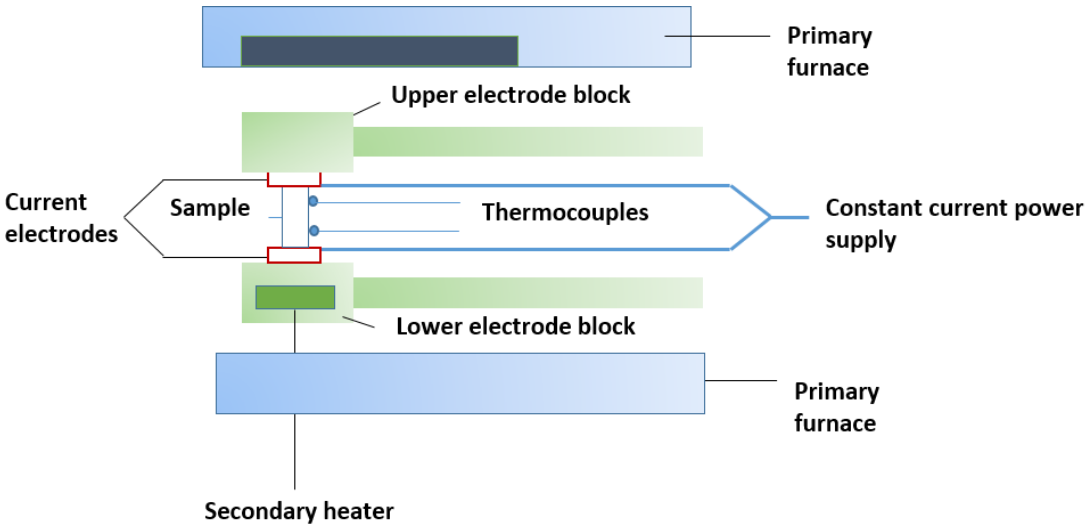

Figure 2.8. Schematic representation of the Linseis LSR-3 instrument.

2.4.3 Thermal Conductivity

A Linseis LFA 1000 laser flash instrument was used to measure the thermal diffusivity of several $(TiCoSb)_{1-x}(TiM_2Sn)_x$ nanocomposites (M = Fe, Ni). This instrument uses the flash method to measure the thermal diffusivity and heat capacity (by comparison to a reference sample) of a sample over a wide range of temperatures. The obtained values can be then used to determine κ. For these measurements, samples were prepared in the shape of cylindrical disks with a diameter of 13 mm. A layer of graphite was coated on both sides of the disk to maximise the absorption of the incident energy.

The flash method involves irradiating one surface of the sample with an intense energy pulse. This surface absorbs the incident energy and results in a temperature rise at the rear surface of the sample, which is measured by an IR detector. The thermal diffusivity

is then determined from the length of time, $t_{1/2}$, required for the rear surface to reach 50% of the maximum temperature rise as described in Equation (2.22). [108]

$$\alpha = \frac{1.38d^2}{t_{1/2}} \qquad \text{Equation (2.22)}$$

Where α is the thermal diffusivity ($m^2\ S^{-1}$) and d is the thickness of the disk (m).

The other quantity needed for generating κ data is the heat capacity C_p. Practically, there is no direct means to measure the amount of energy absorbed by the sample using the LFA instrument. Thus the heat capacity can only be obtained by a comparative method in which the flash experiment is carried out alternatively on a reference sample with previously determined properties, and the sample under investigation. Assuming that the sample and the reference have the same diameter, the heat capacity can be then calculated as shown in Equation (2.23). [109]

$$C_p = C_{p,ref}.\frac{T_{max,ref}}{T_{max}}\frac{\rho_{ref}d_{ref}}{\rho d} \qquad \text{Equation (2.23)}$$

Where ρ_{ref} and d_{ref} are the density and thickness of the reference sample, respectively. ρ is the density of the sample being investigated.

From thermal diffusivity and heat capacity values, κ can be calculated using Equation (2.24).

$$\kappa = \alpha\rho C_p \qquad \text{Equation (2.24)}$$

Where κ represents the thermal conductivity measured in $Wm^{-1}K^{-1}$.

In addition, 3 compositions of the $Ti_{1-x}V_xCo_{1-y}Fe_ySb_{1-z}Sn_z$ series were measured at the Institute for condensed Matter Chemistry Bordeaux, France by Dr. Michael Pollet, using a Netzch LFA 457 laser flash instrument.

2.4.3.1 Callaway Model

As discussed in Chapter 1, κ_{lat} can be reduced via different phonon scattering mechanisms. These include phonon-phonon, phonon-interfaces and phonon-defects scattering mechanism. Callaway model can be used in order to investigate the mechanism being responsible for the reduction of κ_{lat}. In this thesis, $\kappa_{lat}(T)$ data of two compositions (Chapter 4) were fitted using Callaway model, which can be described by Equation (2.25).

$$\kappa_{lat} = \frac{k_B}{2\pi^2 v_s}\left(\frac{k_B T}{\hbar}\right)^3 \int_0^{\frac{\theta_D}{T}} \frac{x^4 e^x}{\tau_{ph}^{-1}(e^x - 1)^2}\, dx \qquad \text{Equation (2.25)}$$

Here, v_s is the velocity of sound, θ_D is the Debye temperature, x the reduced energy and $\tau_{ph}^{-1} = v_s/L + A\omega^4 + B\omega^2 T e^{-\theta D/3T}$ is the phonon relaxation due to boundary, point-defect (PD) and Umklapp scattering, respectively.

Chapter 3–Thermoelectric Properties and High Temperature Stability of the $Ti_{1-x}V_xCoSb_{1-x}Sn_x$ Half Heusler Alloys

3.1 Introduction

This work investigates the structure and properties of the $Ti_{1-x}V_xCoSb_{1-x}Sn_x$ solid solution, which connects the 18 electron HH compounds: TiCoSb and VCoSn. The latter has been subjected to theoretical investigation [110,111] but has not been convincingly isolated. [112] Here it is unclear from the literature if TiCoSb is prone to spontaneous phase segregation into HH and FH phases. The absence of a FH $TiCo_2Sb$ phase in structural database suggests that this route for phase segregation may not be available. In addition, the reported thermoelectric data on TiCoSb are similar in many instances, [71,113,114] suggesting that this composition is indeed less susceptible to non-stoichiometry. Another unresolved issue is the high-temperature stability of TiCoSb-based HHs. Typically these phases show poorer thermal stability than TiNiSn-based compounds. [115] A variable temperature synchrotron X-ray diffraction study of TiCoSb revealed the onset of sample degradation above 700 K, and the formation of metallic CoSb impurity phases. [116] No other impurity phases were observed in diffraction and it remains unclear what happens to Ti during sample decomposition. On the other hand, TiCoSb based samples show excellent cycling stability in vacuum with no discernible degradation of the thermoelectric properties even after 100s of temperature cycles. [117] In this work, samples were structurally investigated using X-ray powder diffraction. In addition, neutron powder diffraction and scanning electron microscopy (SEM) were used to determine the experimental compositions of the $Ti_{1-x}V_xCoSb_{1-x}Sn_x$ HH alloys.

3.2 Synthesis

A preliminary series of polycrystalline $Ti_{1-x}V_xCoSb_{1-x}Sn_x$ samples (x = 0, 0.125, 0.25, 0.375, 0.5, 0.75 and 1) was synthesised on a 1 gram scale via conventional solid-state reactions, as described in Chapter 2. The samples were heated in evacuated sealed quartz tubes at 850 °C for 5 days with one intermediate homogenisation after 24 hours. Three 3 gram samples of TiCoSb and two 3 gram samples of $Ti_{0.7}V_{0.3}CoSb_{0.7}Sn_{0.3}$ were prepared in an identical manner and subsequently hot-pressed at 850 °C for 20 minutes. The densities of the hot-pressed samples were determined using the Archimedes method and were > 95% of the theoretical density. By contrast, the densities for the cold-pressed preliminary series were between 70 and 75% (Table 1, Appendix 1). Neutron powder diffraction data were collected on powdered hot-pressed pieces of TiCoSb and

$Ti_{0.7}V_{0.3}CoSb_{0.7}Sn_{0.3}$ using the Polaris instrument. The microstructure and chemical composition of the hot-pressed TiCoSb and $Ti_{0.7}V_{0.3}CoSb_{0.7}Sn_{0.3}$ samples were analysed using scanning electron microscopy. The working distance, spot size and collecting time were 10 mm, 4.5 and 4-10 frames, respectively.

3.3 X-ray Powder Diffraction

3.3.1 Formation of the $Ti_{1-x}V_xCoSb_{1-x}Sn_x$ Series

The X-ray powder diffraction patterns for the preliminary $Ti_{1-x}V_xCoSb_{1-x}Sn_x$ series are shown in Figure 3.1. For $0 \leq x \leq 0.5$ the major reflections are matched with those for a cubic HH phase. For x = 0.625, 0.75, the patterns contained a mix of HH, full-Heusler (FH) and unidentified impurity peaks. For x = 1, the main peaks were indexed to a FH structure while a minor $CoSn_2$ phase was also unambiguously identified. It proved impossible to index the remaining reflections on any of the phases contained within the ICSD database. Significantly, the x = 1 sample was clearly free of any HH phase. A lattice parameter of 5.8830(1) Å was obtained for TiCoSb, which is in good agreement with a = 5.8835(1) Å reported in a synchrotron diffraction study. [116] The composition dependence of the HH and FH lattice parameters are shown in Figure 3.2. The HH lattice parameter shows a linear decrease to x = 0.43, beyond which no further change is observed. This suggests the formation of a solid solution with an upper limit near x = 0.43. The decrease in lattice parameter is consistent with the replacement of Ti (1.40 Å) by V (1.35 Å), while Sn and Sb have similar radii (1.45 Å). [118] The FH lattice parameter has a minimum near x = 0.65 and falls between 5.9981(7) Å and 6.0129(2) Å. This illustrates that the FH composition varies but this is not clearly correlated with the nominal composition (x). The reported lattice parameters for VCo_2Sn in the ICSD database fall between 5.96-5.99 Å, which is significantly smaller than the values observed here. This suggests that VCo_2Sn is not a line-phase and that these samples are somewhat V or Sn rich.

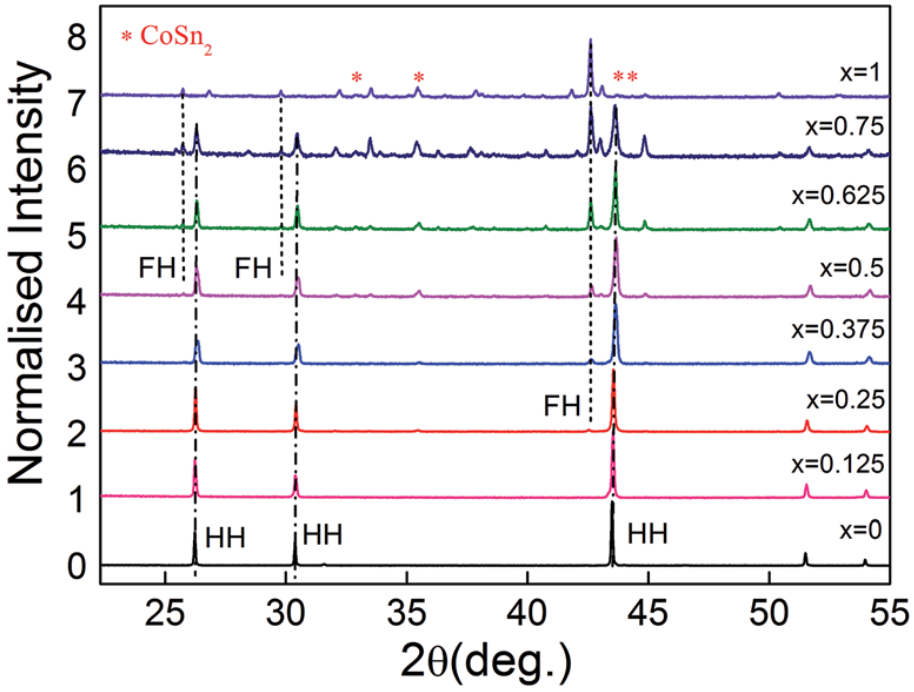

Figure 3.1. X-ray powder diffraction patterns for the $Ti_{1-x}V_xCoSb_{1-x}Sn_x$ series. Data have been normalised and offset by 1. The x = 0 sample is phase pure TiCoSb (HH), while the dominant peaks for x = 1 correspond to a full-Heusler (FH) phase (VCo_2Sn). The unindexed reflections for $x \geq 0.5$ do not correspond to any known phases contained within the ICSD database.

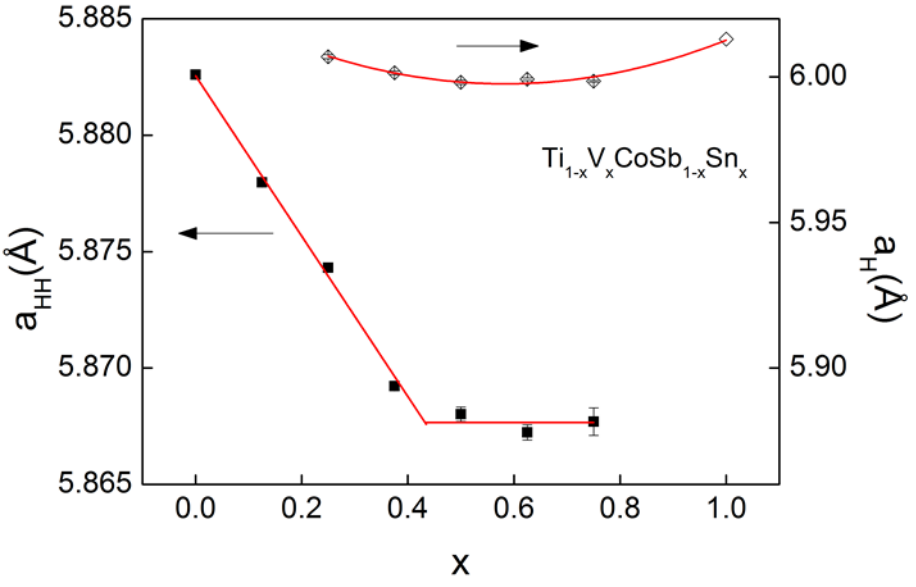

Figure 3.2. Composition dependence of the half-Heusler (a_{HH}) and full-Heusler (a_{FH}) lattice parameters for the $Ti_{1-x}V_xCoSb_{1-x}Sn_x$ series.

3.3.2 Structure of hot-pressed TiCoSb and $Ti_{1-x}V_xCoSb_{1-x}Sn_x$

The lattice parameters and density of all hot-pressed samples are summarised in Table 3.1, and representative X-ray diffraction patterns collected are shown in Figure 3.3. The TiCoSb samples do not contain impurities, while a trace amount of FH was detected in the $Ti_{0.7}V_{0.3}CoSb_{0.7}Sn_{0.3}$ sample. Careful inspection of the X-ray patterns revealed a clear shoulder to the HH reflections for the x = 0.3 sample, and a broadened base for TiCoSb. This is illustrated by the close-up of the (420) reflection shown in the insets to Figure 3.3.

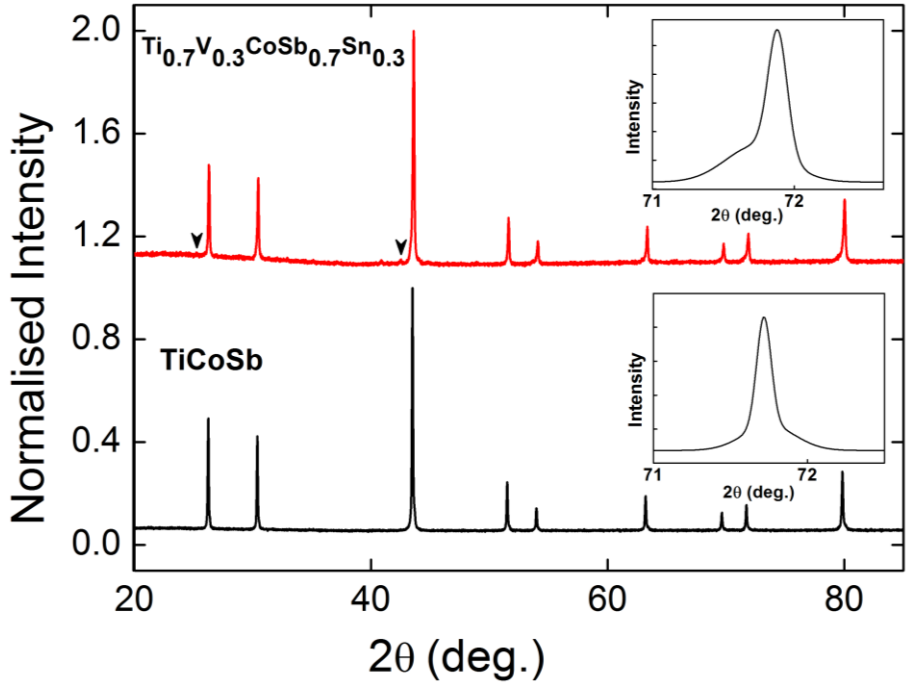

Figure 3.3. X-ray powder diffraction patterns for TiCoSb and $Ti_{0.7}V_{0.3}CoSb_{0.7}Sn_{0.3}$. The insets illustrate the broadening of the half-Heusler reflections (data have been normalised and offset by 1; ▼: VCo_2Sn).

Table 3.1. Overview of the lattice parameters (a), room temperature Seebeck coefficient (S), electrical resistivity (ρ), percentage density and estimated bandgap (E_g, see text) for the hot-pressed repeat samples of TiCoSb and $Ti_{0.7}V_{0.3}CoSb_{0.7}Sn_{0.3}$.

Composition	Sample	a (Å)	S (μV K^{-1})	ρ (mΩ cm)	Density (%)	E_g (eV)
TiCoSb	A	5.8830(1)	-305	25.5	95	0.46
	B	5.8829(1)	-298	23.7	97	0.40
	C	5.8831(1)	-251	16.2	98	0.48
$Ti_{0.7}V_{0.3}CoSb_{0.7}Sn_{0.3}$	A	5.8737(1)	-85	2.7	100	-
	B	5.8714(1)	-95	2.9	97	-

3.4 Neutron Powder Diffraction

Neutron powder diffraction was used to investigate the distribution of the metals over the available crystallographic sites. Neutrons are suited to this because of the good neutron scattering contrast between the elements present: Ti (-3.44 fm), V (-0.38 fm), Co (2.49 fm), Sb (5.57 fm), Sn (6.22 fm) and Ta (6.91 fm). The refined atomic parameters and fit statistics for the three investigated TiCoSb and one x = 0.3 composition are listed in Table 3.2, and the fit quality is illustrated in Figure 3.4. For TiCoSb, initial fits revealed an improvement in χ^2 by increasing the average scattering strength on the Ti site. The incorporation of Ta within the HH structure was evident from SEM-EDX analysis (Section 3.6). Thus, substitution of 2-3% Ta for Ti led to significantly improved χ^2 values (typical $\Delta\chi^2$ = 0.2-0.3). Allowing for the partial occupancy of the vacant tetrahedral (Y2) site that becomes filled in case of a phase segregation into HH and nano-FH phases [91] did not further improve χ^2, and led to zero site occupancies (Table 3.2). This suggests that TiCoSb does not have the tendency to spontaneously form nanosegregated $TiCo_2Sb$ regions, as observed in the Ni-based half-Heuslers [91,119]. However, it is difficult to obtain unambiguous site occupancy information in these high-symmetry systems, and identical χ^2 values are possible for 10% Co occupancy of the Y2 site in the absence of Ta on the Ti site. The SEM-EDX data (section 3. 6) point towards the presence of Ta within the HH structure and the best interpretation of the available data is therefore that there is no spontaneous segregation into HH and nano-FH phases. Inspection of the data for the x = 0.3 sample revealed the presence of shoulders to most but not all of the HH reflections. These were indexed using a FH phase with a = 5.9195(4) Å and a refined composition of $Co_{0.81(2)}Ti_{0.19(2)}(Co_{0.91(1)}Ti_{0.09(1)})_2Sb$ and an abundance of 9.1(1) wt%. Refinement of the

site occupancies of the main HH phase, yielded a $Ti_{0.7(1)}V_{0.27(1)}Ta_{0.025}CoSb_{0.7}Sn_{0.3}$ composition, where the Sb and Sn ratio was kept fixed due to the small difference in neutron scattering length, and a similar amount of Ta substitution as in TiCoSb was assumed (Table 3.2). This confirms the successful double substitution of V and Sn in TiCoSb, which is also evident from the SEM-EDX analysis below. A second smaller 2.5(1) wt% FH VCo_2Sn phase with a larger lattice parameter, a = 6.0281(6) Å was also observed.

Table 3.2. Structural parameters and fit statistics for TiCoSb (samples A-C) and $Ti_{0.7}V_{0.3}CoSb_{0.7}Sn_{0.3}$ (sample A) obtained from Rietveld fits against Polaris neutron powder diffraction data.

		TiCoSb (A)	TiCoSb (B)	TiCoSb (C)	$Ti_{0.7}V_{0.3}CoSb_{0.7}Sn_{0.3}$ (A)
a (Å)		5.8858(1)	5.8819(1)	5.8830(1)	5.8737(1)
X	U_{iso} (Å^2)	0.0039(1)	0.0040(1)	0.0039(1)	0.0047(1)
	Occ	$Ti_{0.98(1)}Ta_{0.02(1)}$	$Ti_{0.98(1)}Ta_{0.02(1)}$	$Ti_{0.97(1)}Ta_{0.03(1)}$	$Ti_{0.70(1)}V_{0.27(1)}Ta_{0.025}$
Y1	U_{iso} (Å^2)	0.0039(1)	0.0040(1)	0.0039(1)	0.0077(1)
	Occ	Co	Co	Co	Co
Y2	U_{iso} (Å^2)	0.0039(1)	0.0040(1)	0.0039(1)	-
	Occ	$Co_{0.001(4)}$	$Co_{0.002(3)}$	$Co_{0.001(3)}$	-
Z	U_{iso} (Å^2)	0.0039(1)	0.0040(1)	0.0039(1)	0.0039(1)
	Occ	Sb	Sb	Sb	$Sb_{0.7}Sn_{0.3}$
χ^2		1.3	1.9	1.4	2.0
Bank5	wR_p (%)	2.1	2.6	1.5	2.5
	R_p (%)	3.7	3.6	2.5	4.0
Bank4	wR_p (%)	1.8	1.7	1.6	1.7
	R_p (%)	3.7	4.0	3.5	2.8
Bank3	wR_p (%)	2.0	2.4	1.9	3.2
	R_p (%)	6.8	3.0	2.5	7.4

The $Ti_{0.7}V_{0.3}CoSb_{0.7}Sn_{0.3}$ sample contained 9.1(1) wt% of a full-Heusler phase with refined composition $Co_{0.81(2)}Ti_{0.19(2)}(Co_{0.91(1)}Ti_{0.09(1)})_2Sb$ (a = 5.9195(4) Å) and 2.5(1) wt% of VCo_2Sn (a = 6.0281(6) Å). HH phases; X: 4a (0, 0, 0); Y1: 4c (¼, ¼, ¼); Y2: 4d (¾, ¾, ¾); Z 4b (½, ½, ½).

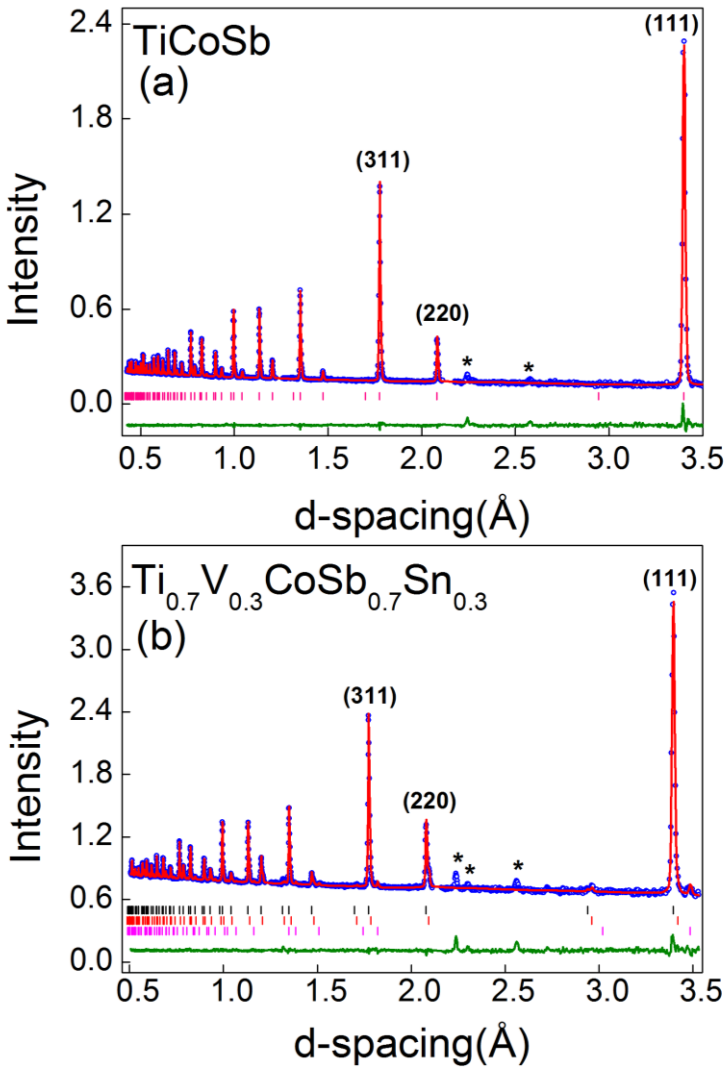

Figure 3.4. Rietveld fit to Polaris neutron powder diffraction data for TiCoSb and $Ti_{0.7}V_{0.3}CoSb_{0.7}Sn_{0.3}$. In (a) the reflection markers are for TiCoSb. In (b) the top, middle and bottom markers are for $Ti_{0.7}V_{0.3}CoSb_{0.7}Sn_{0.3}$, $Co_{0.81(2)}Ti_{0.19(2)}(Co_{0.91(1)}Ti_{0.09(1)})_2Sb$ and VCo_2Sn. An unindexed impurity phase labelled by asterisks is observed in both samples. Data shown are from detector bank 4.

3.5 SEM–EDX Analysis

To further investigate the sample homogeneity SEM-EDX analysis was performed on the hot-pressed samples. The results are summarised in Figure 3.5. The surfaces contain some small voids after polishing, and are characterised by average grain sizes <5 μm. No obvious segregation of any elements was observed but clear variations in brightness are evident in the BSE images. In particular, the boundaries of the grains appear brighter, consistent with a higher average atomic number. Elemental analysis revealed that the variations in brightness are due to the presence of Ta which was used as the sample containment material. The compositions of the mapped areas in the TiCoSb sample are TiCoSb (I) and $Ti_{0.95}Ta_{0.05}CoSb$ (II), respectively. Three regions with varying Ta-concentration were observed in the x = 0.3 sample. These are $Ti_{0.81}V_{0.19}CoSb_{0.83}Sn_{0.17}$ (I), $Ti_{0.66}Ta_{0.1}V_{0.24}CoSb_{0.77}Sn_{0.22}$ (II) and $Ti_{0.64}Ta_{0.14}V_{0.22}CoSb_{0.77}Sn_{0.23}$ (III). In both cases, the core of the grains does not contain Ta, while the boundaries contain up to 10-15%. The inhomogeneous distribution suggests that the HH reacts slowly to the Ta foil after forming from the elemental precursors.

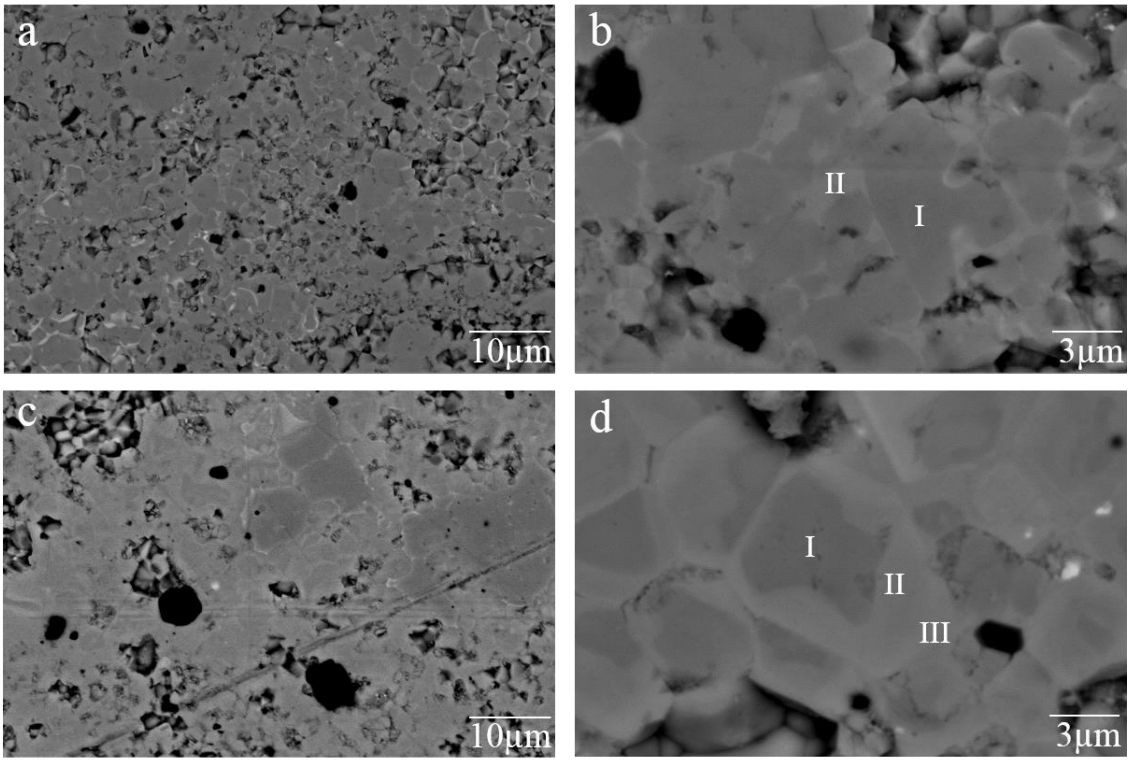

Figure 3.5. BSE-SEM images for TiCoSb (a, b) and $Ti_{0.7}V_{0.3}CoSb_{0.7}Sn_{0.3}$ (c, d). These images reveal relatively small grains and evidence for compositional variations along grain boundaries. For TiCoSb, the compositions of regions I and II are TiCoSb and $Ti_{0.95}Ta_{0.05}CoSb$. The compositions for $Ti_{0.7}V_{0.3}CoSb_{0.7}Sn_{0.3}$ are I: $Ti_{0.81}V_{0.19}CoSb_{0.83}Sn_{0.17,}$ II: $Ti_{0.66}Ta_{0.1}V_{0.24}CoSb_{0.77}Sn_{0.22}$ and III: $Ti_{0.64}Ta_{0.14}V_{0.22}CoSb_{0.77}Sn_{0.23.}$

3.6 Thermoelectric Properties

3.6.1 Thermoelectric power factor of TiCoSb

The temperature dependence of ρ, S and S^2/ρ for the hot-pressed TiCoSb samples (A, B, and C) are shown in Figure 3.6. These samples were prepared under identical conditions and similar thermoelectric properties are observed. The $\rho(T)$ curves show a metal-like temperature dependence with $\rho_{300\ K}$ = 16-25 mΩ cm and $\rho_{723\ K}$ = 23-32 mΩ cm (Figure 3.6a). The observation of degenerate rather than conventional semiconducting behaviour is consistent with n-type doping due to the incorporation of Ta. The S(T) is found to increase linearly from $S_{300\ K}$ = -250-300 μV K^{-1} to maximum values -330-370 μV K^{-1} at 600-700 K (Figure 3.6b). The thermal bandgap was estimated using $E_g = 2|S_{max}|T_{max}$, yielding values of 0.48 eV (A), 0.40 eV (B) and 0.46 eV (C). [21] The samples attained similar maximum power factors S^2/ρ = 0.47 mW m^{-1} K^{-2} at 500 K (A), and 0.55 mW m^{-1} K^{-2} at 550 K (B and C, Figure 3.6c). Zhou et al have reported $\rho_{300\ K}$ = 20 mΩ

cm, $S_{300\ K}$ = -210 μV K^{-1} and $(S^2/\rho)_{max}$ = 0.7 mW m^{-1} K^{-2} for 1% Ta substitution in TiCoSb. [75] These values are similar to our data and suggest that our samples contain ~1% Ta, which is in keeping with the compositions obtained from neutron powder diffraction.

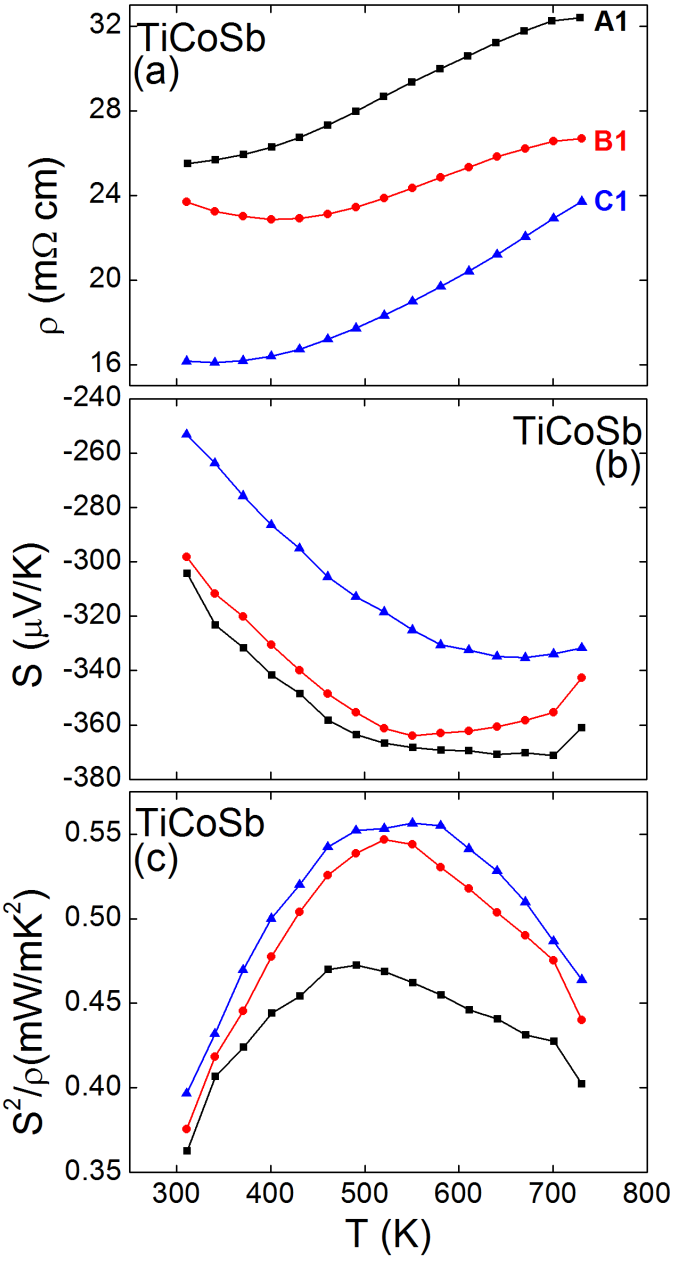

Figure 3.6. Temperature dependence of the electrical resistivity (ρ), Seebeck coefficient (S), and thermoelectric power factor (S^2/ρ) for the three hot-pressed TiCoSb samples (first measurement).

3.7 Temperature stability of TiCoSb and $Ti_{0.7}V_{0.3}CoSb_{0.7}Sn_{0.3}$

To test the thermal stability of the materials, S and ρ measurements were performed on the hot-pressed samples under He atmosphere several times, first up to a maximum temperature of 723 K and then up to 823 K for TiCoSb and 923 K for $Ti_{0.7}V_{0.3}CoSb_{0.7}Sn_{0.3}$. The results of these repeat measurements are shown in Figure 3.7. The $\rho(T)$ for TiCoSb shows a gradual decrease in magnitude for the measurements to 723 K (runs B1-4, Figure 3.7a). A sudden drop is observed at 723 K for run B5 that extends to 823 K and further reductions in magnitude are observed for run B6 (also up to 823 K, Figure 3.7a). The $S(T)$ shows a gradual reduction in magnitude (Figure 3.7b), and S^2/ρ is improved due to the decrease in ρ (Figure 3.7c). Post measurement X-ray powder diffraction (Figure 1, Appendix 1) revealed the presence of a 1-2 wt% metallic CoSb impurity. An identical experiment on a cold-pressed TiCoSb sample (~70% dense) from the preliminary series resulted in ~ 10 wt% CoSb after 6 repeats (Figure 2, Appendix 1). The lattice parameter of TiCoSb remained almost unchanged, suggesting that its composition does not change. The hot-pressed x = 0.3 sample does not show the same dramatic changes in thermoelectric transport upon cycling. An initial drop in ρ is observed between run 1 and 2 but after that identical ρ(T) are observed (Figure 3.7d). Similarly, the $S(T)$ below 600 K for runs 2-4 are identical within the experimental error. Above 650 K some discrepancies are observed, for example run A2 and A4 have S-shaped anomalies near 800 K, while run A3 is much smoother. The cause of the S-shaped response at high temperature is not clear but suggests that the sample is out of equilibrium. The relatively low ρ and high S values lead to power factors S^2/ρ = 0.8 mW m^{-1} K^{-2} at 900 K for the first measurement, and improving up to 1.2 mW m^{-1} K^{-2} for run 3 and 4 (Figure 3.7f). Post measurement X-ray diffraction did not reveal the emergence of any clear impurities (Figure 1, Appendix 1). By contrast, the cold-pressed x = 0.375 sample shows evidence for degradation with the emergence of substantial CoSb and $CoSn_2$ impurity phases, and increased amounts of VCo_2Sn. Interestingly, the thermoelectric properties of this sample hold up much better compared to TiCoSb.

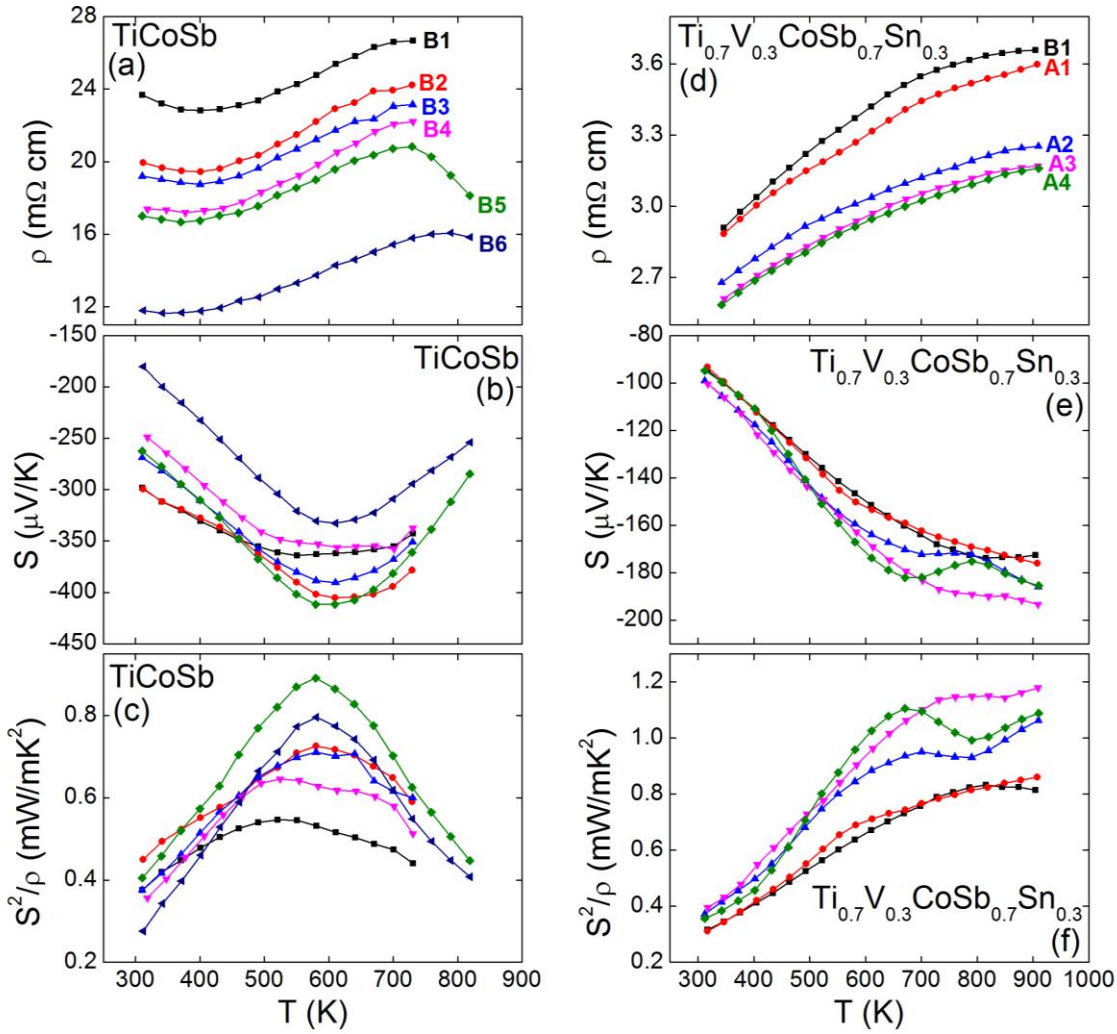

Figure 3.7. Repeatability testing of the electrical resistivity (ρ), Seebeck coefficient (S), and thermoelectric power factor (S^2/ρ) of TiCoSb (sample B, repeats 1-6) and $Ti_{0.625}V_{0.375}CoSb_{0.625}Sn_{0.375}$ (sample A, repeats 1-4; sample B, first measurement).

To further investigate the degradation we undertook SEM-EDX analysis on a polished piece of the TiCoSb sample used for the repeated cycling (data in Figure 3.7). Secondary electron (SE), BSE images and elemental maps for a representative area are shown in Figure 3.8. Two distinct regions are evident in these images: on the left there is a large smooth area with EDX composition close to TiCoSb and towards the right contrast variations are evident. The elemental maps show the presence of substantial quantities of oxygen at the right part of the image, while the left side is nearly free of oxygen. The SE image reveals that the inhomogeneous area on the right is relatively smooth and confirms that the BSE contrast variations are due to compositional variations. EDX analysis yields compositions consistent with TiO_2 and CoSb. The microscopy therefore demonstrates that TiCoSb decomposes into TiO_2 and CoSb. The morphology of the oxidised areas and the absence of TiO_2 in the X-ray powder diffraction data demonstrates that this is an amorphous phase.

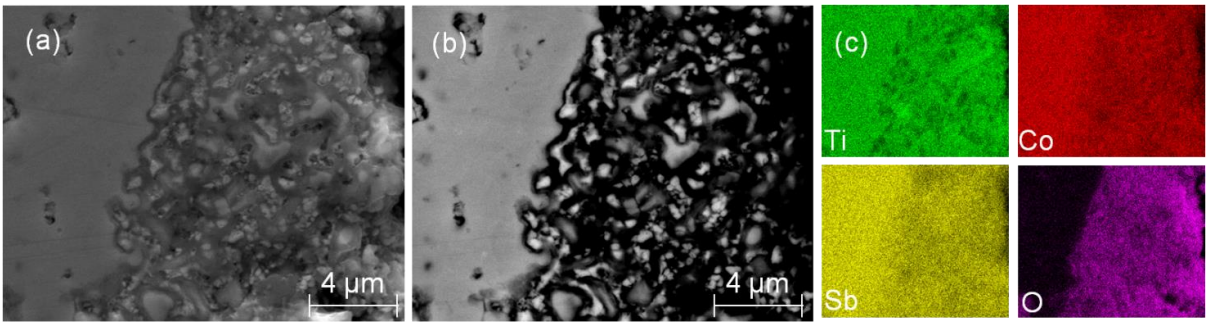

Figure 3.8. (a) SE, (b) BSE scanning electron microscopy images and (c) elemental maps for the hot-pressed TiCoSb sample after repeated measurement of the thermoelectric properties (data in Figure 3.7).

3.8 Discussion

An upper solubility limit near x = 0.4 was established for the $Ti_{1-x}V_xCoSb_{1-x}Sn_x$ solid solution, demonstrating that VCoSn cannot be prepared. This experimental observation is in agreement with a recent computational study that predicted that VCoSn is unstable due to the formation of competing phases, [120] which is in keeping with our diffraction results, although we could not unambiguously index all phases present (Figure 3.1). Analysis of the experimental compositions of the $Ti_{1-x}V_xCoSb_{1-x}Sn_x$ solid solution using NPD and SEM-EDX demonstrates that TiCoSb is stoichiometric, except for the incorporation of Ta along the grain edges due to reaction to the sample containment material. TiCoSb therefore does not appear to be as susceptible to non-stoichiometry as TiNiSn. [91] This may be related to the absence of a $TiCo_2Sb$ FH phase or the absence of other competing phases, such as Ti_5Sn_3, calculated for TiNiSn. [121] The thermoelectric properties for the repeat TiCoSb (samples A–C) and x = 0.3 samples (sample A and B) are similar (Figure 3.6 and Figure 3.7) showing that the synthesis protocol leads to reproducible results. Maximum power factors S^2/ρ = 0.5 $mWm^{-1}K^{-1}$ (x = 0) and S^2/ρ = 0.8 mWm^{-1} K^{-2} (x = 0.3) are observed. Both TiCoSb and $Ti_{1-x}V_xCoSb_{1-x}Sn_x$ show degradation after repeated measurements of their thermoelectric properties in a He atmosphere. The observed changes are more pronounced for TiCoSb than for the V and Sn substituted samples. However, post measurement analysis reveals the formation of significant amounts of CoSb (and $CoSn_2$) in all cases, in particular for the porous cold pressed samples. This immediately suggests a link to the presence of trace amounts of atmospheric oxygen. The SEM and elemental analysis confirm the presence of amorphous TiO_2. A back of the envelope calculation suggests that ~ 2% of TiCoSb can be converted to TiO_2 and CoSb in each measurement before depleting the oxygen present in the measurement chamber. The observation of ~ 10 wt% CoSb for the porous samples after 6 repeats is therefore feasible, and consistent with our experimental data. Further indirect support for the oxidation of Ti as the driving force for the degradation comes from the analogous XCoSb phases with Zr and Hf which have been measured up to 800–900 °C in a similar atmosphere without any reported degradation. [122] Excluding oxygen also leads to improved stabilities as evidenced by the recent report of 100s of heating cycles in vacuum without any degradation in properties. [117] The similar lattice parameters for the HH phases before and after cycling suggests that the composition of the HH phase itself does not change during measurement, and that the degradation in the thermoelectric properties is due to sample oxidation.

To summarise, TiCoSb forms as a stoichiometric phase and does not show the same tendency to spontaneously phase segregate into HH and nano-FH phases that is observed for TiNiSn. The $Ti_{1-x}V_xCoSb_{1-x}Sn_x$ HH alloys can be prepared up to x = 0.4 and are reactive towards oxygen at moderate temperatures with the formation of amorphous TiO_2 and crystalline CoSb and $CoSn_2$ phases evident from post measurement analysis. This demonstrates that thermoelectric generators based on these HH phases will need to be carefully encapsulated.

Chapter 4–Unexpected N-type Conduction in Half Heusler Thermoelectric Materials

4.1 Introduction

This study is focussed on TiCoSb based HH thermoelectrics with substitution at all three atomic positions. This builds on the work presented in Chapter 3 that found that co-substitution of V and Sn improves the high-temperature stability of these compounds. The initial aim of this work was to p-type dope these materials by substitution of Fe on the Co site. This has been previously used to achieve a promising ZT = 0.45 in $TiCo_{1-x}Fe_xSb$ HHs without co-substitution on the X and Z sites. [74] A number of $Ti_{1-x}V_xCo_{1-y}Fe_ySb_{1-z}Sn_z$ compositions were prepared, where x, y and z were adjusted to achieve VEC = 17.85. Surprisingly, electrical property measurements reveal unexpected n-type behaviour for both $Ti_{0.7}V_{0.3}Co_{0.85}Fe_{0.15}Sb_{0.7}Sn_{0.3}$ and $Ti_{0.7}V_{0.3}Co_{0.75}Fe_{0.25}Sb_{0.8}Sn_{0.2}$, while p-type behaviour was observed for $Ti_{0.7}V_{0.3}Co_{0.55}Fe_{0.45}Sb$. Typically, this behaviour has been linked to phase segregation driven by deviations from the highly stable 18 VEC HH structure. As discussed in Chapter 1, Section 1.7.3.2, another multiphase effect is the poor mixing of the X metals that occurs at low temperatures. A recent computational work has shown that atomic substitution in TiCoSb carry an enthalpy that can be overcome by entropy of mixing at high temperature. This study covered V-Fe substitution on the Ti site and in all cases, the calculated phase diagrams showed a lack of solubility at low temperatures. [80] Therefore, the work presented in this chapter will offer the opportunity to investigate this potential phase segregation in TiCoSb, with substitutions at the three atomic positions. Samples were analysed by X-ray and neutron powder diffraction. SEM-EDX analysis was also performed to check compositional homogeneity and microstructure of some of the investigated samples.

4.2 Synthesis

Samples with compositions of $Ti_{1-x}V_xCo_{1-y}Fe_ySb_{1-z}Sn_z$ (x = 0, 0.3), (y = 0, 0.15, 0.25, 0.45), (z = 0, 0.2, 0.3) were prepared on a 2.5 gram scale by conventional solid state route (Chapter 2). For all compositions, a 15% hole concentration was maintained by appropriate adjusting of the x, y and z values. Samples were annealed under vacuum in quartz tubes at 850 °C for an initial 24 hours period. Samples were then reground, pressed and annealed for an additional 7 days. Subsequent consolidation step through hot pressing was performed at 850 °C for 20 minutes under 80 MPa. To check

reproducibility, three samples with substitution at the three sites ($Ti_{0.7}V_{0.3}Co_{0.85}Fe_{0.15}Sb_{0.7}Sn_{0.3}$, $Ti_{0.7}V_{0.3}Co_{0.75}Fe_{0.25}Sb_{0.8}Sn_{0.2}$, $Ti_{0.7}V_{0.3}Co_{0.55}Fe_{0.45}Sb$) were prepared in an identical manner. Neutron powder diffraction data were collected at room temperature on ~ 1.5 g of finely ground samples. The microstructure and homogeneity of the samples were examined directly after hot pressing.

4.3 X-ray Powder Diffraction Analysis

Representative X-ray powder diffraction patterns of all compositions are shown in Figure 4.1. From this figure it can be seen that the main peaks are matched with those for a HH phase. A second phase of VCo_2Sn was observed for $Ti_{0.7}V_{0.3}Co_{0.85}Fe_{0.15}Sb_{0.7}Sn_{0.3}$. Further minor impurity peaks were detected in some samples as shown in Figure 4.1. These impurity peaks were identified as Sn and FeSb by searching against the ICDD-PDF database.

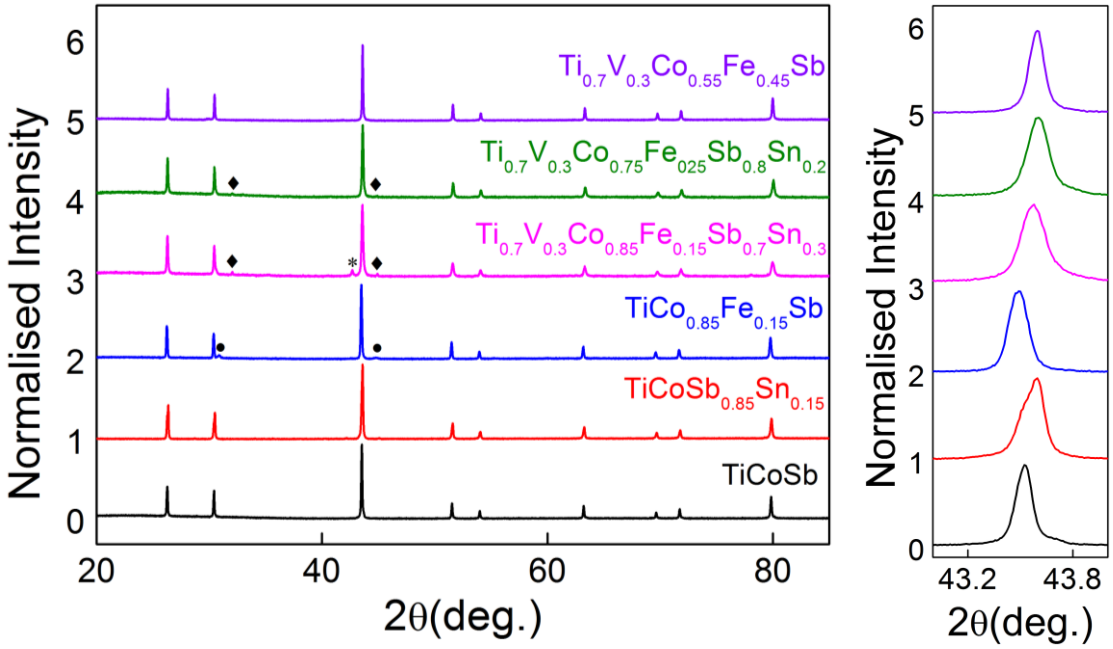

Figure 4.1. Representative X-ray Powder diffraction patterns for the $Ti_{1-x}V_xCo_{1-y}Fe_ySb_{1-z}Sn_z$ series. Data have been normalised and offset by 1. Where, *: FH, ♦: Sn and ●: FeSb phase, and a close up of the (220) reflection for each sample.

It is also apparent from the diffraction patterns that all peaks are sharp, except for $TiCoSb_{0.85}Sn_{0.15}$, which has shoulders on the low *2θ* side. Compared to the parent compound, TiCoSb, the peaks in $TiCo_{0.85}Fe_{0.15}Sb$ are shifted toward slightly lower scattering angles *2θ*, which is in agreement with larger atomic radius of Fe (1.40 Å) compared to Co (1.35 Å). Whereas, the reflections in the V, Fe and Sn doped samples are shifted to slightly higher 2θ angles, which is driven by the reduced size of V (1.35 Å) compared to Ti (1.40 Å), while Sn and Sb have similar radii (1.45 Å). [118] The lattice parameters of all synthesised samples obtained by Rietveld analysis are provided in Table 4.1. The lattice parameter values of $TiCoSb_{0.85}Sn_{0.15}$ (5.8855(1) Å) and $TiCo_{0.85}Fe_{0.15}Sb$ (5.8887(1) Å) agree well with a = 5.887 Å and a = 5.888 Å reported in the literature [74,123], respectively. As shown in Table 4.1, the three repeat samples $Ti_{0.7}V_{0.3}Co_{0.85}Fe_{0.15}Sb_{0.7}Sn_{0.3}$ (D1, D2), $Ti_{0.7}V_{0.3}Co_{0.75}Fe_{0.25}Sb_{0.8}Sn_{0.2}$ (E1, E2) and $Ti_{0.7}V_{0.3}Co_{0.55}Fe_{0.45}Sb$ (F1, F2) have very similar lattice parameters.

Table 4.1. Composition, sample code, lattice parameter (a), density, percentage density, resistivity (ρ), Seebeck coefficient (S) and thermal conductivity (κ) at 300 K and maximum power factor (S^2/ρ) for the investigated samples.

Composition	Sample	a (Å)	Density (g.cm^{-3})	%Density	ρ_{300k} (mΩ cm)	S_{300K} (μV K^{-1})	κ_{300K} (W m^{-1}K^{-1})	$(S^2/\rho)_{max}$ (mW m^{-1}K^{-2})
TiCoSb	A	5.8830(1)	7.1	95	25.5	-305	-	0.36
$TiCoSb_{0.85}Sn_{0.15}$	B	5.8855(1)	5.9	79	44.8	+116.9	-	0.10
$TiCo_{0.85}Fe_{0.15}Sb$	C	5.8887(1)	5.9	79	11.0	+80.9	-	0.52
$Ti_{0.7}V_{0.3}Co_{0.85}Fe_{0.15}Sb_{0.7}Sn_{0.3}$	D1	5.8724(1)	6.9	92	2.8	-60.1	-	0.38
	D2	5.8711(1)	7.1	95	4.1	-85.3	4.8	0.32
$Ti_{0.7}V_{0.3}Co_{0.75}Fe_{0.25}Sb_{0.8}Sn_{0.2}$	E1	5.8689(1)	7.5	100	2.8	-101.8	-	0.86
	E2	5.8690(1)	7.0	93	4.6	-84.2	-	0.37
$Ti_{0.7}V_{0.3}Co_{0.55}Fe_{0.45}Sb$	F1	5.8748(1)	6.75	90	3.8	+160.0	5.8	0.92
	F2	5.8776(1)	7.1	95	4.5	203.1	-	1.05

4.4 Neutron Powder Diffraction Analysis

Neutron powder diffraction was performed to determine the distribution of the metals over the available crystallographic sites, as any deviation from the nominal composition will have an impact on the TE properties. The neutron scattering length are b_{Ti} = -3.4 fm, b_{Ta} = 6.91 fm, b_V = -0.38 fm, b_{Co} = 2.49 fm, b_{Fe} = 9.45 fm, b_{Sb} = 5.57 fm, b_{Sn} = 6.2 fm and therefore allow a good contrast between the constituent elements. Data were collected on samples A, B, C, D1, E1 and F1 (see Table 4.1 for compositions). Rietveld fits to the Polaris neutron powder diffraction data for all samples are provided in Figure 4.2. Also, lattice parameters (a), weight percentages, thermal displacement parameters (U_{iso}/Å^2) and fractional occupancies for the HH, FH and other secondary phases that were used to fit the Polaris neutron powder diffraction data for these samples are given in Table 4.2.

4.4.1 $TiCoSb_{0.85}Sn_{0.15}$ (B)

For this composition, the first model was investigated by fixing the site occupancy of Ti and Co to their nominal values and refining the occupancy of Sb and Sn. This produced an unrealistic composition of $TiCoSb_{0.22(4)}Sn_{0.78(4)}$, with χ^2 = 1.67. However, as discussed in Chapter 3, small amounts of Ta can be incorporated into the HH structure. This was investigated by adding Ta on the Ti site (4b). The occupancy of Co, Sb and Sn were then fixed to their nominal values and a refinement of Ti and Ta occupancy yielded $Ti_{0.98(1)}Ta_{0.02(1)}$ on the 4b site, with χ^2 = 1.66. Keeping the occupancy of the Co and (Ti, Ta) positions fixed and refining the occupancy of Sb and Sn indicate a composition of $Ti_{0.98(1)}Ta_{0.02(1)}CoSb_{0.93(4)}Sn_{0.07(4)}$. This composition is in keeping with results obtained from SEM-EDX analysis, which revealed an average composition of $TiCoSb_{0.93}Sn_{0.07}$ (Figure 1, Appendix 2). Furthermore, small regions rich in Sn and Co were evident from the EDX-elemental mapping. Quantitative analysis indicated that the composition of these regions is close to $TiCo_{1.7}Sn$.

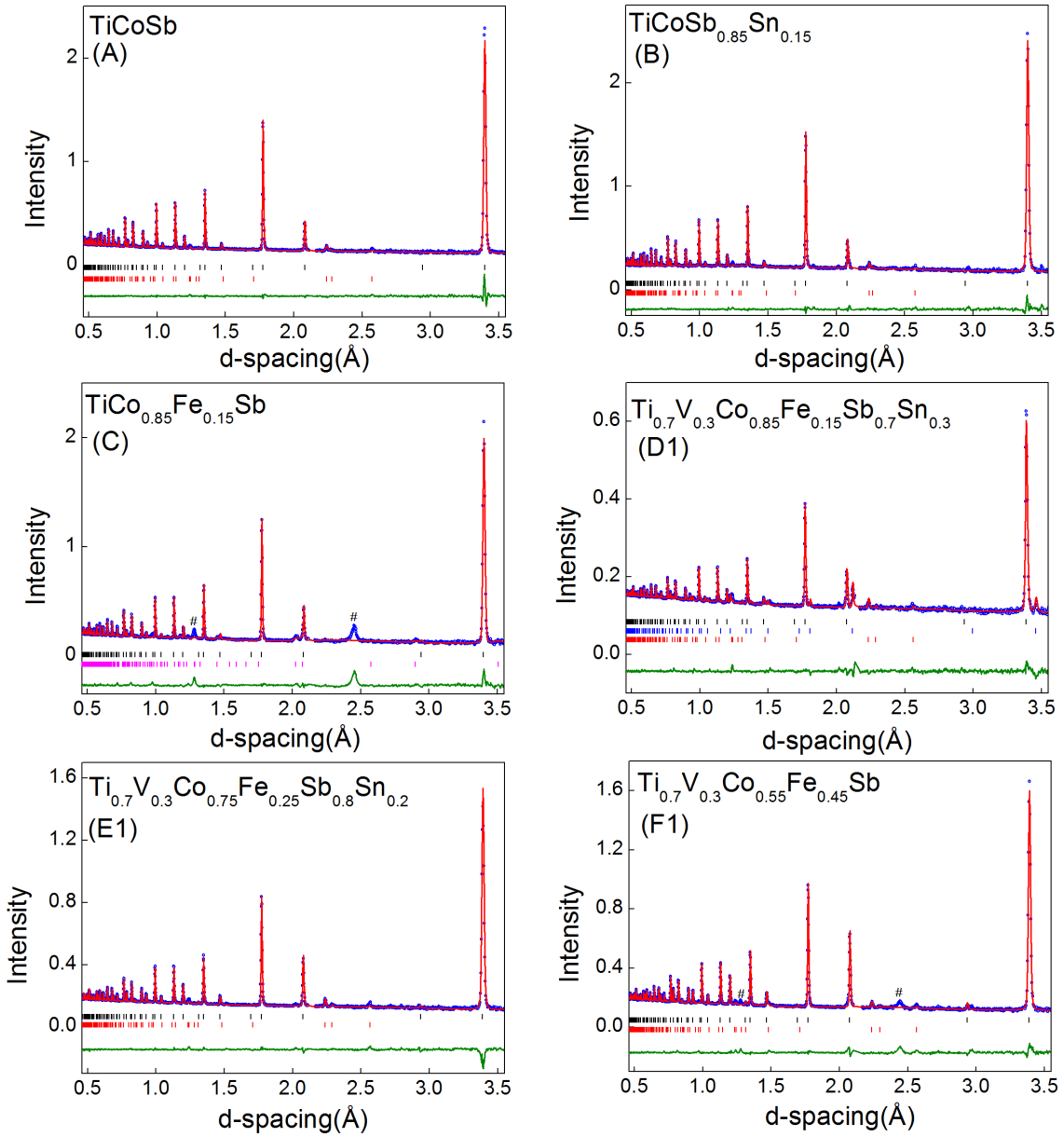

Figure 4.2. Rietveld fit to Polaris neutron powder diffraction data for TiCoSb (sample A), $TiCoSb_{0.8}Sn_{0.15}$ (sample B), $TiCo_{0.85}Fe_{0.15}Sb$, (sample C), $Ti_{0.7}V_{0.3}Co_{0.85}Fe_{0.15}Sb_{0.7}Sn_{0.3}$ (sample D1), $Ti_{0.7}V_{0.3}Co_{0.75}Fe_{0.25}Sb_{0.8}Sn_{0.2}$ (sample E1), and $Ti_{0.7}V_{0.3}Co_{0.55}Fe_{0.45}Sb$ (sample F1). Blue circles are the collected data, the red line is the calculated fit and the green line is the difference curve. Black markers are for the HH phases used to fit the data, blue marker are for the FH phase, red markers are for Ti and magenta markers are for FeSb. An unindexed impurity phase labelled by # is observed for $TiCo_{0.85}Fe_{0.15}Sb$ and $Ti_{0.7}V_{0.3}Co_{0.55}Fe_{0.45}Sb$. Data shown are from detector bank 4.

4.4.2 $TiCo_{0.85}Fe_{0.15}Sb$ (C)

The occupancies of the Ti and Sb positions were fixed to their nominal values. Refining the (Co, Fe) site occupancy produced a composition of $TiCo_{0.89(1)}Fe_{0.11(1)}Sb$, with χ^2 = 6.91. Trial fits with Ta on the Ti site led to unrealistic occupancies. The slightly reduced Fe content in the final refined composition is consistent with the presence of ~ 3 mol% of FeSb, which was also obvious from PXRD and previously reported as an impurity for this composition. [93] In addition to this, an unknown impurity phase with very broad peaks was detected in this sample. Excluding this unknown impurity from the pattern led to χ^2 = 2.56. SEM-EDX analysis revealed relatively homogenous distribution of the constituent elements, with an average composition of $TiCo_{0.88}Fe_{0.12}Sb$ (Figure 2, Appendix 2).

4.4.3 $Ti_{0.7}V_{0.3}Co_{0.85}Fe_{0.15}Sb_{0.7}Sn_{0.3}$ (D1)

In this sample, the distribution of the metals over the available sites was investigated by fixing Sb and Sn to their nominal values 0.7 and 0.3, respectively, as they have relatively similar scattering lengths. The subsequent refinement of the (Ti, V) and (Co, Fe) site occupancies produced a composition of $Ti_{0.78(1)}V_{0.22(1)}Co_{0.84(1)}Fe_{0.16(1)}Sb_{0.7}Sn_{0.3}$, with χ^2 = 2.22, which is close to the nominal composition. A trial fit with Sb and Sn site occupancy fixed to 0.9 and 0.1, respectively, obtained from SEM-EDX analysis, produced a composition of $Ti_{0.79(1)}V_{0.22(1)}Co_{0.84(1)}Fe_{0.16(1)}Sb_{0.9}Sn_{0.1}$, with χ^2 = 2.20. Clearly, in both cases the same X and Y site distribution was recovered with identical χ^2 value. This demonstrates that these fits are not sensitive to the Sb/Sn occupancy. This sample contained a considerable amount of FH (VCo_2Sn) ~ 14 wt%, which was also evident from PXRD (Figure 4.1) and SEM-EDX analysis (Figure 4.3).

4.4.4 $Ti_{0.7}V_{0.3}Co_{0.75}Fe_{0.25}Sb_{0.85}Sn_{0.2}$ (E1) and $Ti_{0.7}V_{0.3}Co_{0.55}Fe_{0.45}Sb$ (F1)

Investigation of the site occupancies in these samples was done in a similar manner to $Ti_{0.7}V_{0.3}Co_{0.85}Fe_{0.15}Sb_{0.85}Sn_{0.15}$. Sb and Sn were fixed to their nominal values. Refinement of the (Ti, V) and (Co, Fe) site occupancies indicated a composition of $Ti_{0.78(1)}V_{0.22(1)}Co_{0.76(1)}Fe_{0.24(1)}Sb_{0.8}Sn_{0.2}$, with χ^2 = 2.46 for sample E1, while a composition of $Ti_{0.69(1)}V_{0.31(1)}Co_{0.59(1)}Fe_{0.41(1)}Sb$, χ^2 = 3.83 was obtained for the F1 sample. Fit statistics for Rietveld refinement for all samples are given in Table 4.2.

Table 4.2. Lattice parameters (a), weight percentages, temperature displacement factors (U_{iso}/A) and fractional occupancies for the HH, FH and other impurity phases that were used to fit the Polaris neutron powder diffraction for samples A, B, C, D1, E1, F1

			TiCoSb (A)	$TiCoSb_{0.85}Sn_{0.15}$ (B)	$TiCo_{0.85}Fe_{0.15}Sb$ (C)	$Ti_{0.7}V_{0.3}C_{0.85}Fe_{0.15}Sb_{0.7}Sn_{0.3}$ (D1)	$Ti_{0.7}V_{0.3}C_{0.75}Fe_{0.25}Sb_{0.8}Sn_{0.2}$ (E1)	$Ti_{0.7}V_{0.3}C_{0.55}Fe_{0.45}Sb$ (F1)
Half Heusler Fm-43m	a (Å)		5.8830(1)	5.8855(1)	5.8883(1)	5.8671(1)	5.8721(1)	5.8685(1)
	Wt (%)		98.0(1)	97.0(1)	95.0(1)	80.0(1)	94.0(1)	96.7(1)
	4b	U_{iso} (Å^2)	0.0039(1)	0.0042(2)	0.0023(1)	0.0020(1)	0.0011(1)	0.0032(1)
		Occ	$Ti_{0.97(1)}Ta_{0.03(1)}$	$Ti_{0.98(1)}Ta_{0.02(1)}$	Ti	$Ti_{0.78(1)}V_{0.22(1)}$	$Ti_{0.78(1)}V_{0.22(1)}$	$Ti_{0.69(1)}V_{0.31(1)}$
	4c	U_{iso} (Å^2)	0.0039(1)	0.0052(8)	0.0069(9)	0.0094(1)	0.0031(1)	0.0075(1)
		Occ	Co	Co	$Co_{0.89(1)}Fe_{0.10(1)}$	$Co_{0.84(1)}Fe_{0.16(1)}$	$Co_{0.76(1)}Fe_{0.24(1)}$	$Co_{0.59(1)}Fe_{0.41(1)}$
	4a	U_{iso} (Å^2)	0.0039(1)	0.0036(1)	0.0048(2)	0.0043(1)	0.0051(1)	0.0035(1)
		Occ	Sb	$Sb_{0.93(4)}Sn_{0.07(4)}$	Sb	$Sb_{0.7}Sn_{0.3}$	$Sb_{0.8}Sn_{0.2}$	Sb
Ti P63/mmc	a (Å)		2.9705(2)	2.9759(2)	-	2.9561(5)	2.9620(2)	2.9595(4)
	c (Å)		4.5583(8)	4.5354(8)	-	4.5721(5)	4.5770(8)	4.5892(13)
	Wt (%)		2.0(1)	3.0(1)	-	5.4(2)	6.0(1)	3.3(1)
		U_{iso} (Å^2)	0.016(4)	0.007(1)	-	0.007(1)	0.005(1)	0.006(1)
Full Heusler Fm-3m	a (Å)		-	-		5.9900(2)	-	-
	Wt (%)		-	-		14.0(1)	-	-
	4b	U_{iso} (Å^2)	-	-		0.0139(6)	-	-
		Occ				V		
	8c	U_{iso} (Å^2	-	-		0.0139(6)	-	-
		Occ				$Co_{0.80(1)}Fe_{0.20(1)}$		
	4a	U_{iso} (Å^2)	-	-		0.0139(6)	-	-
		Occ				Sn		
FeSb P63/mmc	a (Å)		-	-	4.053(1)	-	-	-
	c (Å)				5.150(3)			
	Wt (%)		-	-	5.0(1)	-	-	-
		U_{iso} (Å^2)	-	-	0.012(1)	-	-	-
	χ^2		1.22	1.66	2.56	- 2.22	2.46	3.83
	wR_p (%)	Bank3	1.39	2.00	4.64	2.39	4.41	2.38
		Bank4	1.52	1.72	5.43	3.16	2.73	2.74
		Bank5	1.74	1.85	8.38	3.31	2.76	3.91
	R_p (%)	Bank3	2.32	3.31	6.68	3.24	6.04	4.31
		Bank4	3.38	3.51	5.99	3.76	5.51	4.28
		Bank5	2.42	5.72	7.92	6.63	5.91	6.21

4.5 SEM-EDX Analysis

This was performed on polished pieces of dense samples of B, C, D2, E2 and F1, prior to property measurements. The data on samples B and C can be found in Appendix 2. Low magnification (5000 ×) SEM backscattered electron and EDX layered images of the surface of these samples are displayed in Figure 4.3. The microstructure of samples D2 and E2 is smooth with small voids after polishing but no cracks, confirming the high density of these samples. Furthermore, the surface of these samples D2 and E2 is characterised by small grain sizes (< 5 μm), as previously observed in TiCoSb and the V, Sn co-doped samples (Chapter 3). Meanwhile, minor cracks and larger grains with variable sizes are noticeable for sample F1, which is consistent with the lower density of this sample. Some of the dark regions across these surfaces are associated either with elemental Ti or TiO_2. Brightness variation indicates the presence of inhomogeneities within these samples. More detailed compositional information of different regions across the surfaces of these samples is obtained by EDX analysis. As shown in Figure 4.3, sample D2 has two distinct regions; the matrix, which is composed of HH $Ti_{0.76(3)}V_{0.24(3)}Co_{0.92(2)}Fe_{0.08(2)}Sb_{0.90(1)}Sn_{0.10(1)}$ (VEC = 18.05e), and a segregated grey region, which has a FH composition $V_{1.0(1)}(Co_{0.64(1)}Fe_{0.36(1)})_2Sn_{0.91(1)}Sb_{0.09(1)}$. In the case of sample E2, three phases are detected; a HH matrix with a composition of $Ti_{0.75(2)}V_{0.25(2)}Co_{0.85(2)}Fe_{0.15(2)}Sb_{0.94(2)}Sn_{0.06(2)}$ (VEC = 18.04 e), a FH $Ti_{0.1(1)}V_{0.9(1)}(Co_{0.44(4)}Fe_{0.56(4)})_2Sn_{0.7(1)}Sb_{0.3(1)}$ and an alloy phase with general formula of $M_{1.5}X$ (Table 4.3). In addition, small inclusions of Sn appear in the backscattered electron images of samples D2 and E2 as small bright spots. Sample F1 shows a more homogenous distribution of the constituent elements. However, the matrix $Ti_{0.70(1)}V_{0.30(1)}Co_{0.61(4)}Fe_{0.39(4)}Sb$ (VEC = 17.91e) is interspersed with small regions identified again as $M_{1.5}X$. Table 4.3 summarises all the phases determined by EDX spectroscopy.

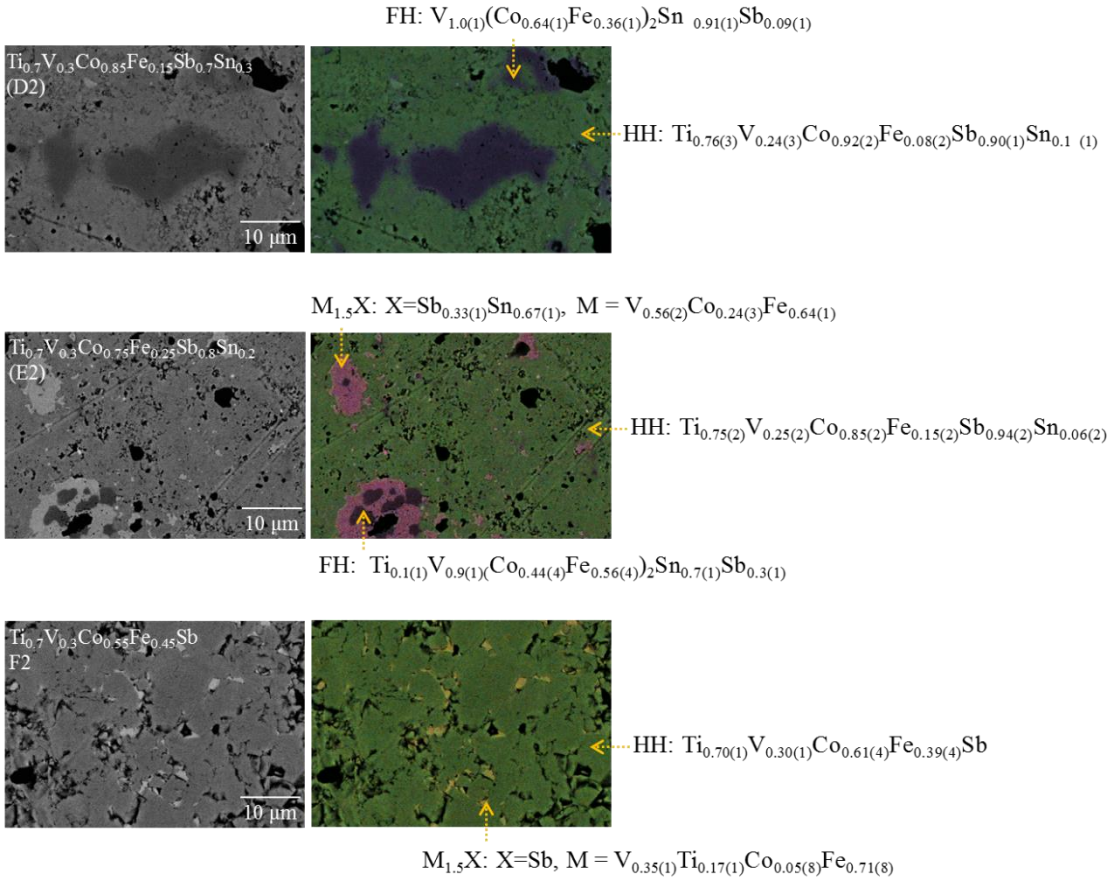

Figure 4.3. BSE/EDX images of samples D2: $Ti_{0.7}V_{0.3}Co_{0.85}Fe_{0.15}Sb_{0.7}Sn_{0.3}$, E2: $Ti_{0.7}V_{0.3}Co_{0.75}Fe_{0.25}Sb_{0.8}Sn_{0.2}$ and F1: $Ti_{0.7}V_{0.3}Co_{0.55}Fe_{0.45}Sb$. Compositions are an average of 4 regions of similar appearance. Standard deviations are derived from these 4 measurements.

Table. 4.3. Composition and phases of the samples D2, E2 and F1 as determined by EDX analysis. Compositions are an average of 4 regions of similar appearance. Standard deviations are derived from these 4 measurements.

SEM-EDX compositions	$Ti_{0.7}V_{0.3}Co_{0.85}Fe_{0.15}Sb_{0.7}Sn_{0.3}$ (D2)	$Ti_{0.7}V_{0.3}Co_{0.75}Fe_{0.25}Sb_{0.8}Sn_{0.2}$ (E2)	$Ti_{0.7}V_{0.3}Co_{0.55}Fe_{0.45}Sb$ (F1)
HH phase	$Ti_{0.76(3)}V_{0.24(3)}Co_{0.92(2)}Fe_{0.08(2)}Sb_{0.90(1)}Sn_{0.10(1)}$ (18.05e)	$Ti_{0.75(2)}V_{0.25(2)}Co_{0.85(2)}Fe_{0.15(2)}Sb_{0.94(2)}Sn_{0.06(2)}$ (18.04e)	$Ti_{0.70(1)}V_{0.30(1)}Co_{0.61(4)}Fe_{0.39(4)}Sb$ (17.91e)
FH phase	$V_{1.0(1)}(Co_{0.64(1)}Fe_{0.36(1)})_2Sn_{0.91(1)}Sb_{0.09(1)}$	$Ti_{0.1(1)}V_{0.9(1)}(Co_{0.44(4)}Fe_{0.56(4)})_2Sn_{0.7(1)}Sb_{0.3(1)}$	-
$M_{1.5}X$ phase	-	$(V_{0.56(2)}Co_{0.24(3)}Fe_{0.64(1)})Sb_{0.33(1)}Sn_{0.67(1)}$	$(V_{0.35(1)}Ti_{0.17(1)}Co_{0.05(8)}Fe_{0.71(8)})Sb$

4.6 Thermoelectric Properties

The temperature dependence of ρ, S and (S^2/ρ) of all samples are plotted in Figure 4.4. Measurements were made up to 723 K for the p - type samples B, C, F1 and F2 and up to 773 K for n-type samples D1, D2, E1 and E2. Both types will be discussed in more detail below.

4.6.1 P-type samples: B, C, F1, F2

The $\rho(T)$ of samples B ($TiCoSb_{0.85}Sn_{0.15}$) and C ($TiCo_{0.85}Fe_{0.15}Sb$) shows semiconducting behaviour, decreasing from values of 44 mΩ cm and 11 mΩ cm at room temperature to values of 16 mΩ cm and 5 mΩ cm at 723 K for samples B and C, respectively. Meanwhile, the V, Fe doped samples (F1, F2) show degenerate semiconducting behaviour, as ρ increases with increasing temperature. This may indicate the presence of conduction through an impurity band resulting from mixing of Ti/V and Co/Fe on the 4b and 4c sites. Sample F2 exhibit the lowest ρ values across the whole measurement range. A plot of $ln\rho(T)$ against inverse temperature for samples B and C is shown in Figure 4.5. The resistive band gap ($E_{g,\rho}$) can be then estimated from the linear fit to the ρ data using the Arrhenius equation $Ln\rho = Ln\rho_0 + E_{g,\rho}/2k_BT$, [124,125] where k_B is the Boltzman constant. A value of 0.06 eV was obtained for both samples B and C. The similar $S(T)$ and $Eg_{,\rho}$ for these two samples suggests that the difference in magnitude of ρ is likely due to microstructure effects. In addition, the thermal band gaps (E_g) were estimated using the Goldsmid-Sharp formula $E_g = 2eS_{max}T_{max}$. [21] This produced band gaps of 0.20 eV and 0.23 eV for B and C, respectively. These values are smaller than those observed for TiCoSb (E_g = 0.45 eV, Chapter 3) and this could be due to lower mobility of holes that dominate the conduction in p-type materials, which leads to lower maximum S and therefore decreasing the apparent thermal band gap. This

effect is known to lead to a 2-3 times underestimation of E_g for p-type TiNiSn.[126] The discrepancies between the thermal and resistive E_g are common because the thermal E_g is a better measure of the actual band gap, while the resistive E_g measures the energy cost of creating free holes. All samples show a positive *S*, indicating that the majority charge carriers are holes. The values of *S* for samples B and C initially increase with temperature, and then reach a maximum of ~ 170 μV K^{-1} and ~ 180 μV K^{-1} at 600 K and 670 K for samples B and C, respectively. This is followed by a decrease with increasing temperature, which is due to the excitation of electrons that occurs at high temperatures. In the case of samples F1 and F2, the temperature dependency of *S* shows a linear increase. Sample F2 attains the highest *S* value of ~ 225 μV K^{-1} at ~ 710 K. The lower *ρ(T)* and *S(T)* confirm that samples F1 and F2 are heavily doped degenerate semiconductors, while B and C are closer to intrinsic thermally activated behaviour. The Sn substituted sample (A) reaches a maximum S^2/ρ = 0.1 mW m^{-1} K^{-2}, while the Fe substituted sample (B) reaches a maximum S^2/ρ = 0.5 mW m^{-1} K^{-2}. However, the combination of low *ρ* and large *S* results in maximum S^2/ρ values of ~ 1 and 0.9 mW m^{-1} K^{-2} at 710 K for F2 and F1, respectively. These values are large for p-type doped TiCoSb and should lead to a high *ZT* and thus better energy conversion efficiency.

4.6.2 N-type samples: D1, D2, E1, E2

The temperature dependence of ρ for samples D1, D2, E1 and E2 clearly shows degenerate semiconducting behaviour, increasing with increasing temperature. As mentioned earlier, all of these samples have the same nominal doping level. Samples D1, D2 and E2 have very similar densities and lower than that of sample E1 (Table 4.1). These samples have resistivities in order of few mΩ cm over the whole measurement range. All measured *S(T)* are negative, indicating n-type behaviour. The S_{300K} values for these samples fall between -60 to -100 μV K^{-1} and smoothly increase to -110 to 190 μV K^{-1} at 823 K. Interestingly, the maximum *S* value in these samples was not reached over the measurement range, which is very promising in terms of thermoelectric application. The D samples have the lowest *S(T)* values and most linear *ρ(T)*, indicating that they may have higher n-type carrier concentration. Sample E1 has the largest S^2/ρ with a broad plateau near 0.8 mW m^{-1} K^{-2} between 600-823 K. This is enabled by its large *S(T)* and moderate *ρ(T)*. However, samples D1, D2 and E2 have considerably lower S^2/ρ values, increasing from 0.1-0.2 mW m^{-1} K^{-2} at 300 K to 0.3-0.4 mW m^{-1} K^{-2} at 823 K.

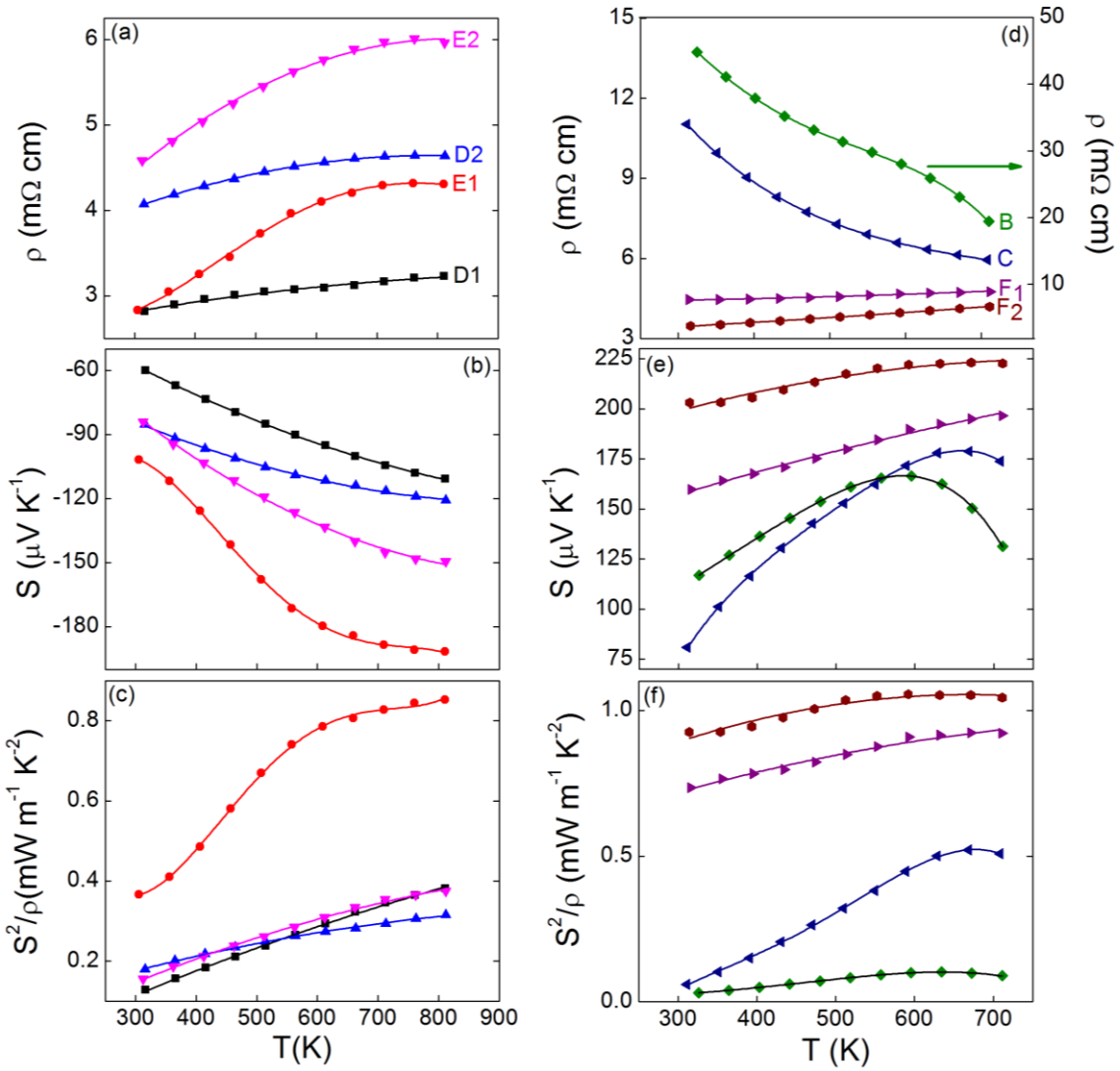

Figure 4.4. Temperature dependence of the electrical resistivity (ρ), Seebeck coefficient (*S*), and thermoelectric power factor (S^2/ρ) for the investigated samples, where D1, D2: $Ti_{0.7}V_{0.3}Co_{0.85}Fe_{0.15}Sb_{0.7}Sn_{0.3}$, E1, E2: $Ti_{0.7}V_{0.3}Co_{0.75}Fe_{0.25}Sb_{0.8}Sn_{0.2}$, F1, F2: $Ti_{0.7}V_{0.3}Co_{0.55}Fe_{0.45}Sb$, C: $TiCo_{0.85}Fe_{0.15}Sb$ and B: $TiCoSb_{0.85}Sn_{0.15}$. Solid lines are a guide to the eye.

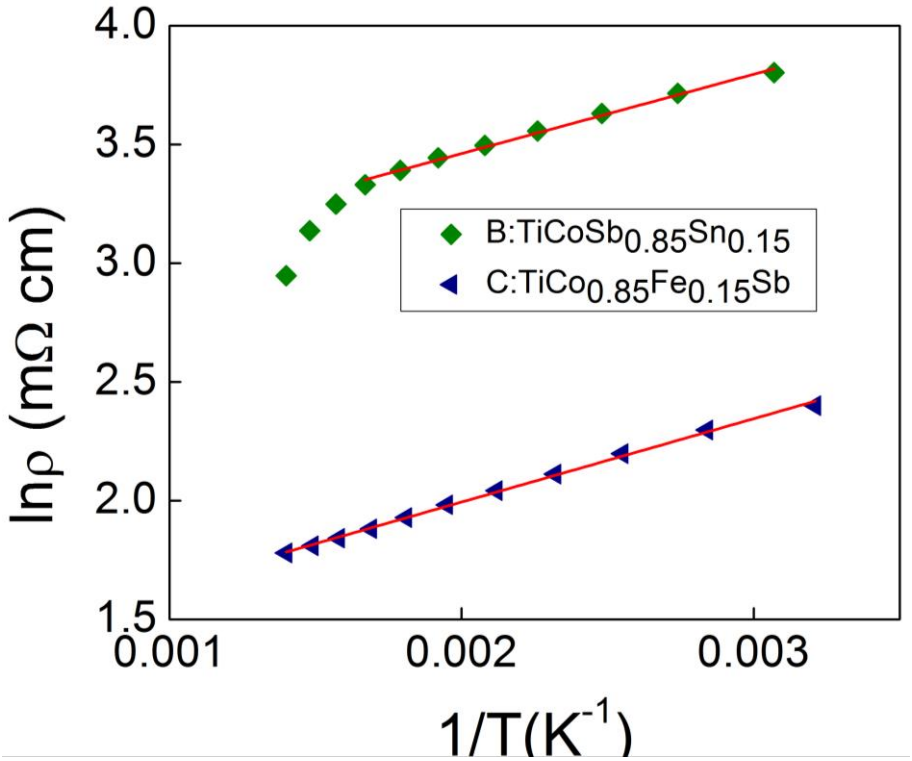

Figure 4.5. A plot of *lnρ(T)* against inverse temperature for samples B and C. Red lines are the Arrhenius fit to *ρ(T)* data for samples B and C.

4.6.3 Thermal Conductivity

This was performed on dense samples of D2 and F1 in the form of disc with 13 mm diameter. The temperature dependence of the κ, κ_{lat} and ZT for these two samples is displayed in Figure 4.6. κ was calculated using Equation 2.24, with C_p = 320 J kg^{-1} K^{-1}. The κ data were corrected to zero porosity using Klemens' equation: $\kappa_{measured}/\kappa_{100\%\ dense}$ = 1 - (4 / 3)ϕ, where ϕ = (100 - % density) / 100. κ_{lat} was then obtained by $\kappa_{lat} = \kappa - \kappa_e$, as described in Chapter 2. It is clear from Figure 4.6a that κ decreases with increasing temperature. Compared with the undoped compound, TiCoSb, κ_{lat} is significantly depressed, especially at room temperature. κ_{lat} values of 4.6 W m^{-1} K^{-1} and 5.6 W m^{-1} K^{-1} were achieved for samples D2 and F1 at room temperature, respectively. Meanwhile, a κ_{lat} of 18 W m^{-1} K^{-1} was reported for TiCoSb at room temperature. [77] Despite the difference in magnitude, in particular at 323 K, the $\kappa_{lat}(T)$ have a similar appearance for both samples. In particular, the $\kappa_{lat}(T)$ is closer to linear rather than following the *1/T* dependence that is expected for phonon transport limited by Umklapp scattering, and which is observed for many good thermoelectric materials. [26] This indicates that there is an additional significant scattering mechanism. A modified Callaway model was used to fit the $\kappa_{lat}(T)$ data [127] for both samples D2 and F1, in order

to investigate the scattering mechanisms that led to the reduction of κ_{lat} over the measurement range (Figure 4.6b, solid lines). No detailed information is available on Debye temperature, θ_D, and phonon velocity, υ, for these two samples, however, known values for TiCoSb were used to fit the data, namely θ_D = 415 K and phonons velocity approximated to be as constant and equals the velocity of sound $\upsilon_s = 3.23 \times 10^3$ m s^{-1}. [128] In the fitting undertaken here the boundary scattering parameter was fixed at L = 5 μm and the point defect (A) and Umklapp phonon (B) scattering parameters were allowed to vary. This yielded $A = 1.75 \times 10^{-41}$ s^3 and $B = 3.30 \times 10^{-19}$ s K^{-1} for sample D2 and $A = 1.11 \times 10^{-41}$ s^3 and $B = 5.43 \times 10^{-19}$ s K^{-1} for sample F1, suggesting a stronger contribution from point defect scattering, and weaker Umklapp scattering in sample D2. In addition to this, the magnitude of point defect scattering due to atomic mass and size differences on the Ti/V, Fe/Co and Sb/Sn sites can be calculated using Equation (4.1). [127]

$$A = \left(\frac{V}{4\pi v_s^3}\right)(\Gamma_M + \Gamma_S) \qquad \text{Equation (4.1)}$$

Where V is the atomic volume and Γ_M and Γ_S are the mass and strain disorder parameters. The procedure for the numerical determination of Γ_M and Γ_S is described in detail in reference. [129]

The Γ_S values depend sensitively on the used radii. Here, atomic radii are used. These are r_{Ti} = 1.40 Å, r_V = 1.35 Å, r_{Fe} = 1.40 Å, r_{Co} = 1.35 Å, r_{Sn} = 1.45 Å and r_{Sb} = 1.45 Å, [118]. Taking the strain disorder parameter, ε, which normally varies between 10-100 at its largest value (ε = 100) yields Γ_S = 0.014 (sample D2) and Γ_S = 0.019 (sample F1). These lead to a small predicted point defect scattering contribution (5-8 10^{-43} s^3), which is almost two orders of magnitude smaller than the value obtained from Callaway fit (Table 4.4). Clearly, the calculated Γ_M and Γ_S are not sufficient to fully explain the large reduction in κ_{lat}. This demonstrates that there must be additional phonon scattering centres within these samples that contribute to the reduction in κ_{lat}. Although the investigation of additional phonon scattering mechanisms may provide a further insight, however, it is difficult to draw any conclusions here, as the results obtained from Callaway fit should be also supported by some experimental evidence.

Table 4.4. Disorder scattering parameters for samples D2 ($Ti_{0.7}V_{0.3}Co_{0.85}Fe_{0.15}Sb_{0.7}Sn_{0.3}$) and F1 ($Ti_{0.7}V_{0.3}Co_{0.55}Fe_{0.45}Sb$). Γ_S was calculated based on the atomic radii. $A_{predicted}$ is the point defect scattering coefficient calculated from Γ_S and Γ_M using Equation (4.1). A_{Exp} is the point defect scattering coefficient obtained from Callaway fit to $\kappa_{lat}(T)$ data.

Sample	Γ_M	Γ_S	$A_{predicted}$ (s^3)	A_{Exp} (s^3)
D2	$2.99.10^{-4}$	$1.44.10^{-2}$	$5.75.10^{-43}$	1.75×10^{-41}
F1	$2.50.10^{-4}$	$1.94.10^{-2}$	$7.68.10^{-43}$	1.11×10^{-41}

4.6.4 Thermoelectric Figure of Merit

From the measured electrical and thermal properties, the dimensionless figure of merit *ZT* was calculated and are shown in Figure 4.6c. For samples D2 and F2 *ZT* increases with increasing temperature for both samples and reaches maximum values of 0.06 and 0.16 at around 773 K for D2 and F1, respectively. The higher *ZT* value observed for F1 is due to the larger S^2/ρ for this sample.

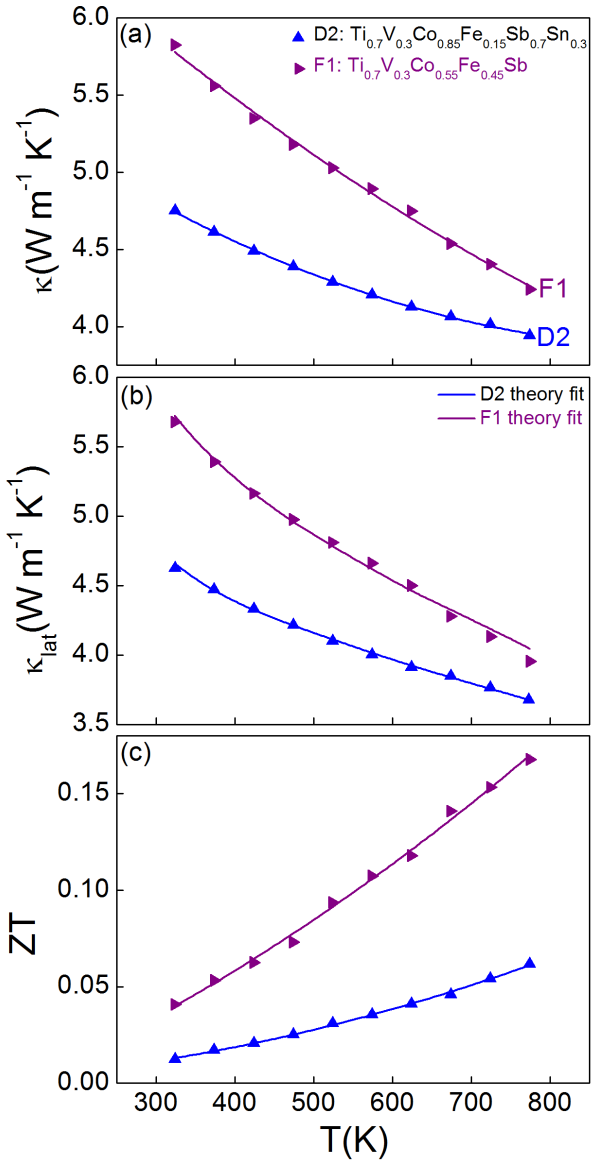

Figure 4.6. The temperature dependence of (a) total thermal conductivity, (b) lattice thermal conductivity and (c) *ZT* for samples D2 and F1. Solid lines in (a) and (c) are a guide to the eye.

4.7 Discussion

X-ray powder diffraction analysis of the $Ti_{1-X}V_xCo_{1-y}Fe_ySb_{1-z}Sn_z$ series demonstrated that these materials contain a single HH phase with the occasional presence of a minor FH phase and trace amounts of Sn and FeSb. Neutron data were also fitted using a single HH phase. Rietveld analysis of NPD data revealed the presence of ~ 2% Ta on the Ti-site for sample B ($TiCoSb_{0.85}Sn_{0.15}$), which was also observed for the parent compound, TiCoSb, and found to be caused by reaction with the sample containment material (Chapter 3). By contrast none of the Fe containing samples has any evidence for incorporation of Ta. The incorporation of the p-type dopant in both samples B and C ($TiCo_{0.85}Fe_{0.15}Sb$) was also confirmed from Rietveld fits, with apparent reduced amounts with respect to the nominal composition. The Rietveld fits for samples D1 ($Ti_{0.7}V_{0.3}Co_{0.85}Fe_{0.15}Sb_{0.7}Sn_{0.3}$), E1 ($Ti_{0.7}V_{0.3}Co_{0.75}Fe_{0.25}Sb_{0.8}Sn_{0.2}$) and F1 (($Ti_{0.7}V_{0.3}Co_{0.55}Fe_{0.45}Sb$) were carried out with keeping the Sb/Sn ratio fixed to its nominal ratio. This led to compositions close to the nominal compositions, with minimum χ^2 and calculated VEC between 17.8-17.9. Very similar compositions were also obtained by fixing the Sb/Sn site occupancy to the value obtained from SEM-EDX analysis. However, this insensitivity to the Sn/Sb occupancy makes the calculated VEC inaccurate and SEM and EDX reveal much more complicated story. Furthermore, neutron data also revealed the presence of elemental Ti phase in most samples (see Table 4.2 for weight fractions). The reason behind the existence of this unreacted Ti is still unclear, however, it is not expected to be the product of a degradation reaction, as one would expect to see simultaneously a CoSb phase from diffraction data, as previously discussed in Chapter 3. Electrical property measurements revealed the anticipated p-type conduction for samples B, C and F1. Meanwhile, samples D1 and E1 remain n-type despite attempts at p-type doping. SEM-EDX analysis revealed a relatively homogenous distribution of the elements for sample B, C and F2 that exhibited p-type conduction, except for the presence of small regions rich in Sn in sample B (Appendix 2, Figure 1). However, an inhomogeneous distribution of the constituent elements was apparent in the n-type samples D1 and E1. These included a HH phase with VEC > 18e (samples D1 and E1), a FH phase (sample D1) and an alloy phase $M_{1.5}X$ (sample E2) (See Table 4.4 for compositions). In addition to this, small segregated regions of Ti/TiO_2 and Sn were also detected in these samples. The occasional formation of TiO_2 may be caused by the oxidation of elemental Ti during polishing.

Generally, this type of behaviour has been linked to phase segregation driven by the stable electronic structure of the 18 valence electronic semiconducting HH compositions. This makes any substitution that changes the VEC ≠ 18 unfavourable. This has been widely observed in metal rich compositions such as $XNi_{1+y}Sn$, where spontaneous phase segregation into HH XNiSn and FH XNi_2Sn occurs. [90,91] In the case of the samples presented in this chapter, p-type behaviour was observed for the sample that does not contain Sn. This suggests that the presence of HH, FH and $M_{1.5}X$ phases in samples D and E is not likely due to the destabilisation of the highly stable 18 VEC structure. Clearly, the main issue in the deviation from targeted VEC = 17.85 is the poor uptake of Sn into the HH structure. This could be caused by a kinetic effect linked to the reaction pathway. Elemental Sn has by far the lowest melting point (232 °C) of the elements present (Sb is the nearest with 631°C) and it may be that this causes it to react first with the transition metals, forming stable phases. These are likely to be difficult to anneal out due to the slow diffusion of Sb and Sn which are the largest elements present in the reaction mixture. This is similar to the kinetic proposed trapping of Ti-rich and Zr/Hf-rich HH phases upon cooling from the melt. [81] A preliminary test using arc-melting, revealed an n- to p-type transition with modest positive magnitude for S < + 30 μV K^{-1} (Figure 4.7). This is entirely in keeping with much faster nature of the melting process causing Sn and Sb to be better dispersed throughout the sample. It suggests that pre-reacting Sn and Sb may be a possible route to prevent this issue, although the different crystal structures prevent the formation of a full solid solution.

To conclude, the data presented in this chapter suggest that the unexpected n-type conduction in these materials is caused by kinetic trapping of Sn caused by its low melting point, and do not suggest a significant thermodynamic barrier towards the formation of VEC < 18 samples.

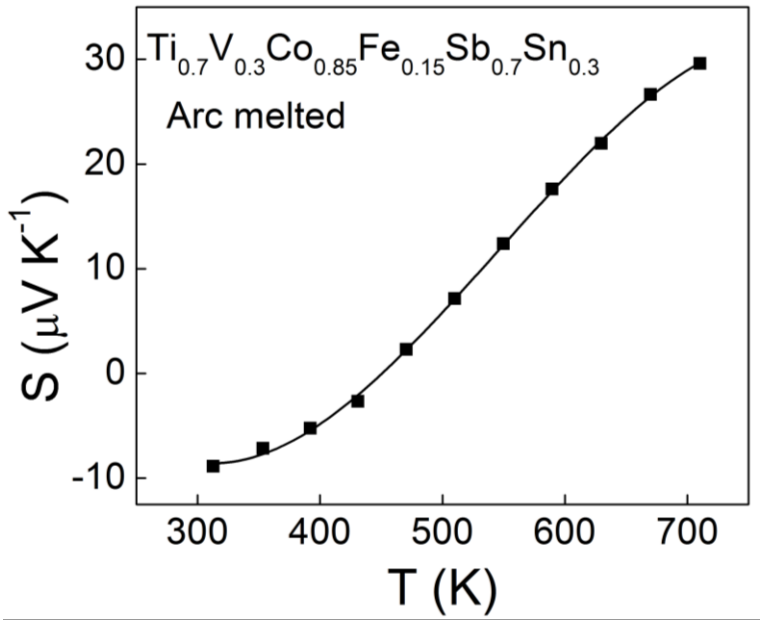

Figure 4.7. The temperature dependence of Seebeck coefficient for the arc melted $Ti_{0.7}V_{0.3}Co_{0.85}Fe_{0.15}Sb_{0.7}Sn_{0.3}$ composition.

Chapter 5-Synthesis, Structure and Properties of $(TiCoSb)_{1-x}$ $(TiM_2Sn)_x$ Nanocomposites

5.1. Introduction

Nanocomposites consisting of a HH matrix with segregated FH inclusions are now considered a promising strategy to improve thermoelectric efficiencies. [66] Studies on slightly Ni-rich TiNiSn (0-10 %) demonstrated that large reduction in κ as well as S^2/ρ improvements can be achieved through the spontaneous formation of FH nanoinclusions within the HH matrix.[89,91,130,131] Also, the effect of larger amount of excess Ni (> 10 %) was reported, revealing enhancement of *ZT* through the formation of micrometre-scale FH particles. [90,132] However, as mentioned in Chapter 1, TiCoSb-based nanocomposites are much less well explored. The aim of this work was therefore to explore the thermoelectric performance of TiCoSb based HH compounds prepared using the strategy of nanocomposites. Five series of $(TiCoSb)_{1-x}(TiM_2Sn)_x$ composites were prepared, with x value ranging from 0 to 0.2 and M_2 = Fe_2, FeCo, Co_2, CoNi, Ni_2. Here, we take advantage of the ability of these metals to occupy the vacant 4d tetrahedral site and thus form the relevant TiM_2Sn FH phase. Also, the Fe-Ni metals will provide a systematic investigation of the variation of the electronic configuration. The nominal compositions can be re-written as $Ti(Co_{1-x}M_x)M_xSb_{1-x}Sn_x$, containing various mole fractions of excess metal M. Samples were structurally characterised using X-ray powder diffraction and neutron powder diffraction. TEM was also employed to investigate the possible segregation of any FH nanoinclusions.

5.2. Synthesis

A preliminary series of $(TiCoSb)_{1-x}(TiM_2Sn)_x$ (M_2 = Fe_2, FeCo, Co_2, NiCo, Ni_2 and x = 0.1), were prepared on a 2g scale by a standard solid state reaction. Samples were initially annealed at 850 °C for 24 hours, then homogenised and annealed for a further 12 days. Samples were then subjected to a densification step using hot pressing at temperatures (850 °C ≤ T ≤ 885 °C) for 20 minutes under 80 Mpa. Subsequent series with x value ranging from 0 to 0.2 were prepared on a 3 g scale as described above. Finely ground powders were used for X-ray and neutron diffraction experiments. Rectangular bars were used for electrical property measurements. Thermal diffusivity measurements were carried out on dense disks of selected compositions using Linseis LFA 1000 device. TEM was performed on two compositions with M_2 = Fe_2, Ni_2 and x = 0.1.

5.3. X-ray Powder Diffraction Analysis

5.3.1. $(TiCoSb)_{0.9}(TiM_2Sn)_{0.1}$

Analysis of the X-ray diffraction patterns (Figure 5.1) of the preliminary series $(TiCoSb)_{0.9}(TiM_2Sn)_{0.1}$(M = Fe_2, FeCo, Co_2, CoNi and Ni_2) confirmed that the main diffraction peaks can be indexed to the HH structure. It is apparent from Figure 5.1 that these samples are pure, except for the presence of very small amount of FH phase as well as elemental Co in the sample with $M_2 = Co_2$. In addition, samples with M_2 = CoNi and Ni_2 contains trace amount of Ni_3Sn_2. A close up of the (220) reflection for each sample is shown also in Figure 5.1. It is clear that all peaks are sharp, except for the parent compound, $TiCoSb_{0.9}Sn_{0.1}$, which has a shoulder on the lower *2θ* side. This was also observed for $TiCoSb_{0.85}Sn_{0.15}$ presented in Chapter 4.

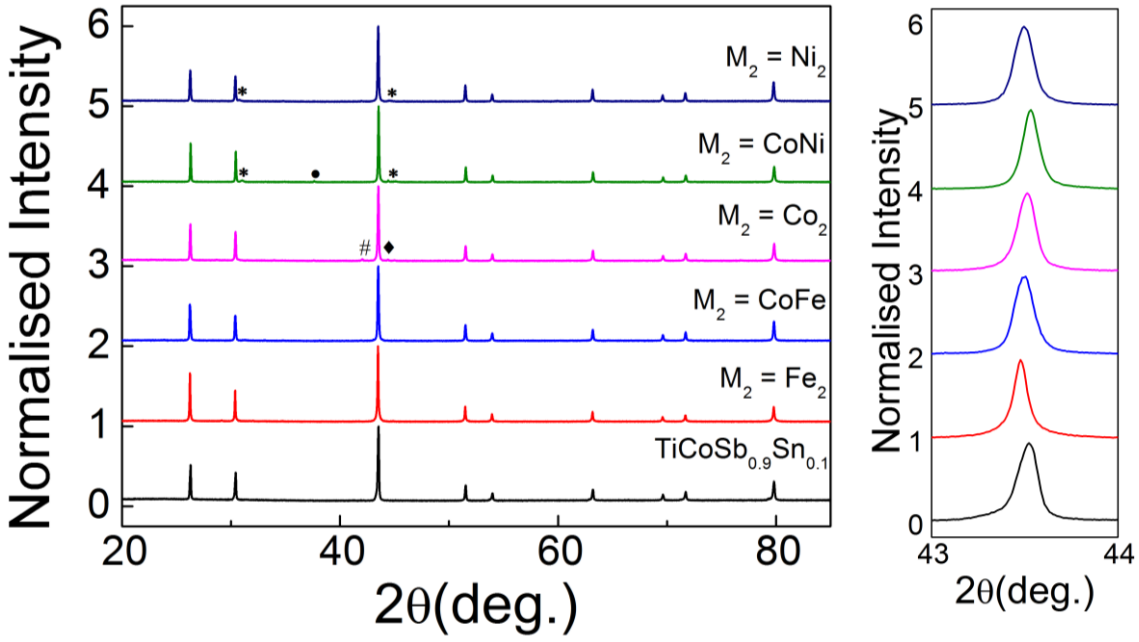

Figure 5.1. X-ray powder diffraction patterns for the $(TiCoSb)_{0.9}(TiM_2Sn)_{0.1}$ series. Data have been normalised and offset by 1. Where, *: Ni_2Sn_3, #: FH, ♦: Co and ●: unknown impurity, and a close up of the (220) reflection for each sample.

Table 5.1. Composition, lattice parameter, density, percentage density, room temperature ρ and S and maximum (S^2/ρ) for the preliminary $(TiCoSb)_{0.9}(TiM_2Sn)_{0.1}$.

Composition	a (Å)	Density ($g.cm^{-3}$)	% Density	ρ_{300k} (mΩ cm)	S_{300K} ($\mu V\ K^{-1}$)	$(S^2/\rho)_{max}$ ($mW\ m^{-1}\ K^{-2}$)
$TiCoSb_{0.9}Sn_{0.1}$	5.8869(1)	7.0	93	48.3	+29.7	0.10
$(TiCoSb)_{0.9}(TiFe_2Sn)_{0.1}$	5.8849(1)	7.0	93	37.8	+176.0	0.62
$(TiCoSb)_{0.9}(Ti(FeCo)Sn)_{0.1}$	5.8843(1)	5.6	76	102	+70.3	0.20
$(TiCoSb)_{0.9}(TiCo_2Sn)_{0.1}$	5.8848(1)	5.6	76	81.8	+23.0	0.06
$(TiCoSb)_{0.9}(Ti(CoNi)Sn)_{0.1}$	5.8868(1)	5.6	76	22.7	-145.4	0.26
$(TiCoSb)_{0.9}(TiNi_2Sn)_{0.1}$	5.8876(1)	5.6	76	6.0	-141.9	0.79

Rietveld analyses were carried out for all samples and the lattice parameters of the HH phases are summarised in table 5.1. From this table it can be seen that samples with $M_2 = Fe_2$, FeCo and Co_2 have very similar lattice parameters. A maximum lattice parameter of 5.8876(1) (Å) is observed for the sample with $M_2 = Ni_2$.

These samples were hot pressed at temperature = 850 °C. The density of the disk / bar shaped samples was calculated from their dimensions and the weight. The relative density was then determined from the theoretical density obtained from Rietveld refinement, which was found to be about 7.4 g/cm^3, and the experimental one. Subsequent series with $0.05 \leq x \leq 0.2$ were prepared. The results of structural analysis will be presented in an order where it was possible to gain some insight into the structure from Rietveld fit to NPD data.

5.3.2. $(TiCoSb)_{1-x}(TiNi_2Sn)_x$

Powder X-ray diffraction patterns of the $(TiCoSb)_{1-x}(TiNi_2Sn)_x$ (x = 0.05, 0.1, 0.15 and 0.2) series are presented in Figure 5.2. It is apparent from this figure that main peaks are matched with those for a HH structure. A secondary FH phase is detected in the samples with x = 0.15 and 0.2. The FH peaks are clearly enhanced with x increasing from 0.1 to 0.2. In addition to that, small amount of Ni_3Sn_2 impurity phase is evident in the x=0.1 and 0.2 samples. Lattice parameters of the HH phases of these samples are obtained from Rietveld fits and are listed in Table 5.2 For the sample with x = 0.05, the lattice parameter is very close to that of the parent compound $TiCoSb_{0.9}Sn_{0.1}$. Thereafter, the lattice parameter increases smoothly with increasing x value. This is also consistent with very slight peak shifting toward lower 2θ angles, as shown in the close up to the (220) reflection (Figure 5.2).

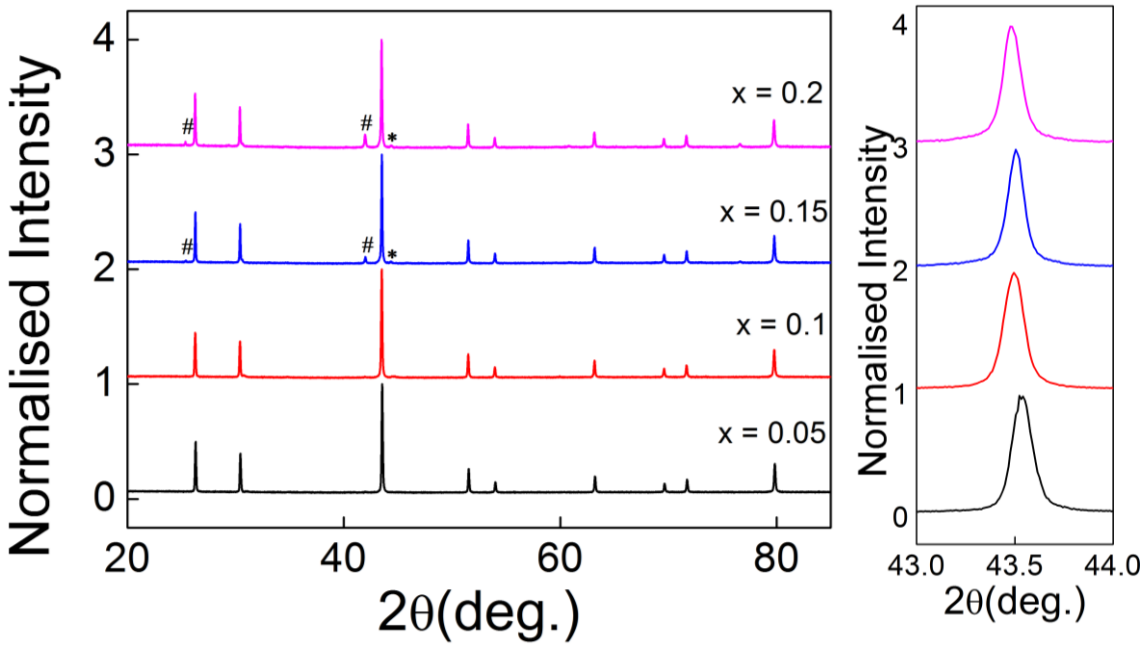

Figure 5.2. X-ray powder diffraction patterns for the $(TiCoSb)_{1-x}(TiNi_2Sn)_x$ series. Data have been normalised and offset by 1. Where, *: Ni_2Sn_3 impurity and #: FH secondary phase, and a close up of the (220) reflection.

Table.5.2. Composition, lattice parameter, density, percentage density, goodness of fit, room temperature ρ and S and maximum (S^2/ρ) for the $(TiCoSb)_{1-x}(TiNi_2Sn)_x$ series

Composition	a (Å)	Density ($g.cm^{-3}$)	% Density	ρ_{300k} (mΩ cm)	S_{300K} (μV K^{-1})	$(S^2/\rho)_{max}$ (mW m^{-1} K^{-2})
$(TiCoSb)_{0.95}(TiNi_2Sn)_{0.05}$	5.8866(1)	6.2	84	11.6	-183.6	0.52
$(TiCoSb)_{0.9}(TiNi_2Sn)_{0.1}$	5.8876(1)	6.8	92	6.0	-142	0.78
$(TiCoSb)_{0.85}(TiNi_2Sn)_{0.15}$	5.8882(1)	6.9	93	4.0	-112.8	0.50
$(TiCoSb)_{0.8}(TiNi_2Sn)_{0.2}$	5.8889(1)	7	95	1.8	-66.8	0.65

5.3.3. $(TiCoSb)_{1-x}(TiCoNiSn)_x$

The X-ray diffraction patterns for the x = 0.1 and 0.2 compositions are shown in Figure 5.3. The peaks are sharp and could be indexed by the HH structure. Small amount of Ni_3Sn_2 impurity phase appeared in both samples. A FH peak is identified in the sample with x = 0.2. Lattice parameters for both samples are obtained by Rietveld analysis and summarised in Table 5.3.

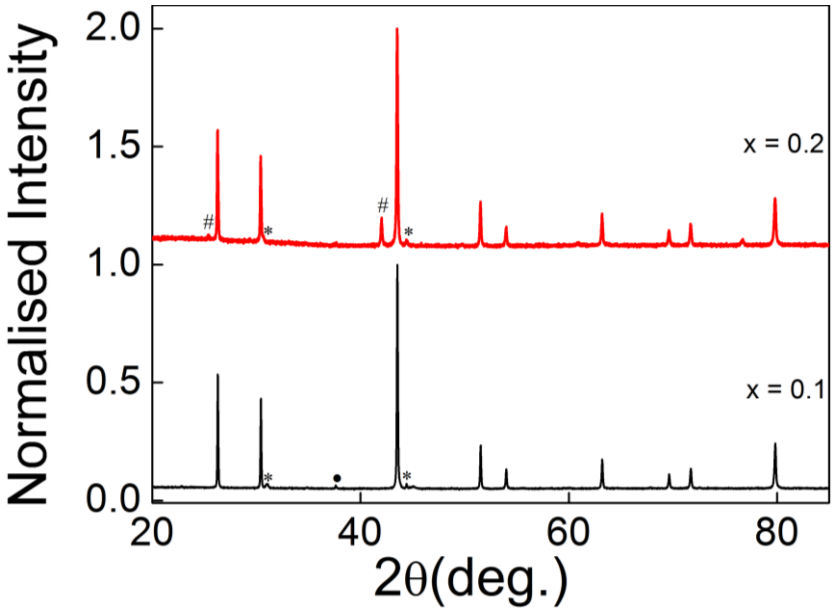

Figure 5.3. X-ray powder diffraction patterns for the $(TiCoSb)_{1-x}(TiNiCoSn)_x$ series. Data have been normalised and offset by 1. Where #: FH, *: Ni_3Sn_2 and ●: unindexed impurity phase.

Table 5.3. Composition, lattice parameter, density, goodness of fit, room temperature ρ and S and (S^2/ρ) for the $(TiCoSb)_{1-x}(TiNiCoSn)_x$ series.

Composition	a (Å)	Density ($g.cm^{-3}$)	% Density	ρ_{300k} ($m\Omega$ cm)	S_{300K} ($\mu V\ K^{-1}$)	$(S^2/\rho)_{max}$ ($mW\ m^{-1}\ K^{-2}$)
$(TiCoSb)_{0.9}(TiNiCoSn)_{0.1}$	5.8868(1)	5.6	76	22.7	-145	0.26
$(TiCoSb)_{0.8}(TiNiCoSn)_{0.2}$	5.8870(1)	6.7	90.5	11.6	-72	0.24

5.3.4. $(TiCoSb)_{1-x}(TiCo_2Sn)_x$

X-ray powder diffraction patterns of the $(TiCoSb)_{1-x}(TiNiCoSn)_x$ (x = 0.1, 0.2) samples are shown in Figure 5.4. Both samples contained a distinct FH phase. The lattice parameters of the HH phases of these two samples increases with x (Table 5.4).

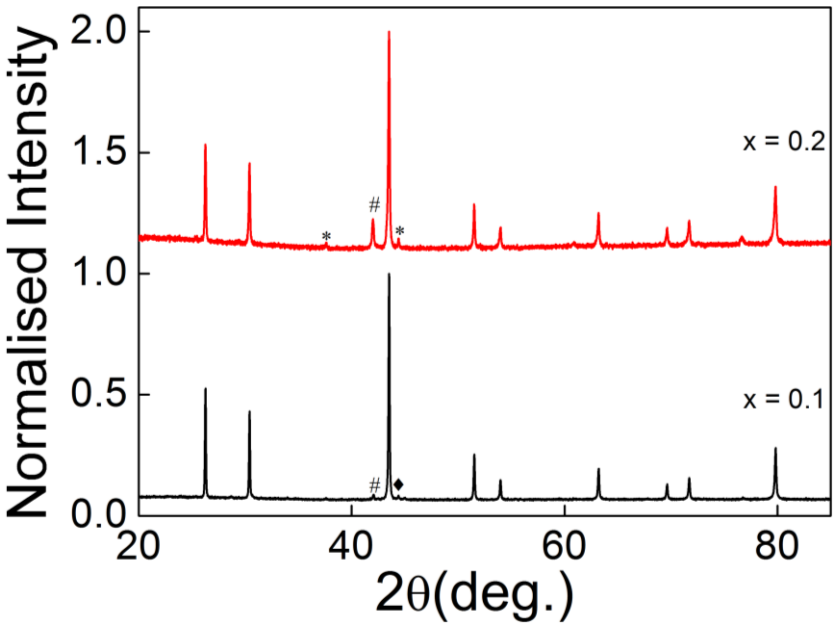

Figure 5.4. X-ray powder diffraction patterns for the $(TiCoSb)_{1-x}(TiCo_2Sn)_x$ series. Data have been normalised and offset by 1. Where #indicates the peaks belonging to the FH phase, * represents TiCo impurity phase and the peak marked ♦ indicates elemental Co.

Table 5.4. Composition, lattice parameter, density, goodness of fit, room temperature ρ and S and $(S^2/\rho)$for the $(TiCoSb)_{1-x}(TiCo_2Sn)_x$ series.

Composition	a (Å)	Density ($g.cm^{-3}$)	% Density	ρ_{300k} (mΩ cm)	S_{300K} (μV K^{-1})	$(S^2/\rho)_{max}$ (mW m^{-1} K^{-2})
$(TiCoSb)_{0.9}(TiCo_2Sn)_{0.1}$	5.8848(1)	5.6	76	81.8	23	0.066
$(TiCoSb)_{0.8}(TiCo_2Sn)_{0.2}$	5.8865(1)	6.9	93	25.4	-12	0.024

5.3.5. $(TiCoSb)_{1-x}(TiFe_2Sn)_x$ and $(TiCoSb)_{1-x}(TiFeCoSn)_x$

As above, the structure of all samples was confirmed by powder X-ray diffraction. The X-ray patterns of both series are provided in Figures 5.5 and 5.6. Samples look very pure. In both series, no obvious peak that could indicate the presence of the FH phase was observed, suggesting that almost all elements are present within the HH structure. The lattice parameters for all samples were evaluated from Rietveld fits to powder X-ray data and provided in Table 5.5.

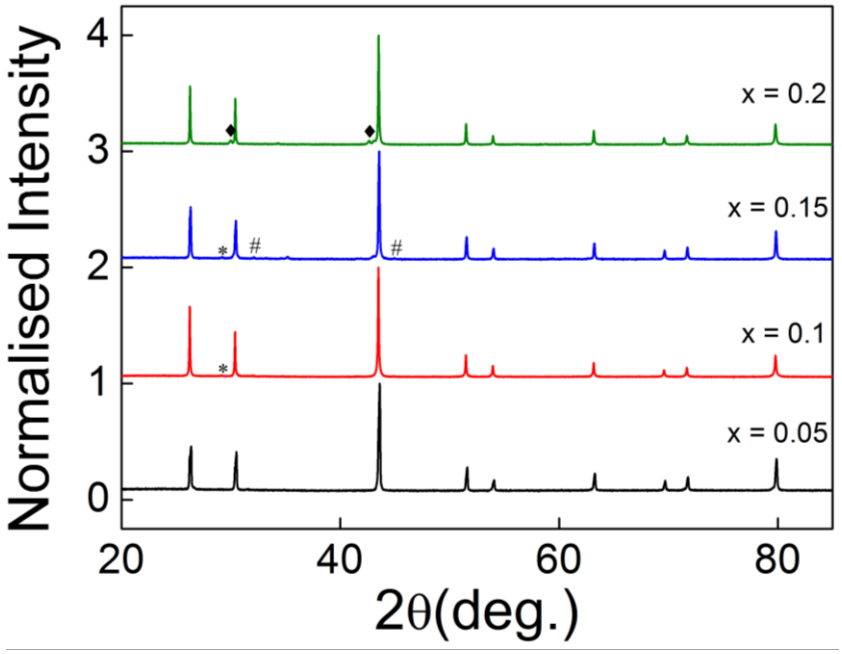

Figure 5.5. Representative X-ray powder diffraction patterns of the $(TiCoSb)_{1-x}(TiFe_2Sn)_x$ series. Data have been normalised and offset by 1. * indicates peaks belonging to SbSn impurity phase, # represents Sn and peaks marked ♦ belong to Fe_2Sn.

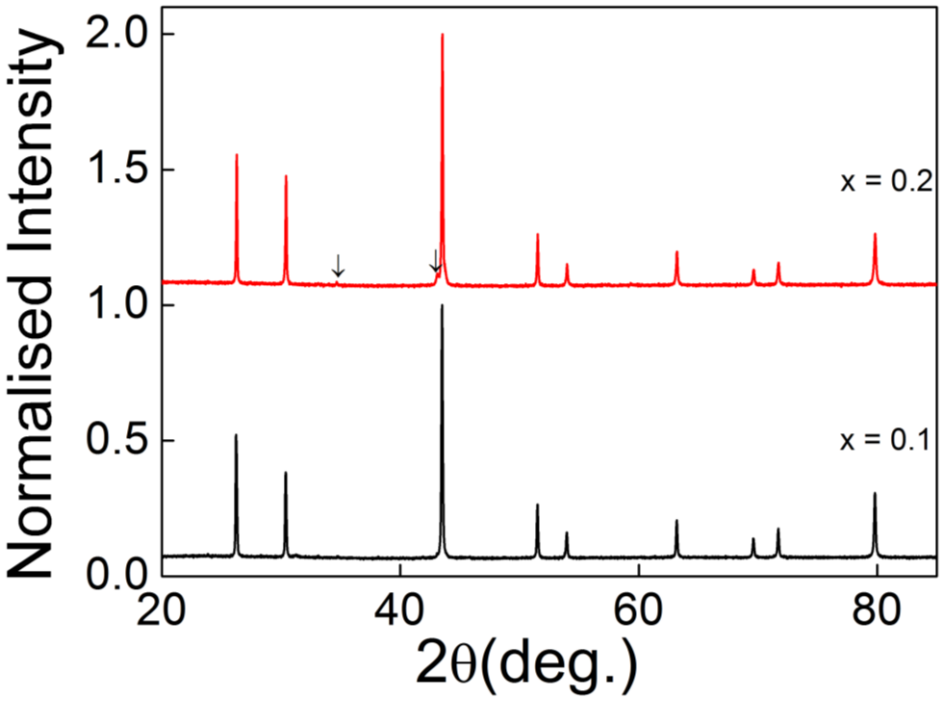

Figure 5.6. X-ray powder diffraction patterns of the $(TiCoSb)_{1-x}(Ti(FeCo)Sn)_x$ series. Data have been normalised and offset by 1. The arrow indicates peaks belonging to Co_3Sn_2.

Table 5.5. Composition, lattice parameter, density, percentage density, goodness of fit, room temperature ρ and S and maximum (S^2/ρ) for both $(TiCoSb)_{1-x}(TiFe_2Sn)_x$ and $(TiCoSb)_{1-x}(Ti(FeCo)Sn)_x$.

Composition	a (Å)	Density ($g.cm^{-3}$)	% Density	ρ_{300k} (mΩ cm)	S_{300K} (μV K^{-1})	$(S^2/\rho)_{max}$ (mW m^{-1} K^{-2})
$(TiCoSb)_{0.95}(TiFe_2Sn)_{0.05}$	5.8849(1)	6.4	86	75.6	-105.8	0.04
$(TiCoSb)_{0.9}(TiFe_2Sn)_{0.1}$	5.8849(1)	7	95	37.8	176.0	0.61
$(TiCoSb)_{0.85}(TiFe_2Sn)_{0.15}$	5.8859(1)	7.2	97	4.2	55.5	0.43
$(TiCoSb)_{0.8}(TFe_2Sn)_{0.2}$	5.8870(1)	7.0	95	7.4	111.5	0.83
$(TiCoSb)_{0.9}(Ti(FeCo)Sn)_{0.1}$	5.8843(1)	5.6	76	102	70	0.19
$(TiCoSb)_{08}(Ti(FeCo)Sn)_{0.2}$	5.8854(1)	7.3	98	9	39	0.17

5.4. Neutron Powder Diffraction

Neutron powder diffraction experiments were carried out on 13 compositions. Data were collected on approximately 1.5 g of each sample, using the Polaris instrument at the ISIS neutron facility, Oxfordshire. Rietveld refinements of the collected data are discussed in more detail below.

5.4.1. $TiCoSb_{0.9}Sn_{0.1}$

This sample was analysed in exactly the manner as the one presented in Section 4.4. The best fit was obtained by adding Ta to the Ti site. Rietveld fit revealed the presence of ~ 1% Ta on this site. The fit is presented in Figure 1, Appendix 3.

5.4.2. $(TiCoSb)_x(TiNi_2Sn)_x$

Neutron data were collected on compositions with x = 0.1, 0.15 and 0.2. The segregation of nano-or micro-inclusions of the FH $TiNi_2Sn$ is expected here. This is driven by the insolubility of the HH/FH phases due to large energy barrier resulting from disrupting the highly stable 18 VEC HH structure. [133–135] Two models were tested in order to fit the data. These include a HH phase with nano-FH inclusions or a HH phase and a distinct FH phase. Assuming that the HH matrix contains nanosegregated FH phase, the data can be fitted equivalently using two models. The first one is a metal-rich HH phase, $Ti(Co_{1-x}Ni_x)(Ni_x)Sb_{1-x}Sn_x$ that suggests the presence of Ni on both 4c and 4d sites, while the other equivalent is a mixture of (1-x)TiCoSb and $x(TiNi_2Sn)$ with the same lattice parameter. This was initially explored for the sample with x =0.1, which did not contain any district FH phase (Figure 5.2). In the case of a metal rich HH phase, a simultaneous refinement of the 4c and 4d site occupancies, while fixing the

other site occupancies to their nominal values, indicated a negative Ni occupancy of the 4d site, while the 4c site yielded a composition of $Co_{0.84(1)}Ni_{0.16(1)}$, with $\chi^2 = 2.7$. In addition, Rietveld fitting using a mixture of the HH and FH phases with the same lattice parameter, led to a large overestimation of the (222) and (420) reflections, with $\chi^2 = 9.7$. Clearly, it is not possible to obtain satisfactory fits either of these two models and this may be an evidence for the absence of any nanosegregated FH phase in this sample. This indicates that most of the excess Ni is associated with the HH phase. Thus, the final model was explored by adding Ni to the 4c site and keeping the other site occupancies fixed to their nominal values. A refinement of the (Co, Ni) ratio revealed a composition of $Co_{0.87(1)}Ni_{0.13(1)}$ on the 4c site, with $\chi^2 = 2.2$. In this case, the amount of Ni is in a good agreement with the nominal composition, taking in account the presence of the 4 wt% of Ni_3Sn_2 impurity phase. Samples with x = 0.15 and 0.2 were analysed in a similar manner and the data were fitted using a $TiCo_{1-x}Ni_xSb_{1-x}Sn_x$ HH phase and a distinct $TiNi_2Sn$ FH phase. The results of Rietveld fits for these 3 samples are summarised in Table. 5.6, and the fits are presented in Figure 5.7. To conclude, Rietveld analysis revealed that the $(TiCoSb)_{1-x}(TiNi_2Sn)_x$ consists of a Ni-doped HH matrix. For the sample with x = 0.1 the majority of excess Ni is associated with the HH phase, while for $x \geq 0.15$ the data can be fitted using a Ni-doped HH and a distinct FH phase and thus the excess Ni is divided over the HH, FH and Ni_3Sn_2 phases. Interestingly, the amount of Ni in the HH matrix for the x = 0.1-0.2 compositions is similar. This conclusion is in agreement with the results obtained from X-ray powder diffraction, which revealed very similar lattice parameter for the HH phases upon the partial substitution of Co by Ni, due to the presence of almost the same amount of Ni on the 4c site.

Table 5.6. Lattice parameters (a), weight percentages, thermal displacement parameters (U_{iso}/Å^2), fractional occupancies and fit statistics for Rietveld refinement of neutron powder diffraction data collected for the $(TiCoSb)_{1-x}(TiNi_2Sn)_x$ series.

x		0.1	0.15	0.2
		HH (F-43m)		
a (Å)		5.8864(1)	5.8848(1)	5.8858(1)
wt (%)		93.0(1)	86.6(1)	82(1)
4b	U_{iso} (Å^2)	0.0041(1)	0.0041(1)	0.0043(1)
	Occ	Ti	Ti	Ti
4c	U_{iso} (Å^2)	0.0041(1)	0.0041(1)	0.0043(1)
	Occ	$Co_{0.87(1)}Ni_{0.13(1)}$	$Co_{0.87(1)}Ni_{0.13(1)}$	$Co_{0.84(1)}Ni_{0.16(1)}$
4a	U_{iso} (Å^2)	0.0041(1)	0.0041(1)	0.0043(1)
	Occ	$Sb_{0.9}Sn_{0.1}$	$Sb_{0.85}Sn_{0.15}$	$Sb_{0.8}Sn_{0.2}$
		FH(Fm-3m)		
a (Å)			6.0894(1)	6.0919(1)
wt (%)			5.7(1)	9.6(1)
4b	U_{iso} (Å^2)		0.0016(3)	0.0027(2)
	Occ		Ti	Ti
8c	U_{iso} (Å^2)		0.0136(3)	0.0151(2)
	Occ		Ni	Ni
4a	U_{iso} (Å^2)		0.0017(3)	0.0027(2)
	Occ		Sn	Sn
		Ti(P63/mmc)		
a (Å)		2.980(1)	2.974(1)	2.966(1)
c (Å)		4.501(1)	4.535(1)	4.560(1)
wt (%)		4.0(1)	3.9(1)	3.9(1)
	U_{iso} (Å^2)	0.0105(4)	0.0116(4)	0.0111(3)
		Ni_3Sn_2(P63/mmc)		
a (Å)		4.0728(1)	4.0874(1)	4.0858(1)
c (Å)		5.1696(1)	5.1888(1)	5.1868(3)
wt (%)		4.0(1)	3.9(1)	3.9(1)
	U_{iso} (Å^2)	0.0105(4)	0.0116(4)	0.0111(3)
Average composition		$TiCo_{0.81(1)}Ni_{0.24(1)}Sb_{0.9}Sn_{0.1}$	$TiCo_{0.75(1)}Ni_{0.34(1)}Sb_{0.85}Sn_{0.15}$	$TiCo_{0.695(1)}Ni_{0.44(1)}Sb_{0.8}Sn_{0.2}$
χ^2		2.20	1.35	3.38
wRp (%)	Bank3	1.45	2.09	2.25
	Bank4	1.64	2.24	2.78
	Bank5	1.56	2.24	3.34
R_p (%)	Bank3	2.14	3.15	2.86
	Bank4	3.09	5.39	5.31
	Bank5	4.54	7.62	5.03

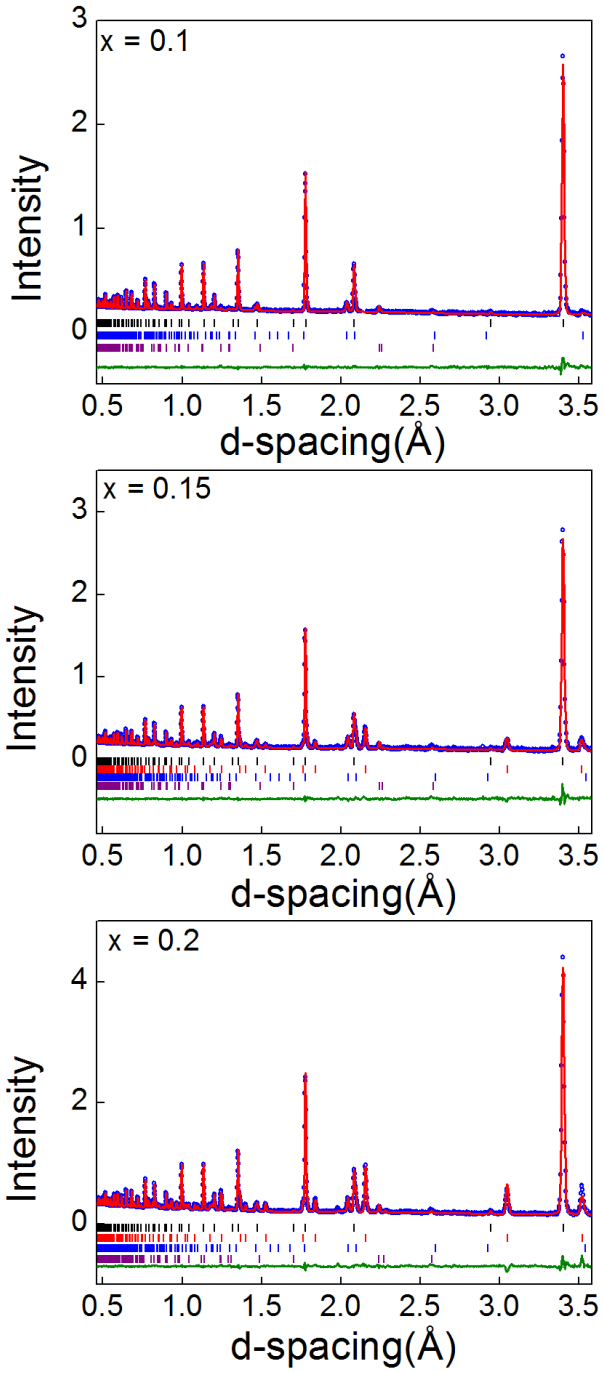

Figure 5.7. Rietveld refinement to neutron powder diffraction data collected for the $(TiCoSb)_{1-x}(TiNi_2Sn)_x$ series. Blue circles represent the collected data, red line is the calculated fit and the green line is the difference curve. Black tickmarks are for the HH phase, red tickmarks are for the FH phase, blue tickmarks are for Ni_3Sn_2 and purple tickmarks are for Ti. Data shown are from detector bank 4.

5.4.3. $(TiCoSb)_{1-x}(TiCoNiSn)_x$

Data were initially fitted for the sample with x = 0.1, which did not contain any district FH reflections. Initial refinement of the Co occupancy on the 4c site yielded unrealistically large occupancy, indicating that Ni was present. The best fit was obtained with substitution of Ni on the 4c site, which will have then a mixture of Co and Ni, and displacement of Co to the vacant 4d site. A simultaneous refinement of the 4c and 4d site occupancies revealed a composition of $Co_{0.93(1)}Ni_{0.07(1)}$ on the 4c site, while the 4d site contained 7% Co. This result is close to the nominal composition, considering the presence of small amounts of impurities (Table 5.7). In the case of the x = 0.2 sample, the data were fitted using a metal rich HH phase and a distinct FH phase $Ti(Co_{0.34(1)}Ni_{0.66(1)})_2Sn$. The fit indicated similar 4c and 4d site occupancies for this sample. This may explain the similar HH lattice parameters of these two samples obtained by powder X-ray diffraction (Table 5.3). The results of Rietveld analysis are summarised in Table 5.7 and the fits are presented in Figure 5.8.

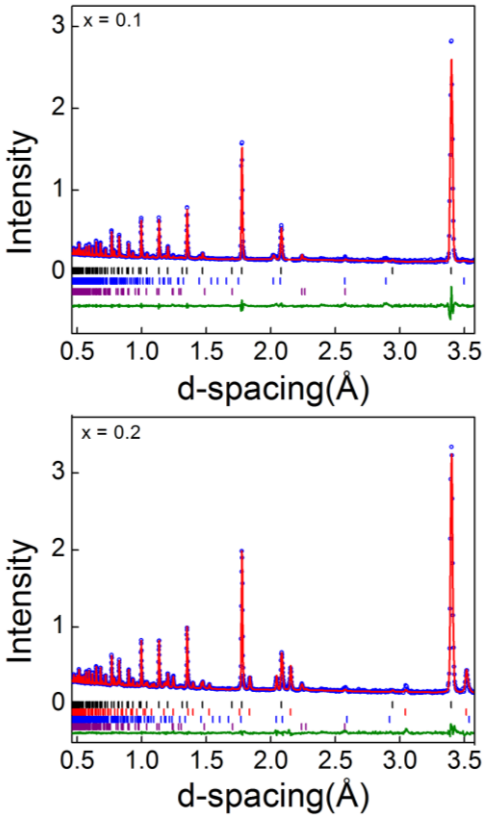

Figure 5.8. Rietveld refinement to neutron powder diffraction data collected for the $(TiCoSb)_{1-x}(Ti(CoNi)Sn)_x$ series. Blue circles represent the collected data, red line is the calculated fit and the green line is the difference curve. Black tickmarks are for the HH phase, red tickmarks are for the FH phase, blue tickmarks are for Ni_3Sn_2 and purple tickmarks are for elemental Ti. Data shown are from bank 4.

Table 5.7. Lattice parameters (a), weight percentages, thermal displacement parameters (U_{iso}/Å^2), fractional occupancies, average compositions and fit statistics for Rietveld refinement of neutron powder diffraction data collected for the $(TiCoSb)_{1-x}(Ti(CoNi)Sn)_x$ series.

x		0.1	0.2
		HH(F-43m)	
a (Å)		5.8831(1)	5.8850(1)
wt (%)		95.0(1)	87.0(1)
4b	U_{iso} (Å^2)	0.0039(1)	0.0041(1)
	Occ	Ti	Ti
4c	U_{iso} (Å^2)	0.0039(1)	0.0041(1)
	Occ	$Co_{0.93(1)}Ni_{0.07(1)}$	$Co_{0.93(1)}Ni_{0.07(1)}$
4a	U_{iso} (Å^2)	0.0039(1)	0.0040(1)
	Occ	$Sb_{0.9}Sn_{0.1}$	$Sb_{0.8}Sn_{0.2}$
4d	U_{iso} (Å^2)	0.0039(1)	0.0041(1)
	Occ	$Co_{0.07(1)}$	$Co_{0.07(1)}$
		FH(Fm-3m)	
a (Å)			6.0863(1)
wt (%)			7.0(1)
4b	U_{iso} (Å^2)		0.0052(2)
	Occ		Ti
8c	U_{iso} (Å^2)		0.0052(2)
	Occ		$Co_{0.34(1)}Ni_{0.66(1)}$
4a	U_{iso} (Å^2)		0.0052(2)
	Occ		Sn
		Ti(P63/mmc)	
a (Å)		2.974(1)	2.970(1)
c (Å)		4.533(1)	4.542(2)
wt (%)		2.5(1)	3.0(1)
	U_{iso} (Å^2)	0.009(1)	0.018(2)
		Ni_3Sn_2(P63/mmc)	
a (Å)		4.0399(4)	4.0845(1)
c (Å)		5.1463(9)	5.1801(3)
wt (%)		2.5(1)	3.0(1)
	U_{iso} (Å^2)	0.0125(7)	0.0138(4)
Average composition		$TiCo_{0.95(1)}Ni_{014(1)}Sb_{0.9}Sn_{0.1}$	$TiCo_{0.91(1)}Ni_{0.21(1)}Sb_{0.8}Sn_{0.2}$
χ^2		1.96	2.19
wRp (%)	Bank3	1.97	1.84
	Bank4	3.53	1.84
	Bank5	1.96	3.05
R_p (%)	Bank3	3.17	3.07
	Bank4	6.48	3.53
	Bank5	4.75	5.00

5.4.4. $(TiCoSb)_{1-x}(TiCo_2Sn)_x$

Both samples contained distinct FH phases. The best fits were obtained by the displacement of excess Co to the vacant 4d site. Fixing the other site occupancies to their nominal values and allowing the Co occupancy to refine freely on the 4d site yielded about 8% of Co on this site for the sample with x = 0.1, χ^2 = 1.85 . However, for the sample with x = 0.2, the fit indicated that this site is slightly over-occupied with Co and led to a significant difference of the average composition of this sample as compared to the nominal one. The representative Rietveld fits of these two samples are shown in Figure 5.9 and the results of Rietveld analysis are provided in Table 5.8.

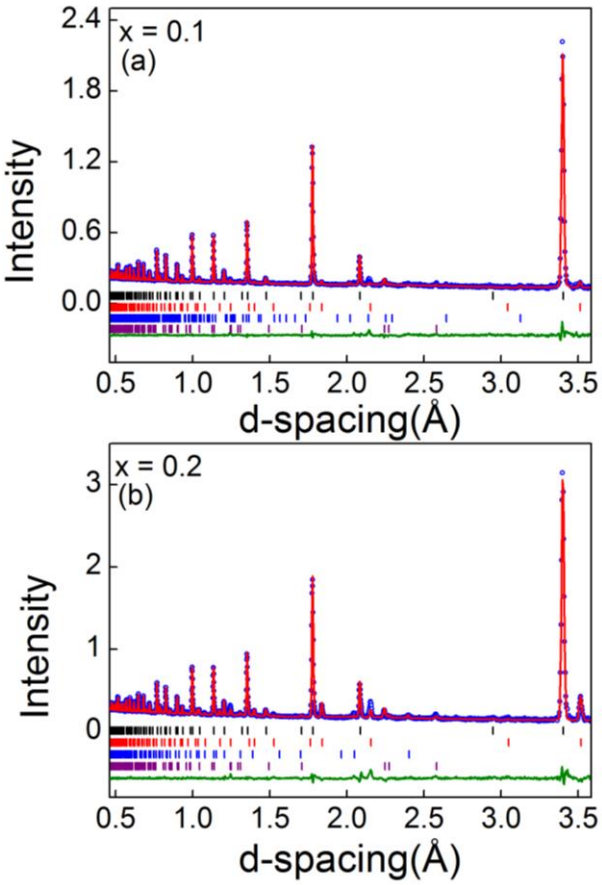

Figure 5.9. Rietveld refinement to neutron powder diffraction data collected for the $(TiCoSb)_{1-x}(TiCo_2Sn)_x$ series. Blue circles represent the collected data, red line is the calculated fit and the green line is the difference curve. Black tickmarks are for the HH phase, red tickmarks are for the FH phase, blue tickmarks are for $CoSn_2$ (1.7 wt%) and TiCo (5.1 wt%) in (a) and (b), respectively and the purple tickmarks are for elemental Ti. Data shown are from bank 4.

Table 5.8. Lattice parameters (a), weight percentages, thermal displacement parameters (U_{iso}/Å^2), fractional occupancies, average compassions and fit statistics for Rietveld refinement of neutron powder diffraction data collected for the $(TiCoSb)_{1-x}(TiCo_2Sn)_x$ series.

x		0.1	0.2
	HH(F-43m)		
a (Å)		5.8835(1)	5.8844(1)
wt (%)		91.0(1)	79.0(1)
4b	U_{iso} (Å^2)	0.0039(1)	0.0041(1)
	Occ	Ti	Ti
4c	U_{iso} (Å^2)	0.0039(1)	0.0041(1)
	Occ	Co	Co
4a	U_{iso} (Å^2)	0.0039(1)	0.0040(1)
	Occ	$Sb_{0.9}Sn_{0.1}$	$Sb_{0.8}Sn_{0.2}$
4d	U_{iso} (Å^2)	0.0039(1)	0.0041(1)
	Occ	$Co_{0.08(1)}$	$Co_{0.23(1)}$
	FH(Fm-3m)		
a (Å)		6.0765(4)	6.0848(1)
wt (%)		2.5(1)	12.0(1)
4b	U_{iso} (Å^2)	0.009(1)	0.0063(2)
	Occ	Ti	Ti
8c	U_{iso} (Å^2)	0.009(1)	0.0063(2)
	Occ	Co	Co
4a	U_{iso} (Å^2)	0.0091(1)	0.0063(2)
	Occ	Sn	Sn
		Ti	
a (Å)		2.973(1)	2.974(1)
c (Å)		4.534(1)	4.538(1)
wt (%)		2.8(1)	3.9(1)
	U_{iso} (Å^2)	0.009(1)	0.009(1)
Average composition		$TiCo_{1.14(1)}Sb_{0.9}Sn_{0.1}$	$TiCo_{1.47(1)}Sb_{0.9}Sn_{0.1}$
χ^2		1.85	3.64
wRp (%)	Bank1	1.32	3.38
	Bank2	1.57	3.10
	Bank3	1.64	3.69
R_p (%)	Bank1	2.25	5.22
	Bank2	3.14	5.44
	Bank3	4.13	5.74

5.4.5. $(TiCoSb)_{1-x}(TiFe_2Sn)_x$ and $(TiCoSb)_{1-x}(TiFeCoSn)_x$

In the case of these two series, none of the samples contained any peaks that that could indicate the presence of the FH phase, however, trace amount of impurities were detected (Figures 5.5 and 5.6). This indicates that the excess metal should be associated with the HH phase. However, attempts to fit the data to a metal rich HH phase model led to unsatisfactory results for both series, suggesting the absence of any nanosegregated FH phase. Other models were also tested, but no satisfactory conclusion could be obtained. The models that are used to fit the data and the Rietveld fits of the representative neutron data collected for all of these samples are provided in Appendix 3. Detailed electron microscopy analysis is required to investigate this further.

5.5. Transmission Electron Microscopy

TEM was carried out for two compositions, $(TiCoSb)_{0.85}(TiNi_2Sn)_{0.15}$ and $(TiCoSb)_{0.9}(TiFe_2Sn)_{0.1}$. Freshly densified pieces of these two samples were used and a detailed TEM analysis of each composition is provided in Sections 5.5.1 and 5.5.2.

5.5.1. $(TiCoSb)_{0.85}(TiNi_2Sn)_{0.15}$

A low resolution STEM image (scanning TEM) for the whole FIB-SEM (Focussed Ion-Beam Scanning Electron Microscopy) prepared lamella is presented in Figure 5.10(I). The regions that have been studied are indicated. It can be seen from this figure that the sample is characterised by small grain sizes (< 2μm), which is usually observed for TiCoSb based HH compounds (Chapter 3). In addition to that, some grains are seen to have very small dark features. Figure 5.10(II) shows an STEM image and EDS/EELS (Electron Energy Loss Spectroscopy) maps for a given grain boundary and one of these features. EDS analysis suggests that this feature is rich in Ti and O, while all other elements are reduced. Furthermore, Ni segregation is obvious at the grain boundary. Figure 5.10(III) depicts an area across three grains and variation in brightness is evident. The EELS map shows a compositional variation across the grains, with reduction in Co in the central grain. In addition to this, a very small region rich in Ti can be observed from this figure.

This analysis has therefore revealed that there is no obvious segregation of any FH nanoinclusions. This result is in keeping with the results obtained from neutron powder diffraction analysis, which showed that the $(TiCoSb)_{1-x}(TiNi_2Sn)_x$ series does not have tendency to accommodate the excess Ni in the vacant 4d site of the HH structure, and instead Ni prefers to substitute to the 4c site.

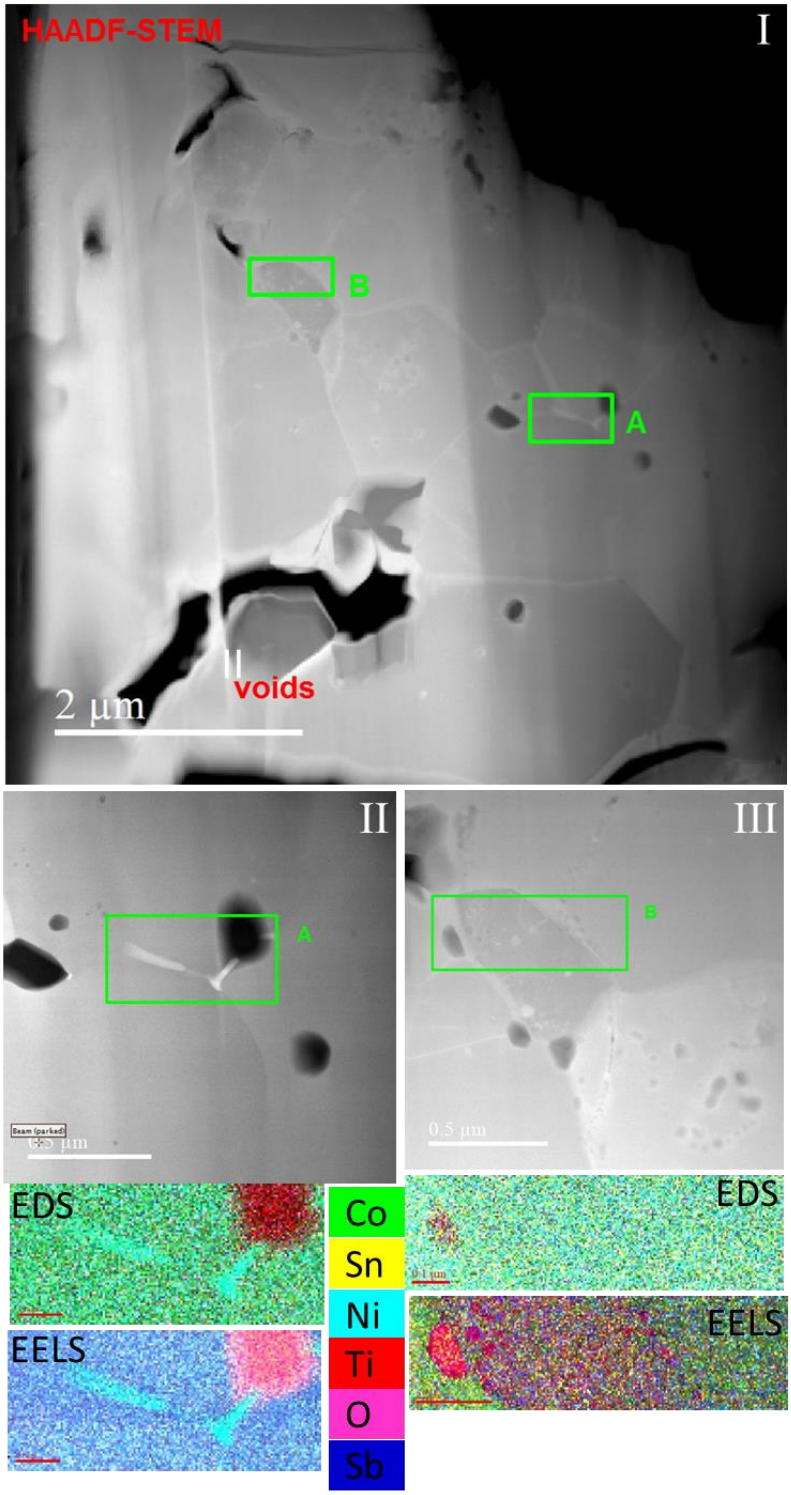

Figure 5.10. (I) is STEM image for the entire lamella and the regions of interest A and B for $(TiCoSb)_{0.85}(TiNi_2Sn)_{0.15}$ (II) is the STEM image and EDS/ EELS maps for the region A, while (III) is the STEM image and EDS/ EELS maps for the region B.

5.5.2. $TiCo_{0.9}Fe_{0.1}Sb_{0.9}Sn_{0.1}$

High magnification STEM image of the entire lamella (prepared by FIB-SEM) and the regions of interest is shown in Figure 5.11(I). This sample is also characterised with small grain sizes. Contrast variation between grains can be observed, which may be due to a compositional variation. No voids can be observed, as the sample has a relatively high density (93%). Figure 5.11(II) shows an STEM image and EELS maps for region (A), which contains both grain boundaries and small dark inclusion. The near vertical streaking seen in the STEM images is an artefact from the sample preparation by FIB-SEM. A variation in Ti concentration is seen between the grains. The small inclusion is found to be rich in Ti and O, suggesting the presence of Ti oxide. The absence of Sn in the elemental refers to the difficulty in resolving the Sn peak EELS spectrum. The STEM image and EELS maps of region B, which again contains both grain boundaries and a Ti oxide inclusion are presented in Figure 5.11(III). An increase in Ti at the grain boundary is obvious, along with a variation in Ti between grains. This analysis therefore suggests that the studied areas do not contain nanosegregated FH phase, which is in agreement with the result obtained from Rietveld analysis.

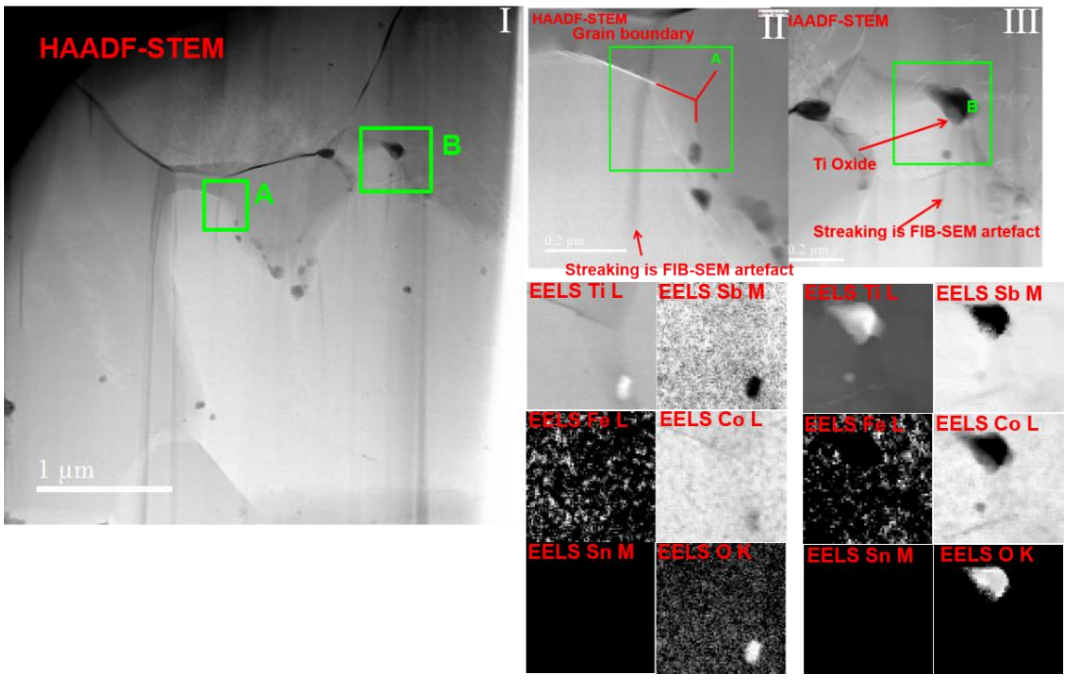

Figure 5.11. (I) is STEM image for the entire lamella and the regions of interest A and B for $(TiCoSb)_{0.9}(TiFe_2Sn)_{0.1}$. (II) is the STEM image and EELS maps for the region A, while (III) is the STEM image and EELS maps for the region B.

5.6. Electrical Property Measurements

Electrical property measurements were carried out initially on the preliminary series up to a maximum temperature of 723 K (Appendix 3, Figure 4). The results revealed interesting properties for the samples with M_2 = Fe_2 and Ni_2. Thereafter, transport property measurements were performed on each series individually.

5.6.1. $(TiCoSb)_{1-x}(TiNi_2Sn)_x$ (x = 0.05, 0.1, 0.15 and 0.2)

The temperature dependence of ρ, S and (S^2/ρ) for the $(TiCoSb_{1-x}(TiNi_2Sn)_x$ series is shown in Figure 5.12(a). For all samples, semiconductor – semimetal (degenerate semiconductor) transition is observed. $\rho(T)$ decreases with temperature to reach its minimum at about 550 K for the samples with x = 0.05 and 0.1, 512 K for the sample with x = 0.15 and 460 K for the sample with x = 0.2, after which it increases with temperature. In addition to that, ρ systematically decreases with increasing x value. All samples exhibit negative S values, indicating that the conduction is predominantly by electrons. For the samples with x = 0.05 and 0.1, the absolute value of S increases with increasing temperature. Meanwhile, it reaches its maximum at about 610 K for the samples with x = 0.15 and 0.2 and decrease with further increasing temperature. This may be due to the excitation of minority charge carriers across the band gap. A maximum S^2/ρ value of ~ 0.8 mW mK^{-2} was obtained for the sample with x = 0.1 at about 710 K. As previously discussed, Rietveld fits to neutron powder diffraction data for this series suggest that up to 16% of Ni substitutes to the Co site of the HH structure. The replacement of Co ($3d^7$) by Ni($3d^8$) will therefore electronically dope the p-type HH matrix (x% of Sn) and lead to n-type conduction. Sample with x = 0.1 has a maximum S^2/ρ of 0.8 mW m^{-1} K^{-2} at ~ 710 K. This is enabled by its large $S(T)$ and moderate $\rho(T)$ values. The other samples have relatively lower S^2/ρ values. The obvious downturn in S^2/ρ values for the x = 0.2 composition at about 600 K could be attributed to the excitation of minority charge carriers, which lead to a reduction in the absolute values of $S(T)$ and thus reducing the maximum S^2/ρ.

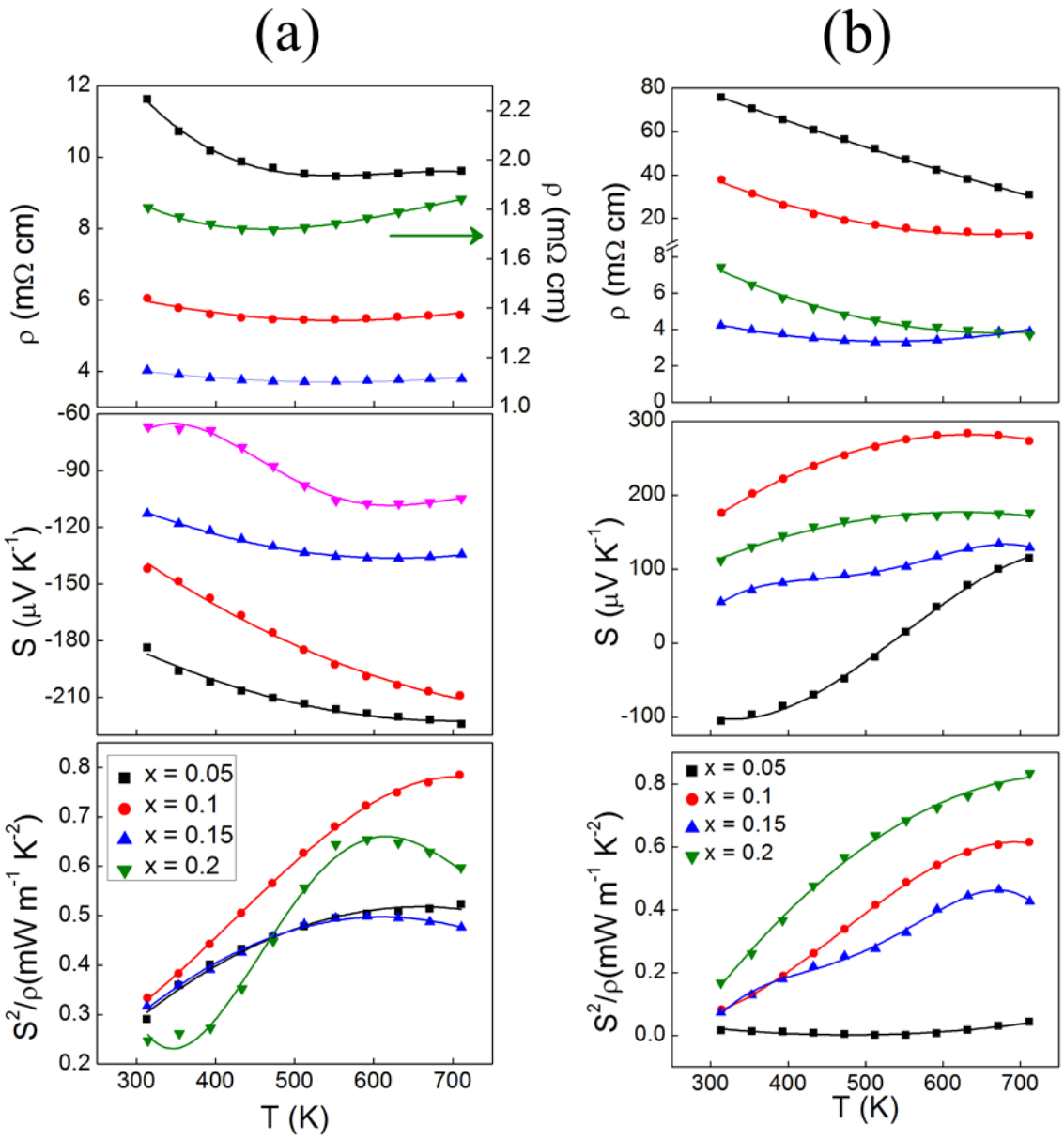

Figure 5.12. Temperature dependence of the electrical resistivity (ρ), Seebeck coefficient (S) and power factor (S^2/ρ) for a: $(TiCoSb)_{1-x}(TiNi_2Sn)_x$ and b: $(TiCoSb)_{1-x}(TiFe_2Sn)_x$ (x = 0.05, 0.1, 0.15, 0.2). Solid lies are a guide to the eye.

5.6.2. $(TiCoSb)_{1-x}(TiFe_2Sn)_x$ (x = 0.05, 0.1, 0.15 and 0,2)

It was not possible to determine the metal distribution of the elements over the crystallographic sites from Rietveld fits of the representative neutron data collected for all of these samples. However, transport property measurements revealed interesting properties for this series. The temperature dependence of the ρ, S and (S^2/ρ) for the ($TiCoSb_{1-x}(TiFe_2Sn)_x$ series is shown in Figure 5.12(b). $\rho(T)$ for the samples with x = 0.05, 0.1 and 0.2 decreases with increasing temperature, however, ρ for the x = 0.15 composition decreases with temperature to reach its minimum at about 550 K and increases with further increasing temperature. Moreover, ρ decreases remarkably with x increasing. At room temperature, a ρ value of ~ 80 mΩ cm is observed for the x = 0.05 sample, dropping to a value of ~ 4 mΩ cm for the x = 0.15 and 0.2 compositions. The x = 0.1, 0.15 and 0.2 samples exhibit p-type conduction in the measured temperature range, indicating that holes are predominant in the alloys. While, $S(T)$ shows a change from negative to positive values at about 540 K for the sample with x = 0.05. This n to p-type conversion is possibly caused by the increase of hole mobility at temperatures > 540 K. A maximum S^2/ρ value of ~ 0.8 mW m^{-1} K^{-2} is obtained for the sample with x = 0.2 at about 710 K.

5.6.3. $(TiCoSb)_{1-x}(TiCoNiSn)_x$ (x =0.1 and 0.2)

Structural analysis revealed that these samples consist of Ni-doped HH phases with Co-rich regions. The temperature dependence of ρ, S and S^2/ρ for the $(TiCoSb_{1-x}(TiCoNiSn)_x$ samples is presented in Figure 5.13a. $\rho(T)$ for both samples shows semiconducting behaviour, decreasing with increasing temperature. $\rho(T)$ values of the x = 0.2 samples are almost half of that for the x = 0.1 sample. At 300 K, a ρ value of ~ 12 mΩ cm is obtained for the x = 0.2 sample, compared to a value of ~ 24 mΩ cm for the x = 0.1 sample. All S values are negative, indicating that electrons are the majority charge carriers. A maximum $S(T)$ of ~ -190 μV k^{-1} at ~630 K is observed for the sample with x = 0.1. The absolute value of S decreases with increasing x from 0.1 to 0.2. The combination of moderate $\rho(T)$ and $S(T)$ values leads to S^2/ρ of 0.26 mW m^{-1} K^{-2} at 710 K for the x = 0.1 sample, compared to a value of 0.24 mW m^{-1} K^{-2} obtained for x = 0.2 at about 710 K.

5.6.4. $(TiCoSb)_{1-x}(TiCo_2Sn)_x$ (x =0.1 and 0.2).

These samples consist of a metal-rich HH matrix and a distinct $TiCo_2Sn$ FH phase. Figure 5.13b reveals the temperature dependence of ρ, S and S^2/ρ for these two samples over the investigated temperature range. $\rho(T)$ for both samples shows semiconducting behaviour. The x = 0.2 composition exhibited the lowest values of ρ, with a minimum value of ~ 10 mΩ cm at 712 K. The x = 0.1 sample shows relatively large and positive S with a maximum value of ~ + 137 μV/k at ~ 670 K. Meanwhile, n to p-type conversion is observed for the x = 0.2 composition at ~ 430 K. The calculation of the S^2/ρ indicates a maximum of 0.07 mW m^{-1} K^{-2} for the x = 0.1 sample.

5.6.5. $(TiCoSb)_{1-x}(Ti(FeCo)Sn)_x$ (x =0.1,0.2)

$\rho(T)$, $S(T)$ and S^2/ρ for this series is shown in Figure 5.13c. In both samples, ρ decreases with increasing temperature. A minimum ρ value of ~ 5 mΩ cm is obtained for the x = 0.2 sample at 712 K. Both samples show p-type semiconducting behaviour as indicated by the positive values of S. A maximum value of S of +248 μV K^{-1} is observed for the x = 0.1 composition at ~ 670 K. Analysis of the S^2/ρ indicates a maximum value of 0.19 mW m^{-1} K^{-2} for the x = 0.1 sample.

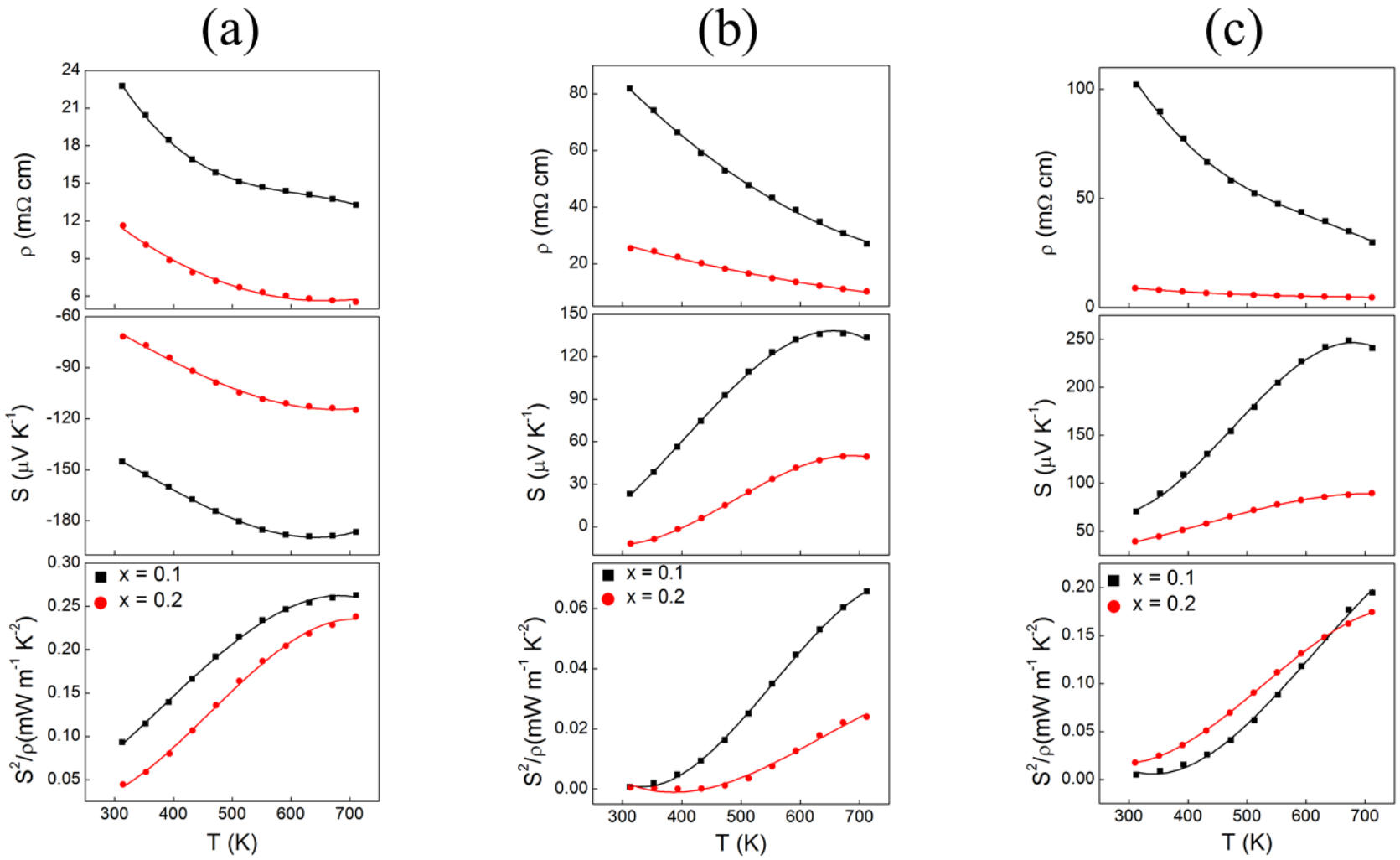

Figure 5.13. Temperature dependence of the electrical resistivity (ρ), Seebeck coefficient (S) and power factor S^2/ρ for a: $(TiCoSb)_{1-x}(Ti(CoNi)Sn)_x$, b: $(TiCoSb)_{1-x}(TiCo_2Sn)_x$ and c: $(TiCoSb)_{1-x}(Ti(FeCo)Sn)_x$ (x= 0.1, 0.2). Solid lines are a guide to the eye.

5.7. Thermal conductivity and Figure of Merit

Thermal diffusivity measurements were carried out on seven compositions. These only included samples with M_2 = Ni_2 and Fe_2.The temperature dependence of the total, κ, κ_{lat} and figure of merit *ZT* for the $(TiCoSb)_{1-x}(TiNi_2Sn)_x$ series is shown in Figure 5.14a. The x = 0.05 sample has the highest κ values over the measured temperature range. At 300 K, a κ value of 9.8 W m^{-1} K^{-1} is observed for the composition with x = 0.05, dropping to ~ 7.6 W m^{-1} K^{-1} for the x = 0.1 sample and ~ 6 W m^{-1} K^{-1} for the samples with x = 0.15 and 0.2. For all samples, as the temperature increases, κ decrease reaching a value of 5.5 W m^{-1} K^{-1} for the x = 0.05 sample at 728 K, 4.7 W m^{-1} K^{-1} at 718 for x = 0.1, 3.6 W m^{-1} K^{-1} at 728K for x = 0.15 and ~ 4.4 W m^{-1} K^{-1} at about 718 K. A similar behaviour is observed for κ_{lat}. At room temperature, more than 50 % reduction of κ_{lat} values can be observed for these samples as compared to TiCoSb (κ_{lat} = 18 W $m^{-1}K^{-1}$). [77] Samples with x = 0.15 and 0.2 attain very similar κ_{lat} values, indicating that the difference on their κ values could be attributed to a larger electronic contribution in the x = 0.2 sample, arising from its higher σ. *ZT* values for this series tend to increase with increasing temperature. A maximum *ZT* value of 0.12 is observed for the x = 0.1 composition at ~ 718 K. This modest value of *ZT* is consistent with literature on Ni-doped TiCoSb HH compounds. [76]

In the case of the $(TiCoSb)_{1-x}(TiFe_2Sn)_x$ series, diffusivity measurements were carried out on samples with x = 0.1, 0.15 and 0.2. The temperature dependence of κ, κ_{lat} and *ZT* is shown in Figure 5.14b. For all samples κ decreases with increasing temperature. The highest κ values are observed for the x = 0.1 composition. At ~ 300 K, κ decreases from ~ 8.5 W m^{-1} K^{-1} for x = 0.1 to a value of about 6 W m^{-1} K^{-1} for the x = 0.15 and 0.2 compositions. This corresponds to a 29 % reduction in κ values. The samples with x = 0.15 and 0.2 have similar κ_{lat} values. A peak ZT of ~ 0.13 is obtained for the sample with x = 0.2 at about 728 K. This value is comparable to values reported on p-type TiCoSb. [73,74,93]

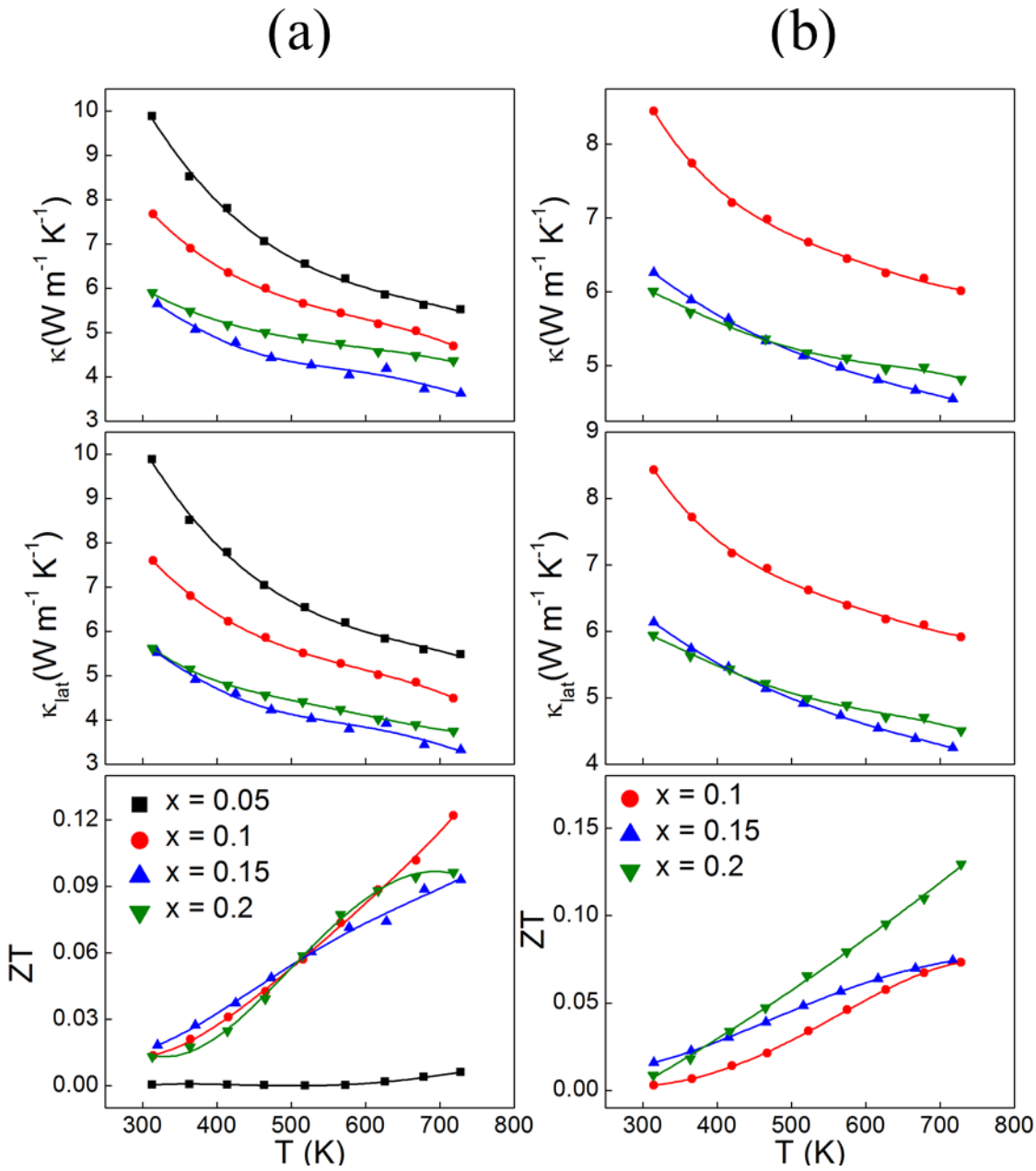

Figure 5.14. The temperature dependence of the total thermal conductivity, κ, lattice thermal conductivity, κ_{lat}, and figure of merit ZT for a: $(TiCoSb)_{1-x}(TiNi_2Sn)x$ and b: $(TiCoSb)_{1-x}(TiFe_2Sn)_x$.

5.8. Discussion

Herein, an investigation of the structure and properties of the $(TiCoSb)_{1-x}(TiM_2Sn)_x$ (M_2 = Fe_2, CoFe, Co_2, CoNi, Ni_2) nanocomposites prepared via solid state reaction, followed by hot pressing are reported. These systems are expected to segregate into a HH matrix with FH inclusions driven by high energy penalty resulting from destabilizing the 18-VEC HH structure. [133–135] PXRD analysis revealed that all of these compounds are pure, except for the occasional presence of very small amounts of minor impurities and/or the relevant FH phase. In addition, all peaks appeared to be sharp, no shoulders or peak splitting could be observed. Rietveld analysis of the NPD data for the $(TiCoSb)_{1-x}(TiNi_2Sn)_x$ (x =0.1, 0.15, 0.2) series revealed that for x = 0.1, the data can be fitted to a Ni-doped HH phase, while for $x \geq 0.15$ the data can be fitted using a mixture of Ni-doped HH and distinct $TiNi_2Sn$ FH phases. This clearly demonstrates that the nanosegregation of FH inclusions does not occur in this case and instead the excess Ni substitutes to the Co site of the HH structure. This conclusion was supported by TEM analysis, which did not revealed any obvious segregation, such as the spherically shaped inclusions or larger segregates reported on p-type XCoSb-based compounds. [92,94] Rietveld analysis of NPD data for the $(TiCoSb)_{1-x}(Ti(CoNi)Sn)_x$ (x = 0.1, 0.2) series demonstrated that the x = 0.1 composition consists of a metal-rich HH phase and that up to 7% of excess Co can be present on the vacant tetrahedral site. Meanwhile, the excess metal (CoNi) in the x = 0.2 sample is accommodated within the HH host and the distinct $Ti(Co,Ni)_2Sn$ FH phase. The fits also revealed that both samples have the same fitted HH composition (Table 5.8), and this result is supported by PXRD analysis, which revealed similar lattice parameters for these two samples (Table 5.3). In the case of the $(TiCoSb)_{1-x}(TiCo_2Sn)_x$ (x = 0.1, 0.2), Rietveld analysis suggested that the excess Co is divided over the HH and FH phases and thus the data could be fitted using a mixture of metal- rich HH and a distinct FH phase. Nevertheless, electron microscopy analysis of the M_2 = NiCo and Co_2 series is required to search for these possible nanoinclusions. The M_2 = Fe_2 and FeCo composites did not contain any peaks that could indicate the presence of a distinct FH phase. In addition, Rietveld analysis suggested that these two series do not contain any FH nanosegregation. This was confirmed on the $(TiCoSb)_{0.9}(TiFe_2Sn)_{0.1}$composition, in which TEM analysis did not reveal any obvious FH segregation. It was not yet possible to gain information on the metal distribution of the elements for the M_2 = Fe_2 and FeCo composites from Rietveld fits, thereby leading to difficulties in determining the structure-property relationship for these two series.

Electrical property measurements revealed n-type conduction for the M_2 = Ni_2 series. This is consistent with the replacement of Co ($3d^7$) by Ni ($3d^8$), which will electronically dope the p-type HH matrix and thus lead to negative S values. The effect of Ni doping on the transport properties of TiCoSb has been previously reported by two groups, [62,76] in which they observed a metallic behaviour for the $TiCo_{1-x}Ni_xSb$ series for $x \geq 0.05$, which was attributed to the formation of impurity band within the band gap. Meanwhile, the samples presented here exhibited semiconductor behaviour with a semiconductor-semimetal (degenerate semiconductor) transition observed at 550 K for x = 0.05 and shifts to lower temperatures with increasing x. This semiconducting behaviour may be due to the presence of Sn in the HH matrix which act as a hole dopant, compensating the electron doping by Ni and thus lead to an overall depletion of charge carriers. N-type conduction was also observed for the M_2 = CoNi series, which is in keeping with replacing Co with Ni. Whereas, the M_2 = Co_2 exhibited p-type behaviour, which may be due to the presence of x% Sn in the HH matrix. The HH phases of M_2 = CoNi and Co_2 series are predicted to be rich in Co and this should have an impact on the transport properties. It has been previously demonstrated that the presence of excess Ni in the in the $TiNi_{1+y}Sn$ composite leads to the formation of in-gap states, which in turn affects both $\rho(T)$ and $S(T)$. [91] Here, however, the impact of excess Co on transport properties requires further investigation, coupled with TEM analysis to probe structural feature of these materials. κ_{lat} values for both M_2 = Ni_2 and Fe are remarkably reduced, as compared to TiCoSb (κ_{lat} = 18 W m^{-1} K^{-1}) [77] Also, it is important here to mention that the formation of nanoinclusions as well as the degree of clustering depends sensitively on sample processing. For example, the $TiNi_{1+x}Sn$ composite prepared by solid state reaction favours the small clustering,[91] compared to lager segregates when prepared by synthesis protocol that proceed via a melt. [132] Furthermore, very promising properties have been reported for the $Zr_{0.25}Hf_{0.75}Ni_{1+x}Sn$ prepared by solid state reaction, ball milling and hot pressing. [89] Therefore it would be of great interest to investigate the integration of ball milling in the processing of the materials presented in this chapter.

Chapter 6-Conclusions

HH compounds based on XNiSn and XCoSb (X = Ti, Zr, Hf) are promising n- and p-type thermoelectric materials. [55,65] The unique crystal structure of HH compounds offers the possibility to optimise their thermoelectric properties through the chemical manipulation of the three filled sublattices. [64]. The best reported *ZT* values for n- and p-type are on the order *ZT* = 1 (for XNiSn) and *ZT* = 0.7 (for XCoSb), respectively. The aim of the work presented in this thesis is to identify other possible thermoelectric materials based on TiCoSb, which may lead to better performing compositions.

Three distinct sets of TiCoSb-based half Heuslers were prepared using solid state reactions. The first series investigates the solid solution between TiCoSb and the hypothetical HH VCoSn. For this purpose, a series of $Ti_{1-x}V_xCoSb_{1-x}Sn_x$ ($0 \leq x \leq 1$) compounds was prepared. Rietveld analysis of XRD data suggested the formation of solid solution up to x = 0.43. NPD and SEM analysis demonstrated that TiCoSb is stoichiometric, except for the incorporation of Ta along the grain edges due to reaction to the sample containment material. Moreover, NPD analysis confirmed the simultaneous substitutions of Ti by V and Sb by Sn for the x =0.3 sample. This study also provides a detailed investigation of the high-temperature stability of the $Ti_{1-x}V_xCoSb_{1-x}Sn_x$ alloys. Both TiCoSb and the V and Sn substituted samples show degradation after repeated measurements of their thermoelectric properties. The degradation is more pronounced for TiCoSb than for the V and Sn substituted samples. SEM-EDX analysis was carried on TiCoSb after the repeat measurements and confirmed the formation of amorphous TiO_2 and metallic CoSb, which was evident from post measurement analysis.

The aim of the second series was to p-type dope the V and Sn co-substituted samples by replacement of Co by Fe. A number of $Ti_{1-x}V_xCo_{1-y}Fe_ySb_{1-z}Sn_z$ compositions were prepared. In which, x, y and z were adjusted to achieve VEC = 17.85 in all samples. Surprisingly, electrical property measurements revealed unexpected n-type conduction for a subset of the samples. Structural analysis using diffraction showed that these samples are single phase, except for the occasional presence of FH phase and/or minority impurities. SEM-EDX analysis revealed the formation of Sn-rich full Heusler and alloy phases. P-type conduction was observed for the samples that do not contain Sn. This suggests that the unexpected n-type conduction may be caused by kinetic trapping of Sn caused by its low melting point. A test using arc-melting, revealed n- to

p-type transition with modest positive S values. This is in agreement with faster diffusion of Sn and Sb throughout the sample caused by the much faster nature of the melting process.

The third set of compounds reports on the synthesis, structure and properties of TiCoSb nanocomposites. Five series of $(TiCoSb)_{1-x}(TiM_2Sn)_x$ (M_2 = Fe_2, FeCo, Co_2, CoNi, Ni_2, $0.05 \leq x \leq 0.2$) were prepared. Laboratory XRD analysis revealed that these samples are pure, however, small amounts of the relevant FH TiM_2Sn phase and/or impurities were occasionally observed. Rietveld analysis of NPD revealed that the $(TiCoSb)_{1-x}(TiNi_2Sn)_x$ series consists of a Ni-doped HH phase, whereas the $(TiCoSb)_{1-x}(TiCoNiSn)_x$ and $(TiCoSb)_{1-x}(TiCo_2Sn)_x$ series can be fitted to a metal-rich HH and a distinct FH phases. For the $(TiCoSb)_{1-x}(TiFe_2Sn)_x$ and $(TiCoSb)_{1-x}(TiFeCoSn)_x$, Rietveld fits to NPD data led to unsatisfactory conclusions, making the determination of structure-property relations for these two series not possible. The $(TiCoSb)_{1-x}(TiNi_2Sn)_x$ and $(TiCoSb)_{1-x}(TiFe_2Sn)_x$ show very promising thermoelectric properties and are of interest for further investigation.

Future Work

All the series investigated in this thesis are new and provide novel contribution to the literature on TiCoSb-based HH compounds. With regard to the samples presented in chapter 4, it would be useful to investigate other phonon scattering mechanisms that led to the reduction of the lattice thermal conductivity. Also, TEM analysis may be beneficial in providing further insight into the structure of this sample. In the case of the sample presented in Chapter 5, determination of the metal distribution in the M_2 = Fe_2 and Co_2 samples will allow the structure-property relationships to be established and this requires further investigation of different structural models to fit neutron data. Furthermore, SEM-EDX analysis on the $(TiCoSb)_{1-x}(TiM_2Sn)_x$ series would be important to further probe the microstructure and compositional homogeneity of these samples. Also, it would be of high interest to investigate the integration of ball-milling in processing of these samples, as this technique is widely used in the preparation of nanocomposites HH materials and has led to significant advances in *ZT*.

References

1 R. E. Smalley, *MRS Bull.*, 2005, **30**, 412–417.

2 G. H. O. Edenhofer, R. Pichs-Madruga, Y. Sokona, K. Seyboth, P. Matschoss, S. Kadner, T. Zwickel, P. Eickemeier and C. von S. (eds S. Schlömer, *IPCC Special Report on Renewable Energy Sources and Climate Change Mitigation*, 2011.

3 A. J. Minnich, M. S. Dresselhaus, Z. F. Ren and G. Chen, 2009, 466–479.

4 P. D.-C. Martín-gonzález, Marisol, O.Caballero-Calero, 2013, **24**, 288–305.

5 S. Kumar, S. D. Heister, X. Xu, J. R. Salvador and G. P. Meisner, *J. Electron. Mater.*, 2013, **42**, 665–674.

6 Y. Ammar, S. Joyce, R. Norman, Y. Wang and A. P. Roskilly, *Appl. Energy*, 2012, **89**, 3–20.

7 T. M. Tritt, H. Böttner and L. Chen, *MRS Bull.*, 2008, **33**, 366–368.

8 S. K. Bux, J.-P. Fleurial and R. B. Kaner, *Chem. Commun.*, 2010, **46**, 8311–8324.

9 J.-P. Fleurial, *JOM*, 2009, **61**, 79–85.

10 W. Luan and S. Tu, *Chinese Sci. Bull.*, 2004, **49**, 1212–1219.

11 T. M. Tritt, *Encycl. Mater. Sci. Technol.*, 2002, 1–11.

12 H. J. Goldsmid, *Introduction to thermoelectricity*, Springer, 2010.

13 A.K. Cheetham and P. Day., Ed., *Solid state chemistry : techniques*, Oxford University Press, Oxfors, 1987.

14 S. B. Riffat and X. Ma, *Appl. Therm. Eng.*, 2003, **23**, 913–935.

15 D. M. Rowe, *Thermoelectrics handbook : macro to nano*, CRC/Taylor & Francis, 2006.

16 L. E. Bell, *Science*, 2008, **321**, 1457–61.

17 E. Altenkirch, *Phys. Zeitschrift*, 1911, **12**, 920–924.

18 J. R. Sootsman, D. Y. Chung and M. G. Kanatzidis, *Angew. Chemie - Int. Ed.*, 2009, **48**, 8616–8639.

19 J.-C. Zheng, *Front. Phys. China*, 2011, **3**, 12.

20 J.-C. Zheng, *Front. Phys. China*, 2011, **3**, 12.

21 H. J. Goldsmid and J. W. Sharp, *J. Electron. Mater.*, 1999, **28**, 869–872.

22 J. P. Heremans, V. Jovovic, E. S. Toberer, A. Saramat, K. Kurosaki, A. Charoenphakdee, S. Yamanaka and G. J. Snyder, *Science.*, 2008, **321**, 554–557.

23 F. J. DiSalvo, 1999, **285**, 703–706.

24 G. Tan, L. D. Zhao and M. G. Kanatzidis, *Chem. Rev.*, 2016, **116**, 12123–12149.

25 H. Muta, T. Kanemitsu, K. Kurosaki and S. Yamanaka, *J. Alloys Compd.*, 2009, **469**, 50–55.

26 E. S. Toberer, A. Zevalkink and G. J. Snyder, *J. Mater. Chem.*, 2011, **21**, 15843.

27 P.G. Klemens and M. Gell, *Mater. Sci. Eng.*, 1998, **A245**, 143–149.

28 C. B. Vining, W. Laskow, J. O. Hanson, R. R. Van der Beck and P. D. Gorsuch, *J. Appl. Phys.*, 1991, **69**, 4333.

29 C. J. Vineis, A. Shakouri, A. Majumdar and M. G. Kanatzidis, *Adv. Mater.*, 2010, **22**, 3970–3980.

30 A. R. West, *Basic solid state chemistry*, John Wiley & Sons, 2nd edn., 2000.

31 A. Rockett, *The Materials Science of Semiconductors*, Springer US, Boston, MA, 2008.

32 L. Smart and E. Moore, *Solid state chemistry : an introduction*, Taylor and Francis, 3rd edn., 2005.

33 Y. Pei, H. Wang and G. J. Snyder, *Adv. Mater.*, 2012, **24**, 6125–6135.

34 E. Environ, Y. Pei, A. D. Lalonde, H. Wang and G. J. Snyder, 2012, 7963–7969.

35 W. Liu, X. Tan, K. Yin, H. Liu, X. Tang, J. Shi, Q. Zhang and C. Uher, *Phys. Rev. Lett.*, 2012, **108**, 1–5.

36 L. D. Hicks and M. S. Dresselhaus, *Phys. Rev. B*, 1993, **47**, 12727–12731.

37 M. S. Dresselhaus, G. Chen, M. Y. Tang, R. Yang, H. Lee, D. Wang, Z. Ren, J. P. Fleurial and P. Gogna, *Adv. Mater.*, 2007, **19**, 1043–1053.

38 R. Venkatasubramanian, E. Siivola, T. Colpitts and B. O'Quinn, *Nature*, 2001, **413**, 597–602.

39 Y.-M. Lin, S. B. Cronin, J. Y. Ying, M. S. Dresselhaus and J. P. Heremans, *Appl. Phys. Lett.*, 2000, **76**, 3944.

40 T. C. Harman, P. J. Taylor, M. P. Walsh and B. E. LaForge, *Science.*, 2002, **297**.

41 F. D. Rosi, B. Abeles and R. V. Jensen, *J. Phys. Chem. Solids*, 1959, **10**, 191–200.

42 C. Wood, *Inst. Phys.*, 1988, **51**, 459–539.

43 G. Slack, in *CRC Handbook of Thermoelectrics*, CRC Press, 1995.

44 J. L. Cohn, G. S. Nolas, V. Fessatidis, T. H. Metcalf and G. a. Slack, *Phys. Rev. Lett.*, 1998, **82**, 779.

45 G. S. Nolas, G. Fowler and J. Yang, *J. Appl. Phys.*, 2006, **100**, 43705.

46 H. Goldsmid, *Thermoelectric refrigeration*, Plenum Press, New York, 1964.

47 Y. I. Ravich, B. A. Efimova and I. A. Smirnov, in *Semiconducting Lead Chalcogenides*, Springer US, Boston, MA, 1970, pp. 323–346.

48 E. Skrabek and D. Trimmer, in *CRC Handbook of Thermoelectrics*, CRC Press, 1995.

49 G. J. Snyder and E. S. Toberer, *Nat. Mater.*, 2008, **7**, 105–114.

50 J. P. Dismukes, L. Ekstrom, E. F. Steigmeier, I. Kudman and D. S. Beers, *J. Appl. Phys.*, 1964, **35**, 2899.

51 X. Tang, Q. Zhang, L. Chen, T. Goto and T. Hirai, *J. Appl. Phys.*, 2005, **97**, 93712.

52 G. S. Nolas, J. L. Cohn, G. A. Slack and S. B, *Phys. Lett.*, 1998, **73178**, 178–180.

53 X. W. Wang, H. Lee, Y. C. Lan, G. H. Zhu, G. Joshi, D. Z. Wang, J. Yang, A. J. Muto, M. Y. Tang, J. Klatsky, S. Song, M. S. Dresselhaus, G. Chen and Z. F. Ren, *Appl. Phys. Lett.*, 2008, **93**, 19–21.

54 J. Androulakis, K. F. Hsu, R. Pcionek, H. Kong, C. Uher, J. J. D'Angelo, A. Downey, T. Hogan and M. G. Kanatzidis, *Adv. Mater.*, 2006, **18**, 1170–1173.

55 T. Graf, C. Felser and S. S. P. Parkin, *Prog. Solid State Chem.*, 2011, **39**, 1–50.

56 H. C. Kandpal, C. Felser and R. Seshadri, *J. Phys. D. Appl. Phys.*, 2006, **39**, 776–

785.

57 D. Jung, H. J. Koo and M. H. Whangbo, *J. Mol. Struct. THEOCHEM*, 2000, **527**, 113–119.

58 S. Sakurada and N. Shutoh, *Appl. Phys. Lett.*, 2005, **86**, 1–3.

59 J. Toboła and J. Pierre, *J. Alloy. Comp.*, 2000, **296**, 243–252.

60 S. Öğüt and K. M. Rabe, *Phys. Rev. B*, 1995, **51**, 10443–10453.

61 T. Graf, S. S. P. Parkin and C. Felser, *IEEE Trans. Magn.*, 2011, **47**, 367–373.

62 Y. Stadnyk, V. A. Romaka, M. Shelyapina, Y. Gorelenko, L. Romaka, D. Fruchart, A. Tkachuk and V. Chekurin, *J. Alloys Compd.*, 2006, **421**, 19–23.

63 L. Offernes, P. Ravindran and A. Kjekshus, *J. Alloys Compd.*, 2007, **439**, 37–54.

64 S. Chen and Z. Ren, *Mater. Today*, 2013, **16**, 387–395.

65 J.-W. G. Bos and R. A. Downie, *J. Phys. Condens. Matter*, 2014, **26**, 433201.

66 W. Xie, A. Weidenkaff, X. Tang, Q. Zhang, J. Poon and T. Tritt, *Nanomaterials*, 2012, **2**, 379–412.

67 Q. Shen, L. Chen, T. Goto, T. Hirai, J. Yang, G. P. Meisner and C. Uher, *Appl. Phys. Lett.*, 2001, **79**, 4165.

68 J. Tobola, J. Pierre, S. Kaprzyk, R. V Skolozdra and M. A. Kouacou, *J. Phys. Condens. Matter*, 1998, **10**, 1013–1032.

69 K. Bartholomé, B. Balke, D. Zuckermann, M. Köhne, M. Müller, K. Tarantik and J. König, *J. Electron. Mater.*, 2014, **43**, 1775–1781.

70 J. Krez, B. Balke, C. Felser, W. Hermes and M. Schwind, 1–10.

71 J. Barth, B. Balke, G. H. Fecher, H. Stryhanyuk, A. Gloskovskii, S. Naghavi and C. Felser, *J. Phys. D. Appl. Phys.*, 2009, **42**, 185401.

72 Y. Kimura, H. Ueno and Y. Mishima, *J. Electron. Mater.*, 2009, **38**, 934–939.

73 T. Sekimoto, K. Kurosaki, H. Muta and S. Yamanaka, *J. Alloys Compd.*, 2006, **407**, 326–329.

74 T. Wu, W. Jiang, X. Li, Y. Zhou and L. Chen, *J. Appl. Phys.*, 2007, **102**.

75 M. Zhou, L. Chen, C. Feng, D. Wang and J. F. Li, *J. Appl. Phys.*, 2007, **101**, 113714.

76 M. Zhou, C. Feng, L. Chen and X. Huang, *J. Alloys Compd.*, 2005, **391**, 194–197.

77 M. Zhou, L. Chen, W. Zhang and C. Feng, *J. Appl. Phys.*, 2005, **98**, 14–19.

78 W. Xie, Q. Jin and X. Tang, *J. Appl. Phys.*, 2008, **103**, 43711.

79 S. R. Culp, J. W. Simonson, S. J. Poon, V. Ponnambalam, J. Edwards and T. M. Tritt, *Appl. Phys. Lett.*, 2008, **93**, 2006–2009.

80 H. Reith, K. Nielsch, J. M. Mena, H. G. Schoberth, T. Gruhn and H. Emmerich, *Phys. Status Solidi Appl. Mater. Sci.*, 2016, **213**, 706–715.

81 A. Page, A. Van der Ven, P. F. P. Poudeu and C. Uher, *J. Mater. Chem. A*, 2016, **4**, 13949–13956.

82 H. Jones, *J. Mater. Sci.*, 1984, **19**, 1043–1076.

83 E. Rausch, B. Balke, T. Deschauer, S. Ouardi and C. Felser, *APL Mater.*, 2015, **3**, 0–8.

84 M. Schwall and B. Balke, *Phys. Chem. Chem. Phys.*, 2013, **15**, 1868–1872.

85 E. Rausch, B. Balke, S. Ouardi and C. Felser, *Phys. Chem. Chem. Phys.*, 2014, **16**, 25258–62.

86 J. Krez, B. Balke, C. Felser, W. Hermes and M. Schwind, *Phys. Chem. Chem. Phys.*, 2015, **17**, 1–10.

87 G. Joshi, X. Yan, H. Wang, W. Liu, G. Chen and Z. Ren, *Adv. Energy Mater.*, 2011, **1**, 643–647.

88 X. Yan, W. Liu, S. Chen, H. Wang, Q. Zhang, G. Chen and Z. Ren, *Adv. Energy Mater.*, 2013, **3**, 1195–1200.

89 J. P. A. Makongo, D. K. Misra, X. Zhou, A. Pant, M. R. Shabetai, X. Su, C. Uher, K. L. Stokes and P. F. P. Poudeu, *J. Am. Chem. Soc.*, 2011, **133**, 18843–18852.

90 C. S. Birkel, J. E. Douglas, B. R. Lettiere, G. Seward, N. Verma, Y. Zhang, T. M. Pollock, R. Seshadri and G. D. Stucky, *Phys. Chem. Chem. Phys.*, 2013, **15**,

6990–7.

91 R. A. Downie, R. I. Smith, D. A. Maclaren and J. W. G. Bos, *Chem. Mater.*, 2015, **27**, 2449–2459.

92 P. Sahoo, Y. Liu, J. P. a Makongo, X.-L. Su, S. J. Kim, N. Takas, H. Chi, C. Uher, X. Pan and P. F. P. Poudeu, *Nanoscale*, 2013, **5**, 9419–9427.

93 W. J. Xie, Y. G. Yan, S. Zhu, M. Zhou, S. Populoh, K. Gałązka, S. J. Poon, A. Weidenkaff, J. He, X. F. Tang and T. M. Tritt, *Acta Mater.*, 2013, **61**, 2087–2094.

94 W. J. Xie, J. He, S. Zhu, X. L. Su, S. Y. Wang, T. Holgate, J. W. Graff, V. Ponnambalam, S. J. Poon, X. F. Tang, Q. J. Zhang and T. M. Tritt, *Acta Mater.*, 2010, **58**, 4705–4713.

95 A. R. West, *Solid state chemistry and Its Applications*, John Wiley & Sons, Chichester, 1987.

96 W. Clegg, *Crystal structure determination*, Oxford University Press, 1998.

97 D. McKie and C. McKie, *Essentials of Crystallography*, Blackwell Scientific Publications, 1986.

98 C. Hammond, *The Basics of Crystallography and Diffraction*, Oxford University Press Inc, New York, 2nd edn., 2001.

99 S. M. Bennington, R. . Smith and A. . Hannon, *ISIS Neutron Training Course Booklet*, ISIS, STFC, Harwell, 2012.

100 E. H. Kisi and C. J. Howard, *Applications of neutron powder diffraction*, Oxford University Press, 2012.

101 *http://www.isis.stfc.ac.uk/instruments/polaris/*.

102 L. B. Mccusker, R. B. Von Dreele, D. E. Cox, D. Loue È R D and P. Scardi, *Int. Union Crystallogr. J. Appl. Crystallogr. J. Appl. Cryst*, 1999, **32**, 36–50.

103 R. A. Young, *The Rietveld method*, Oxford University Press, Oxford, 1993.

104 A. C. Larson and R. B. Von Dreele, 2000.

105 B. H. Toby, *J. Appl. Cryst*, 2001, **34**, 210–213.

106 A.K. Cheetham and P. Day., Ed., *Solid state chemistry : techniques*, Oxford

University Press, Oxfors, 1987.

107 T. G. Rochow and P. A. Tucker, *Introduction to microscopy by means of light, electrons, X rays, or acoustics*, Plenum Press, New York, 2nd edn., 1994.

108 P. S. Gaal, M.-A. Thermitus and D. E. Stroe, *J. Therm. Anal. Calorim.*, 2004, **78**, 185–189.

109 C. Uher and D. Morelli, *Thermal conductivity 25 : thermal expansion 13 : joint conferences, June 13-16, 1999, Ann Arbor, Michigan, USA*, CRC Press, 2000.

110 M. Hichour, D. Rached, R. Khenata, M. Rabah, M. Merabet, A. H. Reshak, S. Bin Omran and R. Ahmed, *J. Phys. Chem. Solids*, 2012, **73**, 975–981.

111 M. Ameri, A. Touia, R. Khenata, Y. Al-Douri and H. Baltache, *Optik.*, 2013, **124**, 570–574.

112 C. S. Lue, Y. Öner, D. G. Naugle and J. H. Ross, *IEEE Trans. Magn.*, 2001, **37**, 2138–2140.

113 Y. Xia, V. Ponnambalam, S. Bhattacharya, a L. Pope, S. J. Poon and T. M. Tritt, *J. Phys. Condens. Matter*, 2000, **13**, 77–89.

114 S. Ouardi, G. H. Fecher, C. Felser, M. Schwall, S. S. Naghavi, A. Gloskovskii, B. Balke, J. Hamrle, K. Postava, J. Piatora, S. Ueda and K. Kobayashi, *Phys. Rev. B - Condens. Matter Mater. Phys.*, 2012, **86**, 14–17.

115 T. Sekimoto, K. Kurosaki, H. Muta and S. Yamanaka, *J. Alloys Compd.*, 2005, **394**, 122–125.

116 I. Skovsen, L. Bjerg, M. Christensen, E. Nishibori, B. Balke, C. Felser and B. B. Iversen, *Dalt. Trans.*, 2010, **39**, 10154–10159.

117 E. Rausch, B. Balke, S. Ouardi and C. Felser, *Energy Technol.*, 2015, **3**, 1217–1224.

118 J. C. Slater, *J. Chem. Phys.*, 1964, **41**, 3199.

119 R. A. Downie, D. A. MacLaren, R. I. Smith and J. W. G. Bos, *Chem. Commun.*, 2013, **49**, 4184.

120 R. Gautier, X. Zhang, L. Hu, L. Yu, Y. Lin, S. O. L., D. Chon, K. R. Poeppelmeier and A. Zunger, *Nat Chem*, 2015, **7**, 308–316.

121 J. E. Douglas, C. S. Birkel, N. Verma, V. M. Miller, M.-S. Miao, G. D. Stucky, T. M. Pollock and R. Seshadri, *J. Appl. Phys.*, 2014, **115**, 43720.

122 X. Yan, G. Joshi, W. Liu, Y. Lan, H. Wang, S. Lee, J. W. Simonson, S. J. Poon, T. M. Tritt, G. Chen and Z. F. Ren, *Nano Lett.*, 2011, **11**, 556–560.

123 E. Rausch, M. V. Castegnaro, F. Bernardi, M. C. Martins Alves, J. Morais and B. Balke, *Acta Mater.*, 2016, **115**, 308–313.

124 H. Muta, T. Kanemitsu, K. Kurosaki and S. Yamanaka, 2006, **47**, 1453–1457.

125 R. Downie, S. Popuri, H. Ning, M. Reece and J.-W. Bos, *Materials.*, 2014, **7**, 7093–7104.

126 J. Schmitt, Z. M. Gibbs, G. J. Snyder and C. Felser, *Mater. Horiz.*, 2015, **2**, 68–75.

127 A. Petersen, S. Bhattacharya, T. M. Tritt and S. J. Poon, *J. Appl. Phys.*, 2015, **117**.

128 T. Sekimoto, K. Kurosaki, H. Muta and S. Yamanaka, *Mater. Trans.*, 2006, **47**, 1445–1448.

129 J. Yang, G. P. Meisner and L. Chen, *Appl. Phys. Lett.*, 2004, **85**, 1140–1142.

130 H. Hazama, M. Matsubara, R. Asahi and T. Takeuchi, *J. Appl. Phys.*, 2011, **110**.

131 Y. Wang Chai and Y. Kimura, *Appl. Phys. Lett.*, 2012, **100**.

132 J. E. Douglas, C. S. Birkel, M.-S. Miao, C. J. Torbet, G. D. Stucky, T. M. Pollock and R. Seshadri, *Appl. Phys. Lett.*, 2012, **101**, 183902.

133 K. Kirievsky, M. Shlimovich, D. Fuks and Y. Gelbstein, *Phys. Chem. Chem. Phys.*, 2014, **16**, 20023–20029.

134 J. E. Douglas, P. A. Chater, C. M. Brown, T. M. Pollock and R. Seshadri, *J. Appl. Phys.*, 2014, **116**, 163514.

135 K. Kirievsky, Y. Gelbstein and D. Fuks, *J. Solid State Chem.*, 2013, **203**, 247–254.

Appendix 1

Rietveld refinement results, X-ray diffraction data and electrical property measurements for the preliminary cold – pressed $Ti_{1-x}V_xCoSb_{1-x}Sn_x$ series, referred to in Chapter 3, are provided in this appendix.

Table 1. Lattice parameters, densities and percentage densities for the preliminary cold-pressed $Ti_{1-x}V_xCoSb_{1-x}Sn_x$ series. No solid pellets were obtained for the x = 0.125 and x $\geq$ 0.625

x	a_{HH} (Å)	Density (g cm^{-3})	Density (%)
0	5.8825(1)	5.22	69.9
0.125	5.8779(1)	-	-
0.25	5.8743(1)	5.30	70.7
0.375	5.8692(1)	5.46	72.6
0.5	5.8680(3)	5.65	75.2
0.625	5.8672(3)	-	-
0.75	5.8691(2)	-	-
1	-	-	-

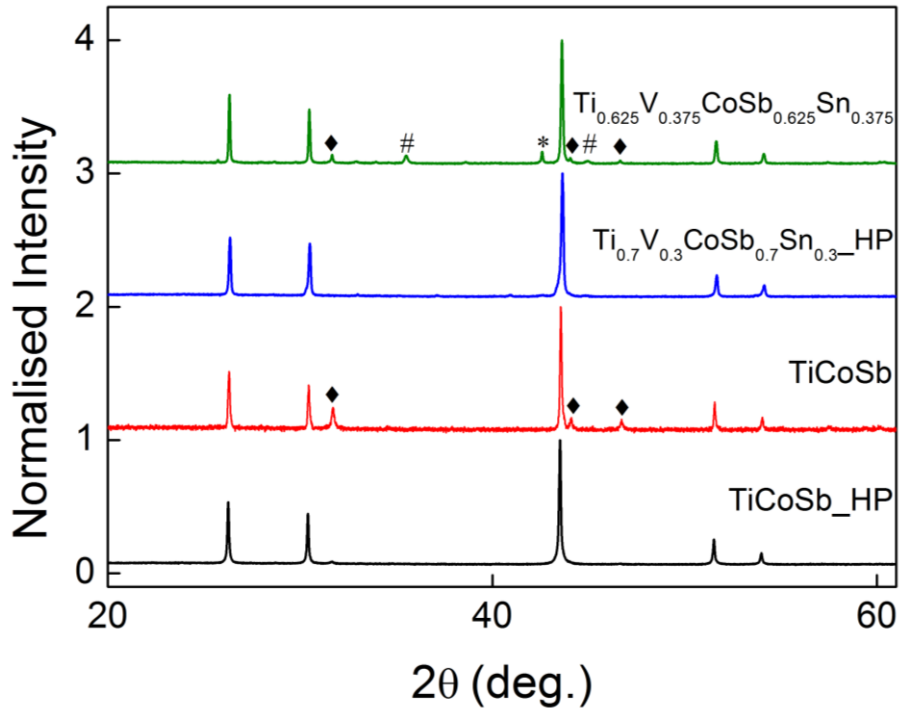

Figure 1. X-ray powder diffraction patterns for hot - and cold - pressed TiCoSb, hot-pressed $Ti_{0.7}V_{0.3}CoSb_{0.7}Sn_{0.3}$ and cold-pressed $Ti_{0.625}V_{0.375}CoSb_{0.625}Sn_{0.375}$ after repeat thermoelectric property measurements. (Data have been normalised and offset by 1; ♦: CoSb, *: VCo_2Sn, #: $CoSn_2$).

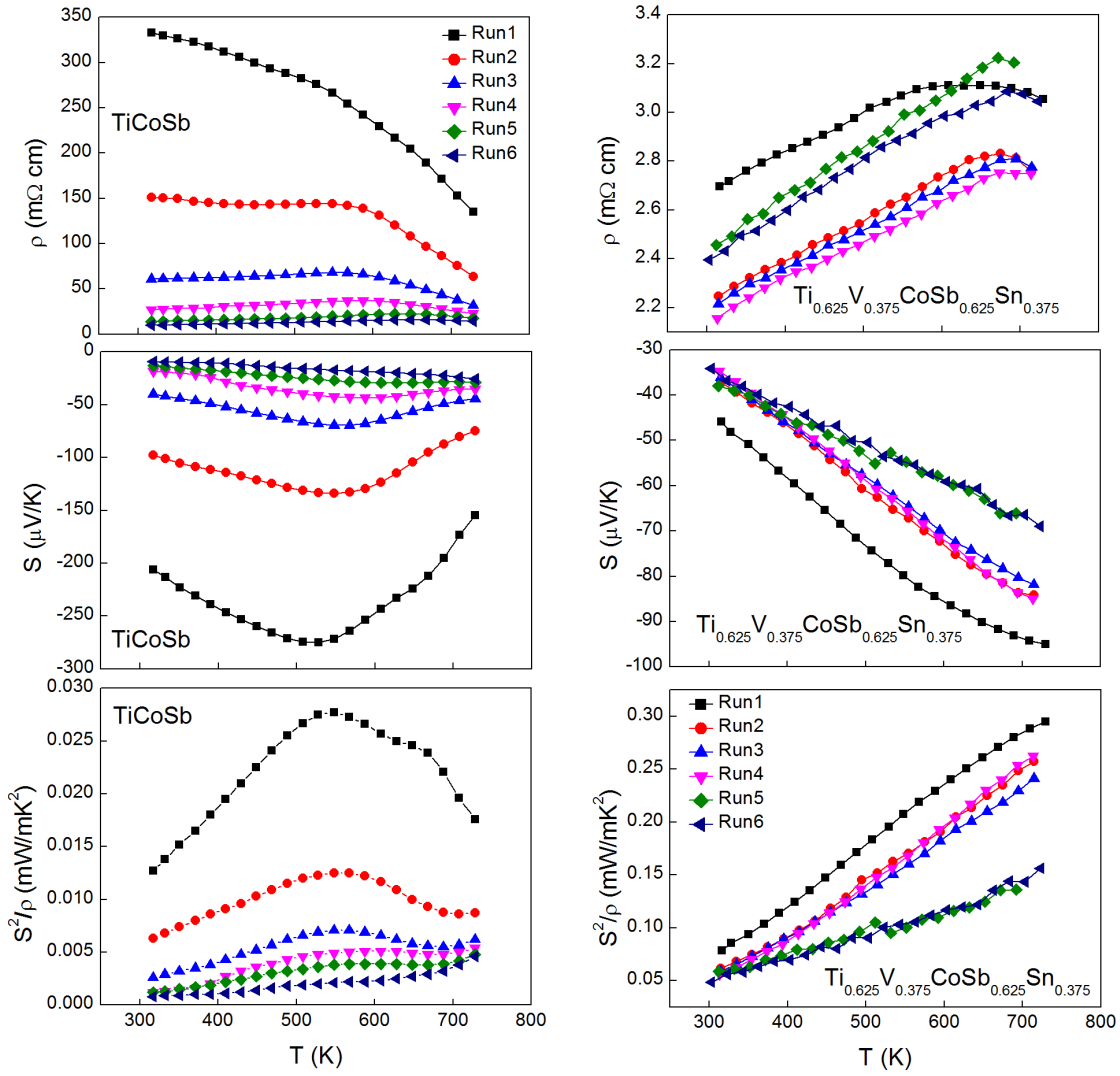

Figure 2. Repeatability tests of the electrical resistivity (ρ), Seebeck coefficient (S), and thermoelectric power factor (S^2/ρ) for cold - pressed TiCoSb and $Ti_{0.625}V_{0.375}CoSb_{0.625}Sn_{0.375}$.

Appendix 2

Low magnification (5000 ×) SEM backscattered electron, EDX layered images and elemental maps of the surface of samples B and C discussed in Chapter 4.

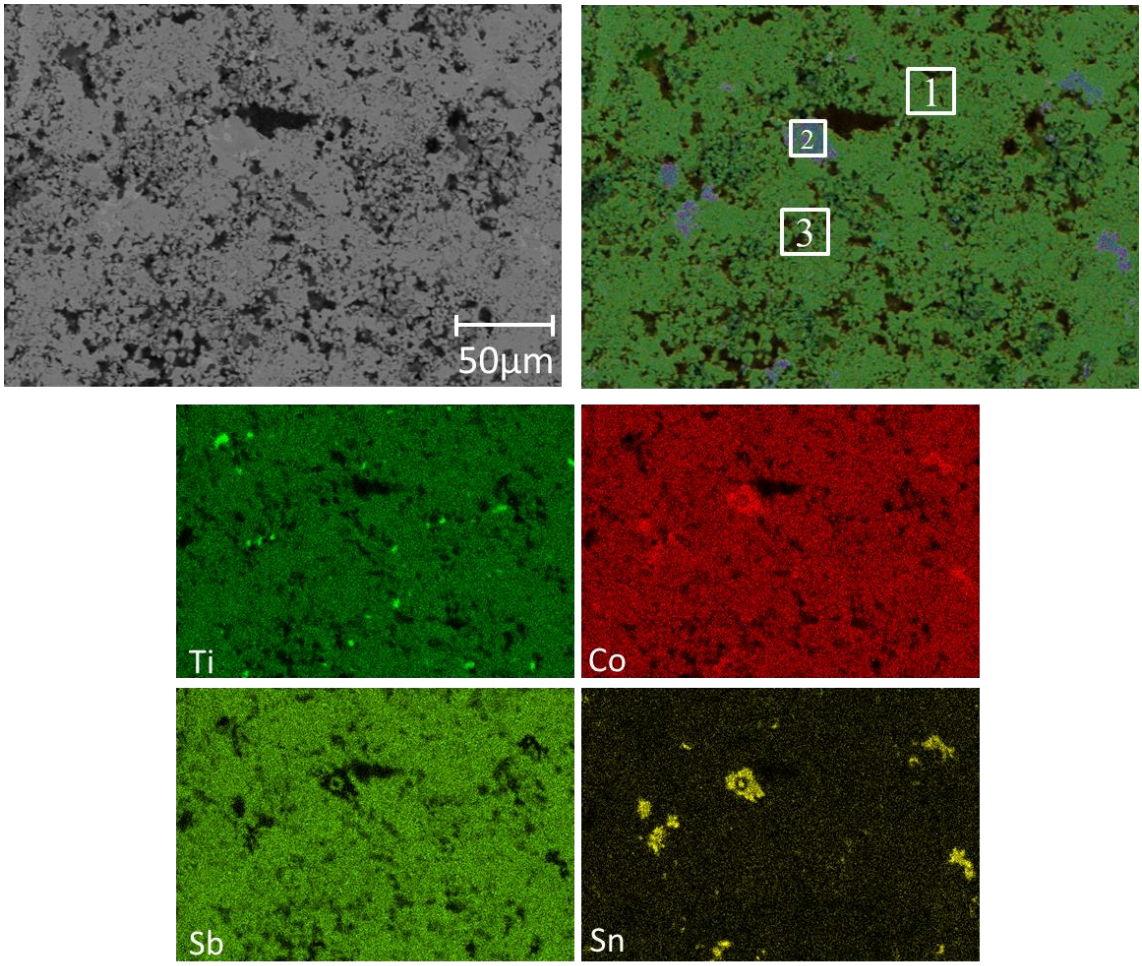

Figure 1. SEM backscattered electron, EDX layered images and elemental maps for $TiCoSb_{0.85}Sn_{0.15}$ (sample B). The experimental compositions of regions 1, 2 and 3 are: TiCoSb, $TiCo_{1.7}Sn$ and $TiCoSb_{0.96}Sn_{0.04}$, respectively. The average chemical composition of the whole map is $TiCoSb_{0.93}Sn_{0.07}$ with VEC = 17.93. The sample contains traces of elemental Ti, which is also observed in neutron powder diffraction but difficult to detect in laboratory X-ray diffraction.

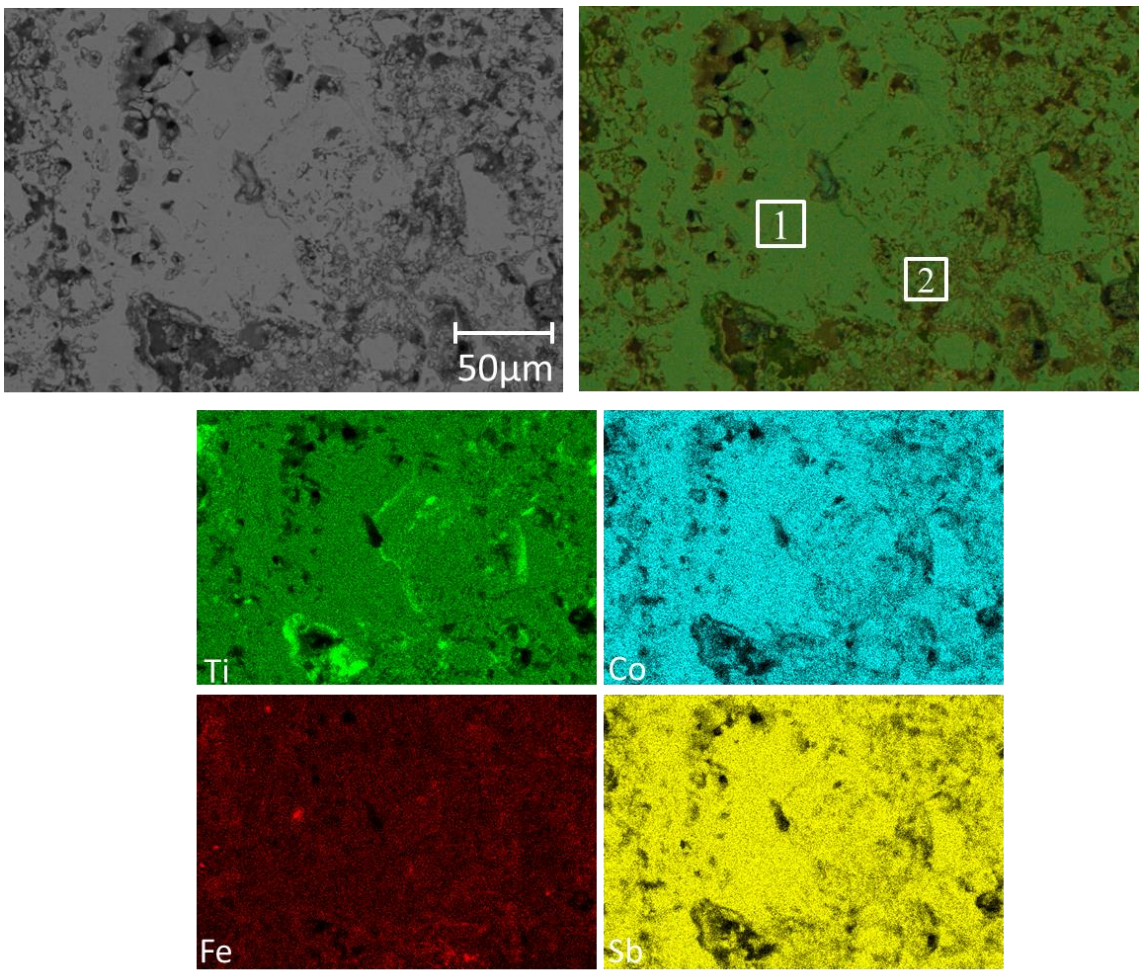

Figure 1. SEM backscattered electron, EDX layered images and elemental maps for $TiCo_{0.85}Fe_{0.15}Sb$ (sample C). The experimental compositions of regions 1 and 2 are: $TiCo_{0.92}Fe_{0.08}Sb$ and $TiCo_{0.84}Fe_{0.16}Sb$, respectively. The average chemical composition of the whole layer is $TiCo_{0.88}Fe_{0.12}Sb$ with VEC = 17.88.

Appendix 3

Rietveld fits to neutron powder diffraction data collected for $TiCoSb_{0.9}Sn_{0.1}$, $(TiCoSb)_{1-x}(TiFe_2Sn)_x$ (x= 0.1, 0.15, 0.2) and $(TiCoSb)_{1-x}(Ti(FeCo)Sn)_x$ (x= 0.1, 0.2), referred to in Chapter 5 are provided in this appendix. In addition to this, temperature dependence of the electrical resistivity (ρ), Seebeck coefficient (S) and power factor (S^2/ρ) for the preliminary series $(TiCoSb)_{0.9}(TiM_2Sn)_{0.1}$ is also provided here.

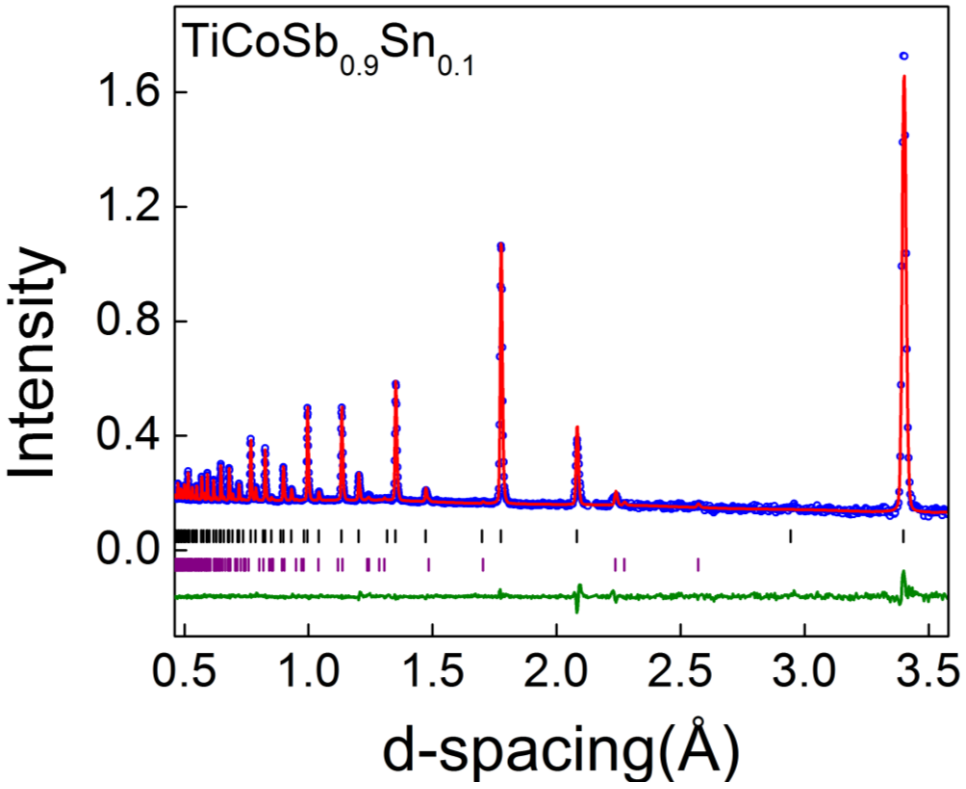

Figure 1. Rietveld refinement to neutron powder diffraction data collected for $TiCoSb_{0.9}Sn_{0.1}$. Blue circles represent the collected data, red line is the calculated data and the green line is the difference. Black tickmarks are for the half Heusler phase and purple tickmarks are for Ti. Data shown are from detector bank 4.

Table 1. Lattice parameters (a), weight percentages, thermal displacement parameters (U_{iso}/Å^2), fractional occupancies and fit statistics for Rietveld refinement of neutron powder diffraction data collected for the $(TiCoSb)_{1-x}(TiFe_2Sn)_x$ series.

x		0.05	0.1	0.2
		HH (F -4 3 m)		
a (Å)		5.8821(1)	5.8825(1)	5.8849(1)
wt (%)		97.0(5)	97.0(1)	96.2(1)
4b	U_{iso} (Å^2)	0.0040(1)	0.0039(1)	0.0041(1)
	Occ	Ti	Ti	$Ti_{0.97(1)}Fe_{0.03(1)}$
4c	U_{iso} (Å^2)	0.0039(1)	0.0039(1)	0.0041(1)
	Occ	$Co_{0.96(1)}Fe_{0.04(1)}$	$Co_{0.99(1)}Fe_{0.01(1)}$	Co
4a	U_{iso} (Å^2)	0.0040(1)	0.0039(1)	0.0041(1)
	Occ	$Sb_{0.95}Sn_{0.05}$	$Sb_{0.9}Sn_{0.1}$	$Sb_{0.8}Sn_{0.2}$
4d	U_{iso} (Å^2)	0.0040(1)	0.0039(1)	-
	Occ	$Fe_{0.04(1)}$	$Fe_{0.01(1)}$	-
		Ti(P63/mmc)		
a (Å)		2.975(1)	2.973(1)	2.960(1)
c (Å)		4.536(1)	4.537(1)	4.572(3)
wt (%)		3.0(5)	3.0(1)	3.8(1)
	U_{iso} (Å^2)	0.010(1)	0.007(1)	0.008(1)
χ^2		1.15	2.11	6.13
wRp (%)	Bank 3	2.75	2.17	2.56
	Bank 4	2.48	2.46	2.70
	Bank 5	2.42	2.17	3.29
R_p (%)	Bank 3	4.37	2.79	3.60
	Bank 4	6.01	5.37	3.99
	Bank 5	8.73	5.49	5.97

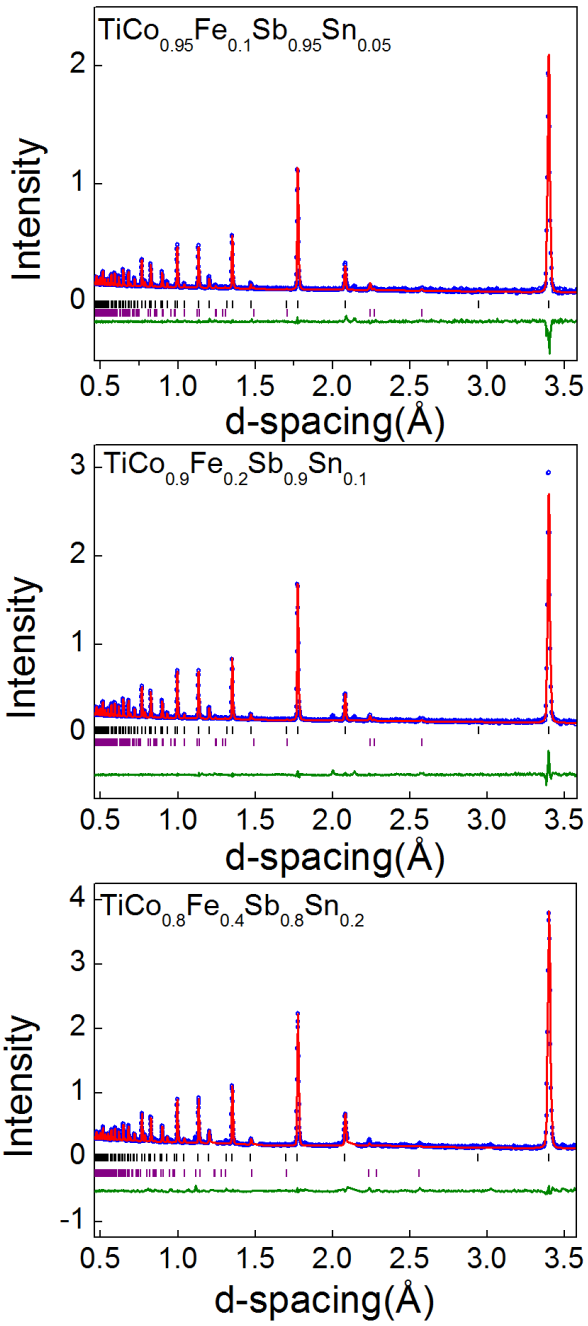

Figure 2. Rietveld refinement to neutron powder diffraction data collected for the $(TiCoSb)_{1-x}(TiFe_2Sn)_x$ (x= 0.1, 0.15, 0.2) series. Blue circles represent the collected data, red line is the calculated data and the green line is the difference. Black tickmarks are for the half Heusler phase and purple tickmarks are for Ti. Data shown are from detector bank 4.

Table 2. Lattice parameters (a), weight percentages, thermal displacement parameters (U_{iso}/Å^2), fractional occupancies and fit statistics for Rietveld refinement of neutron powder diffraction data collected for the $(TiCoSb)_{1-x}(TiCoFeSn)_x$ series. The x = 0.2 sample contained 10.9 wt% of Co_3Sn_2 impurity phase.

x		0.1	0.2
HH (F -4 3 m)			
a (Å)		5.8842(1)	5.8829(1)
wt (%)		95.6(1)	87.0(1)
4b	U_{iso} (Å^2)	0.0040(1)	0.0040(1)
	Occ	Ti	Ti
4c	U_{iso} (Å^2)	0.0040(1)	0.0040(1)
	Occ	$Co_{0.97(1)}Fe_{0.03(1)}$	$Co_{0.95(1)}Fe_{0.05(1)}$
4a	U_{iso} (Å^2)	0.0040(1)	0.0040(1)
	Occ	$Sb_{0.9}Sn_{0.1}$	$Sb_{0.8}Sn_{0.2}$
4d	U_{iso} (Å^2)	-	0.0040(1)
	Occ	-	$Co_{0.03(2)}$
Ti(P63/mmc)			
a (Å)		2.973(1)	2.967(1)
c (Å)		4.542(1)	4.547(1)
wt (%)		4.4(1)	2.1(1)
	U_{iso} (Å^2)	0.008(1)	0.007(1)
χ^2		1.91	4.482
wRp (%)	Bank 3	1.50	3.31
	Bank 4	2.24	3.22
	Bank 5	1.82	4.21
R_p (%)	Bank 3	2.24	5.46
	Bank 4	4.96	4.49
	Bank 5	4.93	5.26

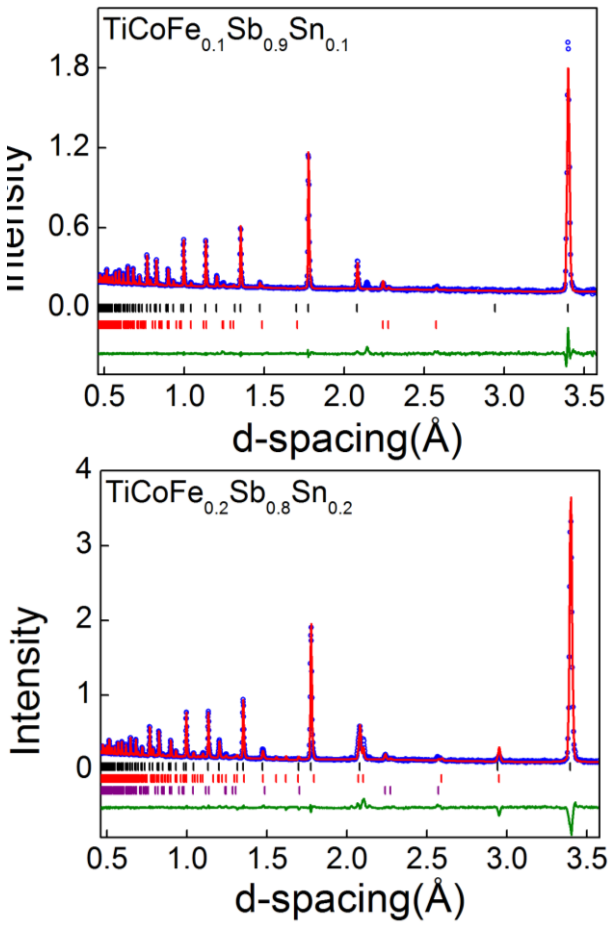

Figure 3. Rietveld refinement to neutron powder diffraction data collected for the $((TiCoSb)_{1-x}(Ti(FeCo)Sn)_x$ (x= 0.1, 0.2) series. Blue circles represent the collected data, red line is the calculated data and the green line is the difference. Black tickmarks are for the half Heusler phase, red marks are for Co_3Sn_2 and purple tickmarks are for Ti. Data shown are from detector bank 4.

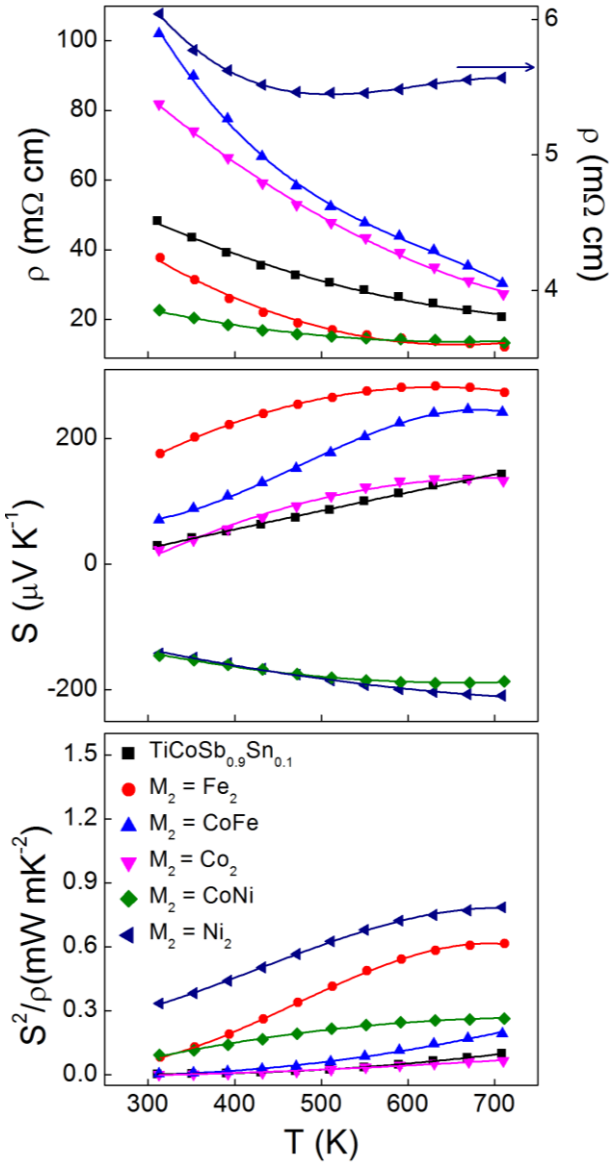

Figure 4. Temperature dependence of the electrical resistivity (ρ), Seebeck coefficient (S) and power factor S^2/ρ for the $(TiCoSb)_{0.9}(TiM_2Sn)_{0.1}$ (M= Fe, FeCo, Co, CoNi, Ni) series. Solid lies are polynomial fits.

Appendix 3

Rietveld fits to neutron powder diffraction data collected for $TiCoSb_{0.9}Sn_{0.1}$, $(TiCoSb)_{1-x}(TiFe_2Sn)_x$ (x= 0.1, 0.15, 0.2) and $(TiCoSb)_{1-x}(Ti(FeCo)Sn)_x$ (x= 0.1, 0.2), referred to in Chapter 5 are provided in this appendix. In addition to this, temperature dependence of the electrical resistivity (ρ), Seebeck coefficient (S) and power factor (S^2/ρ) for the preliminary series $(TiCoSb)_{0.9}(TiM_2Sn)_{0.1}$ is also provided here.

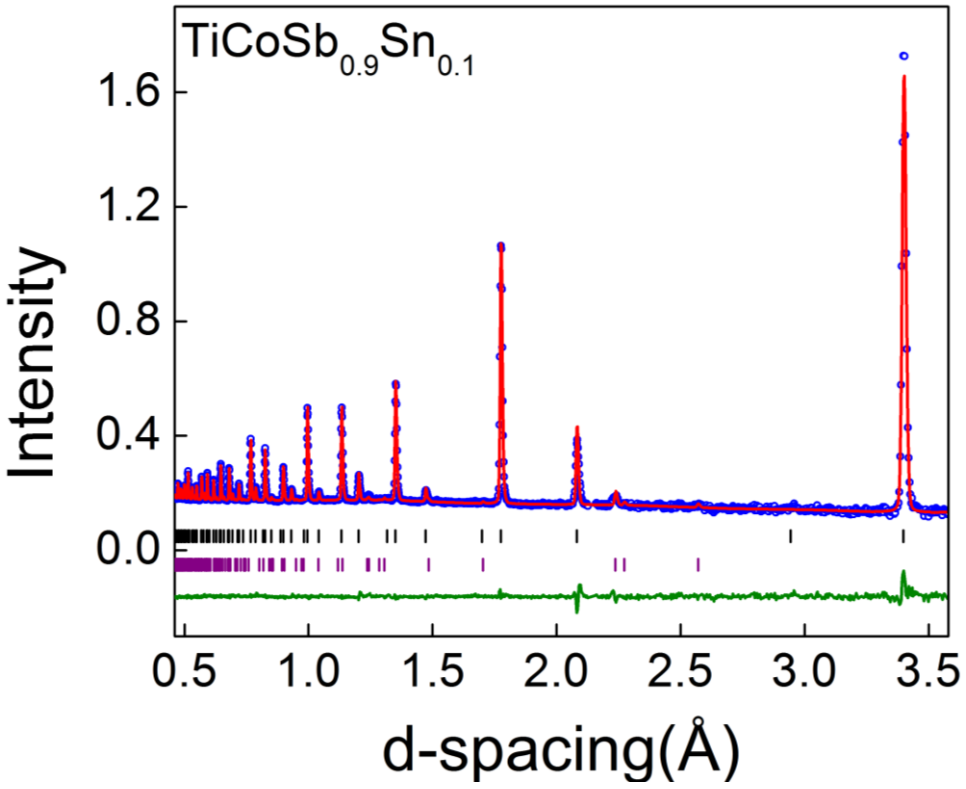

Figure 1. Rietveld refinement to neutron powder diffraction data collected for $TiCoSb_{0.9}Sn_{0.1}$. Blue circles represent the collected data, red line is the calculated data and the green line is the difference. Black tickmarks are for the half Heusler phase and purple tickmarks are for Ti. Data shown are from detector bank 4.

Table 1. Lattice parameters (a), weight percentages, thermal displacement parameters (U_{iso}/Å^2), fractional occupancies and fit statistics for Rietveld refinement of neutron powder diffraction data collected for the $(TiCoSb)_{1-x}(TiFe_2Sn)_x$ series.

x		0.05	0.1	0.2
		HH (F -4 3 m)		
a (Å)		5.8821(1)	5.8825(1)	5.8849(1)
wt (%)		97.0(5)	97.0(1)	96.2(1)
4b	U_{iso} (Å^2)	0.0040(1)	0.0039(1)	0.0041(1)
	Occ	Ti	Ti	$Ti_{0.97(1)}Fe_{0.03(1)}$
4c	U_{iso} (Å^2)	0.0039(1)	0.0039(1)	0.0041(1)
	Occ	$Co_{0.96(1)}Fe_{0.04(1)}$	$Co_{0.99(1)}Fe_{0.01(1)}$	Co
4a	U_{iso} (Å^2)	0.0040(1)	0.0039(1)	0.0041(1)
	Occ	$Sb_{0.95}Sn_{0.05}$	$Sb_{0.9}Sn_{0.1}$	$Sb_{0.8}Sn_{0.2}$
4d	U_{iso} (Å^2)	0.0040(1)	0.0039(1)	-
	Occ	$Fe_{0.04(1)}$	$Fe_{0.01(1)}$	-
		Ti(P63/mmc)		
a (Å)		2.975(1)	2.973(1)	2.960(1)
c (Å)		4.536(1)	4.537(1)	4.572(3)
wt (%)		3.0(5)	3.0(1)	3.8(1)
	U_{iso} (Å^2)	0.010(1)	0.007(1)	0.008(1)
χ^2		1.15	2.11	6.13
wRp (%)	Bank 3	2.75	2.17	2.56
	Bank 4	2.48	2.46	2.70
	Bank 5	2.42	2.17	3.29
R_p (%)	Bank 3	4.37	2.79	3.60
	Bank 4	6.01	5.37	3.99
	Bank 5	8.73	5.49	5.97

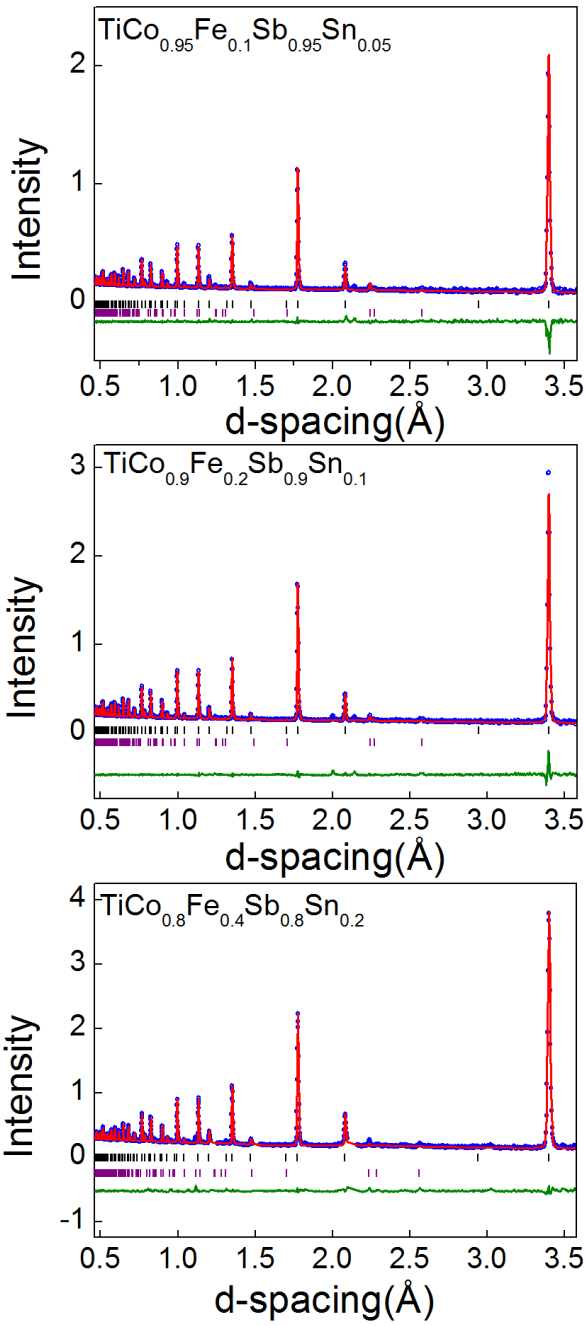

Figure 2. Rietveld refinement to neutron powder diffraction data collected for the $(TiCoSb)_{1-x}(TiFe_2Sn)_x$ (x= 0.1, 0.15, 0.2) series. Blue circles represent the collected data, red line is the calculated data and the green line is the difference. Black tickmarks are for the half Heusler phase and purple tickmarks are for Ti. Data shown are from detector bank 4.

Table 2. Lattice parameters (a), weight percentages, thermal displacement parameters (U_{iso}/Å^2), fractional occupancies and fit statistics for Rietveld refinement of neutron powder diffraction data collected for the $(TiCoSb)_{1-x}(TiCoFeSn)_x$ series. The x = 0.2 sample contained 10.9 wt% of Co_3Sn_2 impurity phase.

x		0.1	0.2
HH (F -4 3 m)			
a (Å)		5.8842(1)	5.8829(1)
wt (%)		95.6(1)	87.0(1)
4b	U_{iso} (Å^2)	0.0040(1)	0.0040(1)
	Occ	Ti	Ti
4c	U_{iso} (Å^2)	0.0040(1)	0.0040(1)
	Occ	$Co_{0.97(1)}Fe_{0.03(1)}$	$Co_{0.95(1)}Fe_{0.05(1)}$
4a	U_{iso} (Å^2)	0.0040(1)	0.0040(1)
	Occ	$Sb_{0.9}Sn_{0.1}$	$Sb_{0.8}Sn_{0.2}$
4d	U_{iso} (Å^2)	-	0.0040(1)
	Occ	-	$Co_{0.03(2)}$
Ti(P63/mmc)			
a (Å)		2.973(1)	2.967(1)
c (Å)		4.542(1)	4.547(1)
wt (%)		4.4(1)	2.1(1)
	U_{iso} (Å^2)	0.008(1)	0.007(1)
χ^2		1.91	4.482
wRp (%)	Bank 3	1.50	3.31
	Bank 4	2.24	3.22
	Bank 5	1.82	4.21
R_p (%)	Bank 3	2.24	5.46
	Bank 4	4.96	4.49
	Bank 5	4.93	5.26

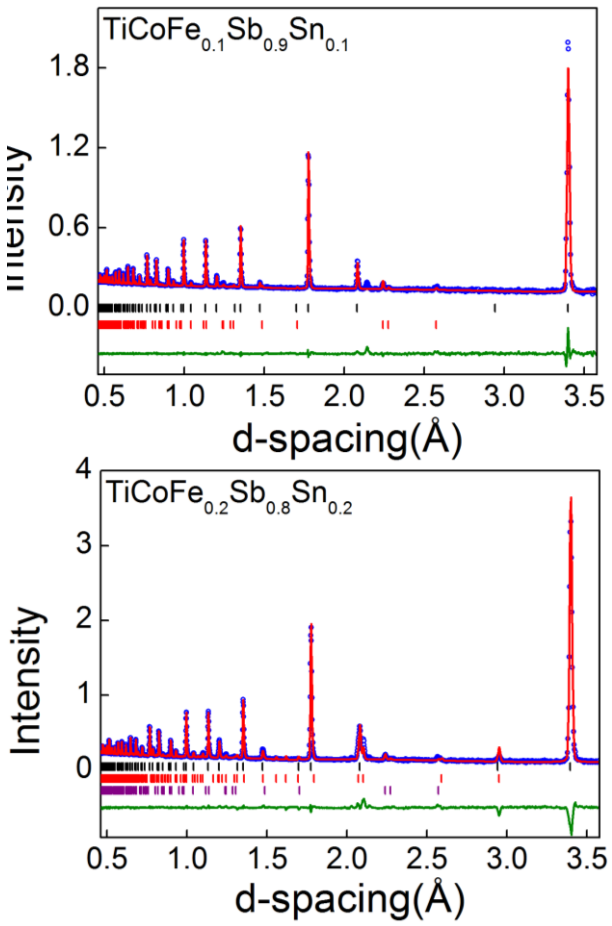

Figure 3. Rietveld refinement to neutron powder diffraction data collected for the $((TiCoSb)_{1-x}(Ti(FeCo)Sn)_x$ (x= 0.1, 0.2) series. Blue circles represent the collected data, red line is the calculated data and the green line is the difference. Black tickmarks are for the half Heusler phase, red marks are for Co_3Sn_2 and purple tickmarks are for Ti. Data shown are from detector bank 4.

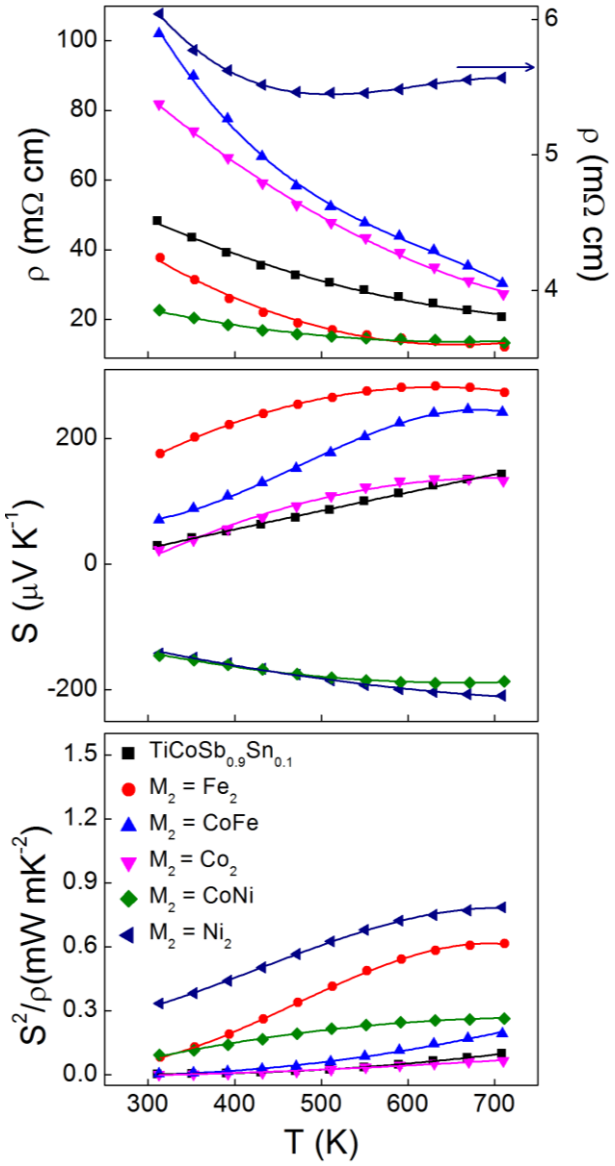

Figure 4. Temperature dependence of the electrical resistivity (ρ), Seebeck coefficient (S) and power factor S^2/ρ for the $(TiCoSb)_{0.9}(TiM_2Sn)_{0.1}$ (M= Fe, FeCo, Co, CoNi, Ni) series. Solid lies are polynomial fits.